7-31-2021

Predicting Flow Through the Causeway of the Great Salt Lake Using Hydrodynamic Simulations and Artificial Neural Networks

Som Dutta
Utah State University

Brian Mark Crookston
Utah State University

Michael Rasmussen
Utah State University

Eric Larsen
Utah State University

Recommended Citation

Dutta, Som; Crookston, Brian Mark; Rasmussen, Michael; and Larsen, Eric, "Predicting Flow Through the Causeway of the Great Salt Lake Using Hydrodynamic Simulations and Artificial Neural Networks" (2021). *Reports.* Paper 679.
https://digitalcommons.usu.edu/water_rep/679

Final Report

Predicting Flow through the Causeway of the Great Salt Lake using Hydrodynamic Simulations and Artificial Neural Networks

---

July 31, 2021

Prepared for

Utah Department of Natural Resources

Prepared by

UtahStateUniversity
UTAH WATER RESEARCH LABORATORY

Hydraulics Report No. 4450

Final Report

Predicting Flow through the Causeway of the Great Salt Lake using Hydrodynamic Simulations and Artificial Neural Networks

Institutional Proposal NUMBER: 00204715
Award ID: 203145-00001

Prepared for
Utah Department of Natural Resources

By
Utah State University, Utah Water Research Laboratory
Som Dutta, PhD
Brian Mark Crookston, PhD, PE
Michael Rasmussen, EIT
Eric Larsen, EIT

July 31, 2021

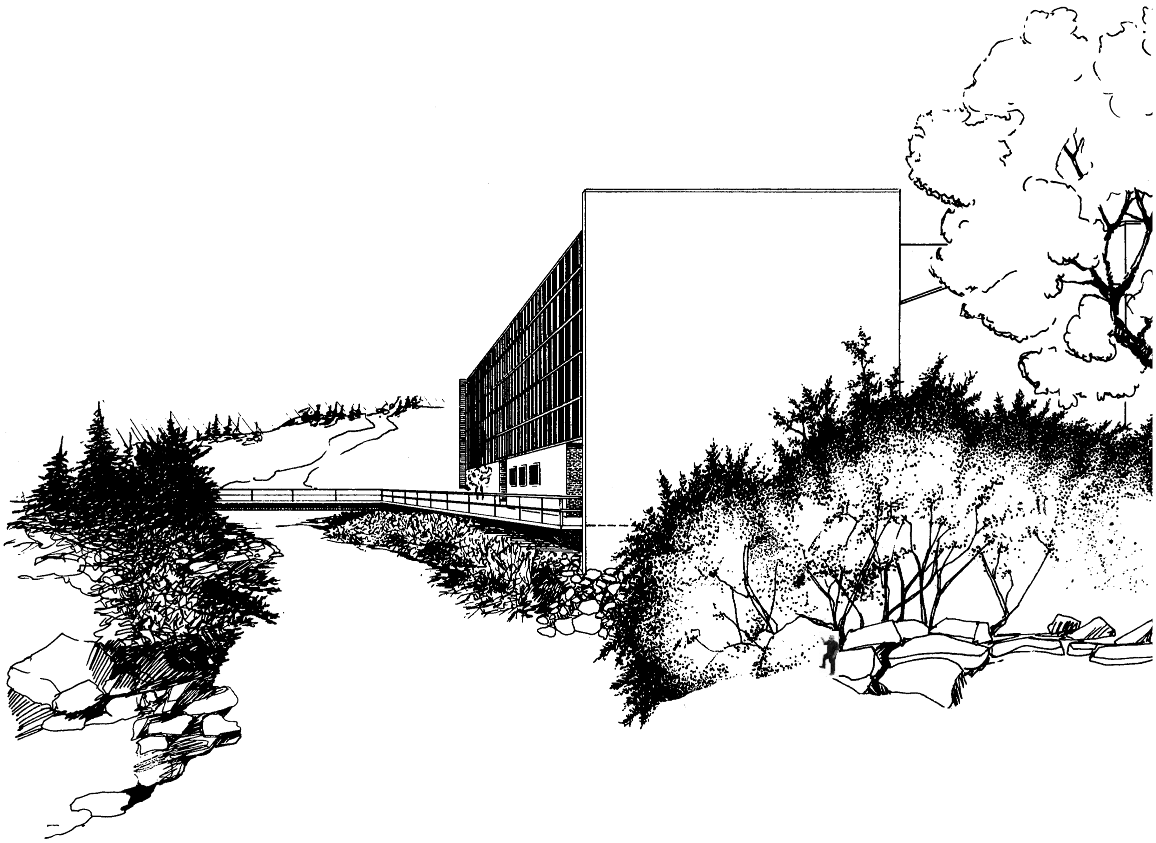

UTAH WATER RESEARCH LABORATORY

Hydraulics Report No. 4450

UtahState University
UTAH WATER RESEARCH LABORATORY

Any Unpublished USGS Data Included Herein is

Provisional and Subject to Revision

Table of Contents

List of Tables

List of Figures

The N-S flow usually occurs during sustained north to south wind events. below the south arm water and form a sustained bottom current that continues to move southward, eventually forming the deep brine layer (DBL). N-S winds lead to reduction in WSE difference between the South and North arms of the lake at the breach, allowing the higher density North arm water to push back the S-N flow through the breach. This leads to the flow registered by the USGS ADVM uplooker to show sustained N-S flow through the breach. We used the CFD model developed for the bidirectional case, and changed the WSE at the boundaries to the values observed during the wind-event. We did not explicitly add the wind-induced shear at the water-surface in the CFD model, to test the hypothesis that the local effects of the wind are not necessary to capture the general

Acronyms and Abbreviations

ADVM	Acoustic Doppler Velocimeter Meter
ANN	Artificial Neural Network
CFD	Computational Fluid Dynamics
DBL	Deep Brine Layer
GSL	Great Salt Lake
CAD	Computer-Aided Design
DO	Dissolved Oxygen
SoW	Scope of Work
TDS	Total Dissolved Solids
UDNR	Utah Department of Natural Resources
USGS	U.S. Geologic Survey
USU	Utah State University
UWRL	Utah Water Research Laboratory
WSE	Water Surface Elevation
N-S	North to South
S-N	South to North
DNN	Deep Neural Network

1.0 Executive Summary

At the Great Salt Lake, the northern and southern portions of the lake are divided by an east-to-west causeway that disrupts natural lake currents and significantly increases salt concentrations in the norther portion. To support management efforts to address rising environmental and economic concerns, the causeway was recently modified to include a new breach that typically exhibits a strong density-driven bidirectional flow pattern. To obtain much needed insights into the hydraulic performance of this hydraulic structure and the exchange between the two sections of the lake, a field campaign coupled with computational fluid dynamics (CFD) modeling and an artificial neural network (ANN) model were undertaken.

Utah State University (USU) and the Utah Water Research Laboratory (UWRL) conducted monthly field measurements at the West Crack Breach of the Great Salt Lake (GSL) causeway, supported by the U.S. Geologic Survey (USGS). Data collected by USU/UWRL Team, publicly available data from USGS, and preliminary data from USGS shared with USU/UWRL were used in CFD and ANN modeling including formulation, calibration, and verification.

The following observations and conclusions are based upon the field campaign and results of these two modeling efforts:

- The CFD model is able to accurately simulate and predict flows through the West Crack Breach at the Great Salt Lake Causeway, including north-to-south flow patterns, bidirectional flow patterns (most common), and south-to-north flow patterns.
- The CFD model provides new insights into the flow field through the breach for the simulated cases. The model is sensitive to the following parameters, which are confirmed to be actual sensitivities of the Lake: water densities, water surface elevations, differences in density and water surface elevation, strong winds, and the breach geometry including the submerged berm.
- Through this study it was shown that the ANN was able to adequately predict the total discharge from one arm to the other at the west crack breach. It was shown

that for general cases of bi-directional flow the ANN was able to predict the discharge with high fidelity.

- This study also shows that the ANN model approximation deteriorates as the model approaches extreme flow events, both in high and low discharge measurement. It was also shown that with the limitations of the ANN, the model was still able to perform better than a standard regression model. During development of the ANN the limitation in the amount of single flow event information led to the limitation of the model. If there was a larger data pool available for extreme flow event cases it is anticipated that the ANN would be able to have higher R2 values for all flow cases.
- This study included a breach rating curve that can be used for hydrologic modeling.

However, additional field data, CFD simulations, and supporting research is needed to:

- Investigate flows through the breach at lower lake levels to estimate if critical conditions exist where unsatisfactory flow exchange occurs,
- Increase the robustness of the rating curve to consider climate change and extreme events,
- And to study different submerged berm geometries to support management efforts.

Finally, the continuous measurements by USU/UWRL were critical for model development, simulations, and flow predictions. We recommend that continuous density and temperature measurements continued at the breach at they are necessary input for the flow rating curve at the breach as part hydrologic modeling of the lake. This data is also necessary for additional modeling efforts as noted above.

2.0 Introduction

2.1 Lake Overview

The Great Salt Lake (GSL) is a significant body of water that is unique in composition, size, and ecology. As an economic resource it contributes more than $1.3 billion annually to Utah’s economy through mineral extraction and its world-leading brine shrimp production (Bioeconomics, 2012; Wurtsbaugh et al., 2016). Recreational attractions connected to the GSL also play a significant part in the local economy, including motorsport activities at the salt flats and primarily due to GSL’s unique ecosystem that provides habitat for almost 5 million migratory birds every year (WHSRN, 2016). The importance of the GSL has attracted both domestic and international interest, resulted in significant research and monitoring efforts (Loving et al., 2000).

The GSL includes a causeway that was constructed in 1959 by the Union Pacific Railroad Company (UPRR). The causeway divides approximately 1/3 of the lake from the southern portion, which has altered its characteristics including natural circulation, water and salt balances, etc. (Waddell and Bolke, 1973). For example, since 1959 the northern part of GSL has become more saline while salt content in the southern portion has become lower (Stephens, 1990; Loving et al., 2000). These changes in observed salinity have occurred despite the inclusion of two culverts. These culverts were recently abandoned and the new West Crack Breach was constructed in 2016-2017 (see Fig. 2.1).

Figure 2.1. The original 15 ft wide culverts of the causeway that have been closed in December 2013 (top left and right). The breach built in 1984 (bottom left), and the breach created in 2016 (bottom right) are currently the connections between the northern and southern parts of GSL. The flow through the breaches will depend on the difference in densities and water surface elevations (WSE) between the two sides, and on the structure of the bridge. [pictures reproduced from https://usgs.gov/news and https://www.up.com/aboutup/community/inside_track/causeway-6-14-2016]

The differences in salt concentrations have caused complex hydraulic conditions at the West Crack Breach that are influenced by weather patterns. Three general flow patterns have been observed: 1) flows passing from the north to the south, 2) flows passing south to north, and most commonly 3) a stable, stratified bidirectional flow with the upper layer flowing north with the lower density current flowing south.

2.2 Project Scope of Work

Utah State University (USU) was awarded $75,000 by Utah Dept. of Natural Resources (Utah DNR), which was enhanced by USU with a funding match of $20,900 to perform the scope of work (SoW) from Aug. 1 2020 to July 31, 2021. This SoW from the selected grant proposal is included herein for USU/UWRL research efforts at the West Crack Breach of the Great Salt Lake Causeway (see Fig. 2.2). Please note that the USU/UWRL team adapted this SoW to local conditions at the breach, especially the frequency of the field visits.

The primary purpose of this research was to gain new insights into the hydraulics at the breach to support water management efforts for the lake, including the exchange of flows between the north and south portions of the GSL. Although the SoW was completed, additional research is needed to expand the west crack breach rating curve, consider the effects of alternative submerged berm geometries at the north entrance to the breach, and consider future likely scenarios of the lake as a consequence of climate change, economic activities, etc.

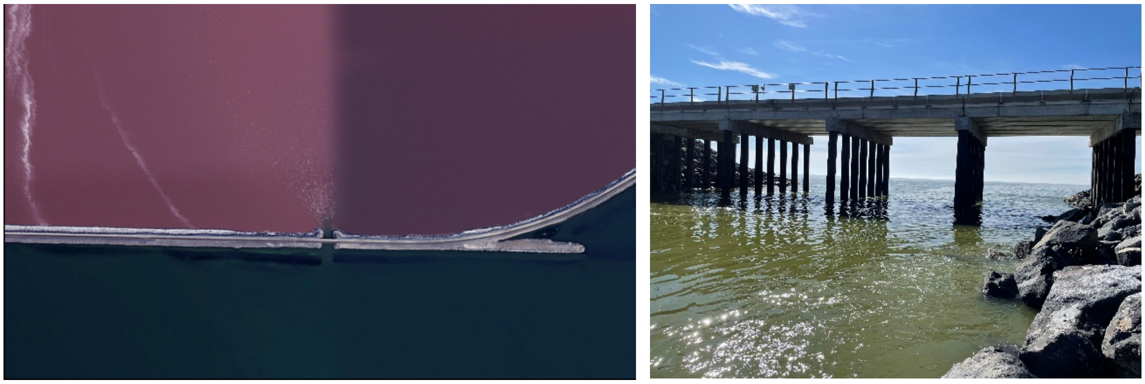
(a) (b)

Figure. 2.2. (a) Satellite image of the causeway and the West Crack (WC) Breach. The hyper-saline northern arm of the lake has a pink color due to presence of microbes that thrive in the hyper-saline environment (b) Picture of the WC Breach taken from the northern side of the causeway.

2.2.1 Objective 1: Historical Understanding of the flow through different breaches in the GSL causeway and Aggregation of Existing Data (Completed)

Various federal and state agencies have been collecting data within the GSL since 1966. Over the years, the USGS has maintained a series measurement gages, buoys, and stations to monitor the flow and salinity in various parts of GSL. Two of the most important gages were the ones at the Eastern and Western culverts in the causeway (see fig. 2.1), which monitored the flow through the culverts until their closure in December 2013. For the existing breaches, the USGS 10010020 GSL station has daily and monthly discharge data since 2008 for the 290 ft. breach opened in 1984. Analysis of the discharge data from the USGS gage for a 5-year period (2009-2013) showed the dynamic nature of the flow, as net discharge ranged between 12000 ft3s-1 south to north and 5862 ft3s-1 north to south. During this period about 1510 north to south flow events were observed, with some of them lasting up to 32 hours (Freeman, 2014). Flow reversal events primarily occurred during the months of September to May, when either the WSE difference between the northern and the southern arm is at a minimum, or the temperature of water is relatively low. The strong sensitivity of GSL water density to temperature agrees with the equation of state developed by Naftz et al. (2011b).

The USGS 10010026 GSL station has daily discharge data for the breach opened in December 2016, along with water quality and salinity data measured sporadically. Additionally, there is daily water surface elevation (WSE) data from the north (USGS 10010027) and south (USGS 10010024 GSL) of the new breach. There are multiple USGS gages, especially in the southern arm of the GSL, that monitor salinity and WSE. Most of the data we have discussed are available publicly through waterdata.usgs.gov/nwis. There are also other sources of historical data about flow through the causeway and spatial variation of salinity (e.g. from HDR), which has been used for development and validation of the models. Under the aegis of the current project we have brought together data from disparate sources, about the flow through the breach and the GSL under one repository. In the future, we plan to make the data available through a platform like HydroShare.

We have coordinated with ongoing data collection efforts by USGS (Rowland, 2016) in order to understand how we can fill that gap in the data. More details about our data collection efforts have been illustrated in later sections. One of the main data we collected is water temperature and specific conductance (σ), north and south of the breach. These data has been invaluable in setting up the boundary conditions for the CFD model, and training the ANN models.

2.2.2. Objective 2: Field Study **(Completed, additional monitoring needed)**

Accurate and reliable field data serves as the primary input and help test the accuracy of numerical models. The multiple historic data sets (UGS, USGS, Rowland 2016, etc.), digital elevation models, and hydrologic data sets are of great value for Objective 3. However, this effort requires detailed hydraulic measurements at and around the openings in the causeway, consisting of velocity, temperature and σ profiles at strategic locations. We conducted field study in collaboration with USGS, and also installed instrumentation for high-frequency measurement of σ and temperature. During the visits, digital imagery and videos of flow condition has also been collected. The new data collected by USU will made available through a repository. High-frequency measurements at the breach will continue in the future, augmented by ADCP based velocity measurements in collaboration with USGS.

2.2.3. Objective 3: Developing and Validating the 3D Computational Fluid Dynamic Models **(Completed)**

Despite being a complex flow problem, there has only been two recent studies that have used hydrodynamics modeling to study different aspects of the GSL. Spall (2009) and Naftz et al. (2011) used 3D hydrodynamic models that incorporated baroclinic and barotropic responses, tidal forcing, wind stresses, Coriolis effects, surface thermal forcing, inflows, outflows, and transport of salt, heat and passive scalars. Spall (2009) investigated the effects of surface heat flux and wind forcing on the spatio-temproal variations in the flow patterns within the southern arm of GSL. Naftz et al. (2011) studied the transport of methylmercury through modeling temperature of the water-column and the process of diurnal overturning in the southern wetlands of GSL. Neither of the studies modeled the spatio-temporal dynamics of the deep brine layer (DBL) in GSL, or the bidirectional flow passing through the causeway openings.

We developed the first 3D CFD model of flow through the West Crack breach. Our goal was to develop a model that captures the complex interaction between the bidirectional flow and the hydraulics structure of the breach. The model was developed using the multiphase CFD solver FLOW-3D© (Flow-3D) that is a non-hydrostatic finite-volume–finite- difference solver employing a fractional volume of fluid method (Hirt and Nichols,

1981) to track the interface (fluid-fluid or fluid-air) between different phases. We have used the one-fluid multiphase model based on the Boussinesq approximation. Turbulence in the flow will be modeled using the Smagroinsky large eddy simulation (LES), and was chosen after comparison against different Reynolds averaged Naveir-Stokes (RANS) closures (Rodi, 1993). FLOW-3D has been used successfully to study variable density flows and various complex multiphase flow problems, e.g. multiphase sewage flows in water reclamation plants (Dutta et al., 2014), estimation of flow discharge through hydraulic structures (Crookston et al., 2018), aeration modeling (Aydin et al, 2019), etc. The initial CFD model development had focused on the cases that have detailed field observations, as this will be help minimize uncertainty in model validation.

2.2.4. Objective 4: Predicting Different Scenarios using the 3D Models **(Completed, more work needed)**

Once the CFD model has been developed and validated, it has been used to simulate a range of hypothetical conditions that will fill up the gap in and go beyond the parameter range observed in the field. This process will generate more data, that will then be used to develop a rating formula. This exercise will also help us understand and predict the flow dynamics at the breach for different hypothetical situations that may arise in the future due to man-made or natural changes to the GSL.

2.2.5. Objective 5: ANN Model Development using Measured and Model Generated Data **(Model Completed, needs to be integrated with GSLIM model)**

With the advent of large amounts of data, data-driven and machine-learning based models have become an important tool for accurately predicting complex phenomena. The best thing about these models are that once they have been developed and trained using reliable data about the phenomena, they can predict different aspects of the phenomena fairly quickly. For the current project we have used publicly available data from GSL and data collected by the USU team during field visits. We have used the data to develop an Artificial Neural Network (ANN) based model for predicting the flow through the causeway. Historically, for a host of problems in hydraulics, ANN based models have been found to perform substantially better than most correlation/statistics-based models (Ghosh et al., 2014). The trained and tested ANN model can then be coupled with the new GSLIM model that has been developed on the GoldSim platform. For the ANN model, we will use Backpropagation as the training algorithm, along with a conjugate-gradient based algorithm (e.g., Levenberg-Marquardt) for minimizing the error (Rojas, 1996). The proposed ANN model will not be the first ML based model trained to predict some aspect of GSL. Abdel-Hafez (2007) developed self-learning machines (ANNs, SVMs, and RVMs) to predict water-level in GSL.

3.0 Field Campaign

3.1 Historical Data

Prior to performing the field campaign, existing data was compiled and evaluated in order to prioritize missing data required for the CFD and ANN modeling efforts. A summary of the monitoring locations is provided in Fig. 3.1 with corresponding records shown in Table 3.1.

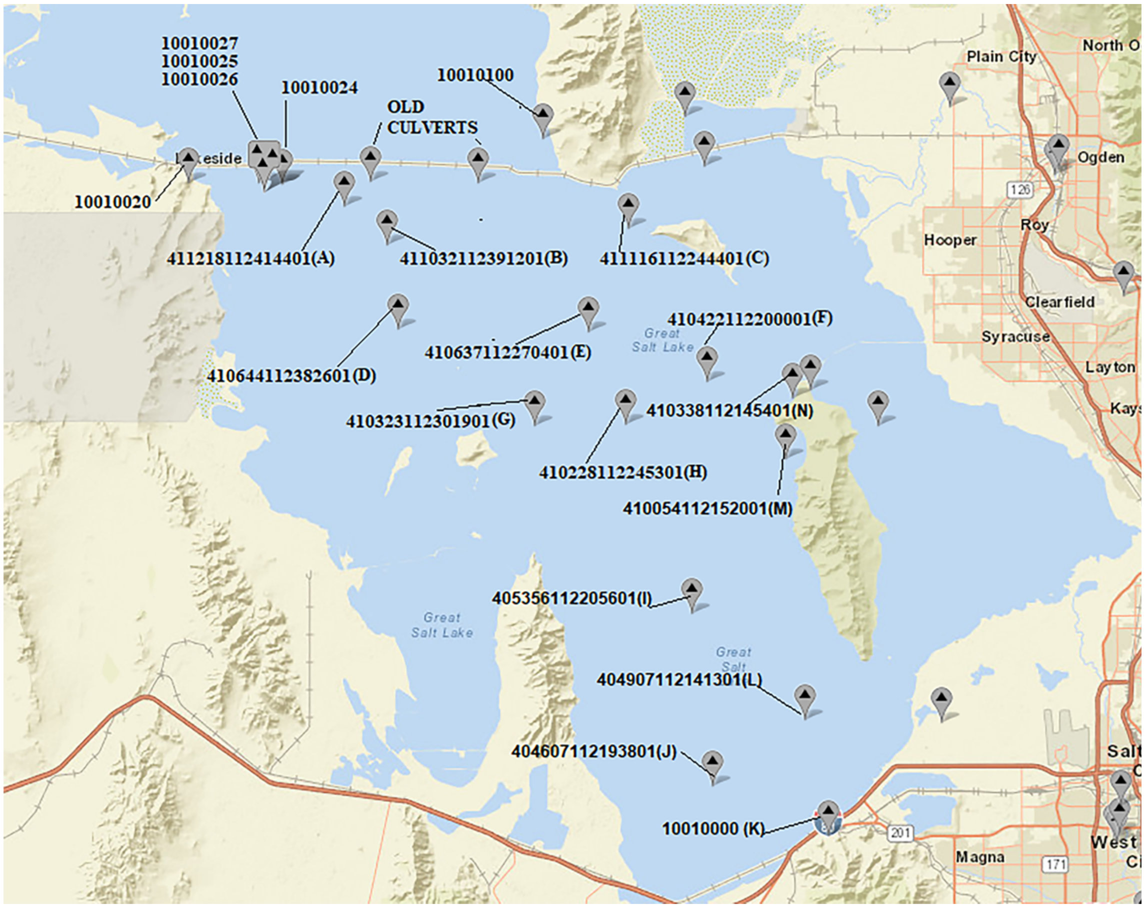

(a)

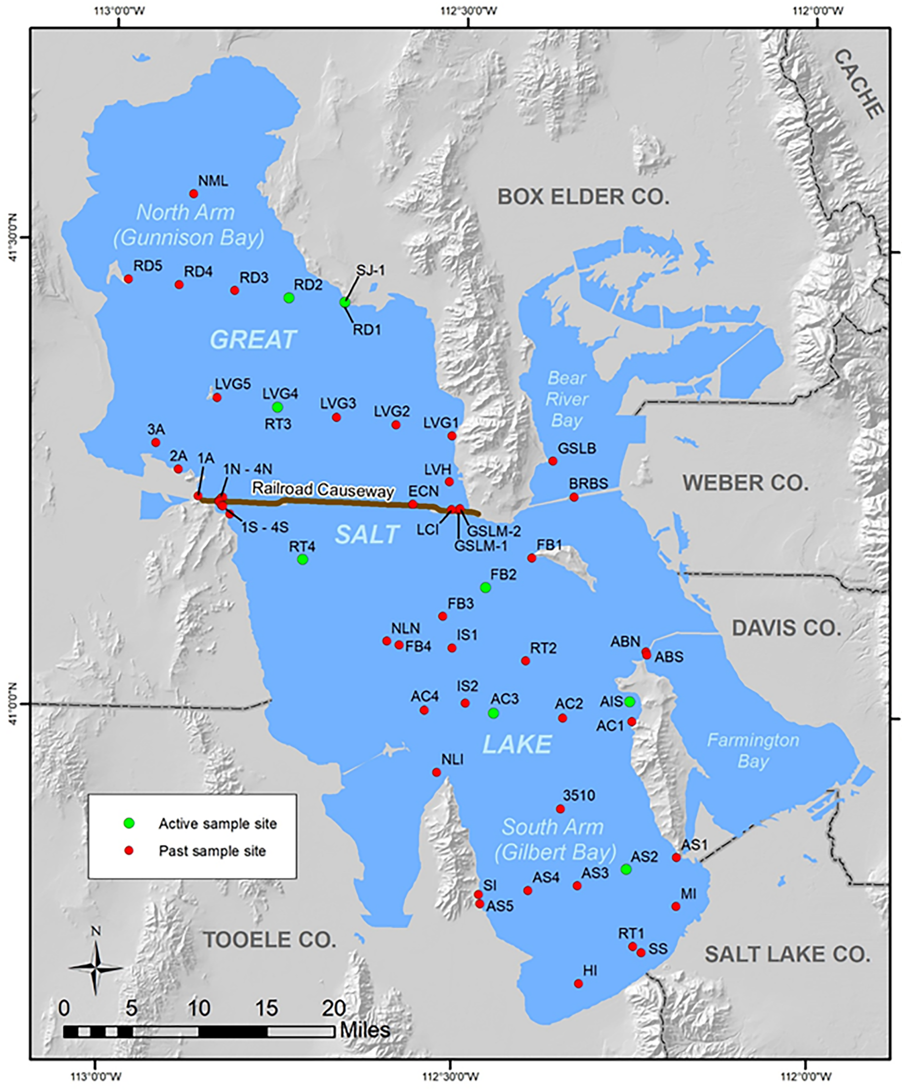

Great Salt Lake brine sample locations. Great Salt Lake is represented at its extent when the water level is at 4200 feet elevation.

(b)

Figure 3.1. Overview of historical USGS monitoring locations at the Great Salt Lake (a), and (b) Utah Department of Natural Resources monitoring locations.

Table 3.1. Summary of historical data at the Great Salt Lake

Site	Discharge	WSE	Air temp	Point velocity	Velocity Profile	Wind Speed	Bar. Pressure	Water temp.	Water temp. profile	Sp. Cond.	Salinity	Density	Dis. Solids	σ	Time
10010020	x	x		x		x	x	x		x	x	x	x	x	12/96-Present
10010024		x													12/18-Present
10010025	x	x		x	x	x	x	x		x	x	x	x	x	12/16-Present
10010026	x			x		x	x	x		x	x	x	x	x	12/16-Present
10010027		x													11/18-Present
10010100		x													4/16-Present
A							x	x		x	x	x			11/16 - 8/20
B							x	x	x	x					7/16 - 7/18
C							x	x		x	x	x	x		9/95 - 11/20
D			x				x	x		x	x	x	x	x	8/95 - 11/20
E			x				x	x		x	x	x			12/02 - 10/20
F			x				x	x		x	x	x	x		8/95 - 11/20
G							x	x		x	x	x			8/95 - 10/20
H								x	x	x					11/16 - 7/18
I			x			x	x	x	x	x	x	x	x		8/95 - 11/20
J			x				x	x		x	x	x			8/95 - 11/20
K		x	x			x		x		x	x	x	x	x	10/18 - Present
L								x	x	x	x	x			7/16 - 9/20
M										x					7/20 - 10/20
N										x					7/20 - 10-20

*yellow highlights = data sampled at monthly intervals

As illustrated, a significant amount of data has been collected in the lake. After construction of the breach was finished, USGS and the engineering firm HDR, Inc. (the consultants tasked with design and construction of the breach) had collected at the breach σ, TDS, temperature, and estimating density and salinity. This data from 2017 was provided to USU. For example, data from June 5, 2019 at 12 in increments at the breach is presented in Table 3.2.

Table 3.2. Sample USGS data collected monthly at West Crack Breach.

date	Station	distance_Lbank	Time	Depth_ft	Sample Elevation ft	pH	Temp_degC	σ	DO	USGS Station #
6/5/2019	1	17	10:18	2	4192.8	8.22	20.68	130206	3.99	10010025
6/5/2019	1	17	10:20	6	4188.8	8.18	20.23	138162	4	10010025
6/5/2019	1	17	10:35	8	4186.8	8.21	19.8	143516	4.51	10010025
6/5/2019	1	17	10:32	11	4183.8	7.65	18.87	220834	8.7	10010026
6/5/2019	1	17	10:27	13.5	4181.3	7.62	18.76	221051	8.51	10010026
6/5/2019	2	32	10:43	2	4192.8	8.29	21.4	127317	4.18	10010025
6/5/2019	2	32	10:44	6	4188.8	8.23	20.86	135093	3.82	10010025
6/5/2019	2	32	10:45	8	4186.8	8.21	19.46	140000	4.31	10010025
6/5/2019	2	32	10:53	11	4183.8	7.65	19.11	220886	8.86	10010026
6/5/2019	2	32	10:55	16	4178.8	7.64	19.13	220791	8.9	10010026
6/5/2019	3	49	10:58	2	4192.8	8.28	21.29	126876	4.16	10010025
6/5/2019	3	49	11:00	6	4188.8	8.24	20.82	134024	3.99	10010025
6/5/2019	3	49	11:03	8	4186.8	8.22	19	141075	4.51	10010025
6/5/2019	3	49	11:09	11	4183.8	7.65	19.05	220412	8.82	10010026
6/5/2019	3	49	11:11	16	4178.8	7.64	18.96	220365	8.77	10010026
6/5/2019	4	66	11:16	2	4192.8	8.26	20.92	129175	4.07	10010025
6/5/2019	4	66	11:19	6	4188.8	8.21	20.1	138076	3.93	10010025
6/5/2019	4	66	11:21	8	4186.8	8.21	19.1	145000	4.1	10010025
6/5/2019	4	66	11:26	11	4183.8	7.66	19.01	220461	8.57	10010026

6/5/2019	4	66	11:29	16	4178.8	7.64	18.85	220601	8.61	10010026
6/5/2019	5	81	11:35	2	4192.8	8.29	21.4	126211	4.18	10010025
6/5/2019	5	81	11:40	6	4188.8	8.22	20.38	135993	3.92	10010025
6/5/2019	5	81	11:42	8	4186.8	8.17	19.1	152251	4.08	10010025
6/5/2019	5	81	11:48	11	4183.8	7.65	19.17	220122	8.69	10010026
6/5/2019	5	81	11:49	16	4178.8	7.64	19.16	221383	8.75	10010026

Following the compilation and review of historical data the USU/UWRL team concluded that continuous monitoring of σ in the north and south arms at the breach, along with point velocities, temperature profiles, and additional samples by boat adjacent to the breach were needed for modeling efforts.

3.2 Field Campaign

A field campaign by the USU/UWRL Project Team was conducted at the WC Breach of the Great Salt Lake causeway, located approximately 53 km northwest of Salt Lake City and about 27 km west of Promontory Point. At this location lake depths were on average less than about 6 meters. Field data were collected from October 1, 2020 to June of 2021 (see Table 3.3) with supplemental data obtained from USGS who have been collecting field data from the time the WC Breach was completed. Field observations were made via shore access and by kayak (see Fig. 3.3) and included σ measurements (Aqua Troll 600) and water grab samples (analyzed at the UWRL) at and adjacent to the breach at various depths. Field measurements also included temperature profiling (Hobo temperature sensors at 12-in spacing) at a central pier on the north face of the breach, and video and photo documentation of visual observations.

Additional select photos of the field campaign are included in Appendix C.

Table 3.3. Field Campaign

Date	Summary
7/30/2020	1st site visit.
10/1/2020	SC profiles near the breach
11/5/2020	SC profiles near the breach. Water samples collected for TDS.
11/13/2020	Downloaded data from AquaTroll 600
12/3/2020	Downloaded data from AquaTroll 600

1/6/2021	Downloaded data from AquaTroll 600
2/2/2021	Downloaded data from AquaTroll 600. Water samples collected for TDS.
3/2/2021	Downloaded data from AquaTroll 600. Used velocity probe.
4/29/2021	Temperature array installed. AquaTroll 600 data collected
5/20/2021	Unexpected bad weather. Observed N-S flow case.
7/12/2021	Temperature array downloaded and reinstalled. North sonde casing installed. Data downloaded.

Water samples were collected initially at multiple locations north and south of the causeway breach at specific flow depths (e.g., 0.15 m to 4.6 m at approximately 0.3 m spacing), with samples processed back at the lab for Total Dissolved Solids (TDS) in accordance with standard methods. Locations were GPS located and depths were measured with a field tape accurate to ±30 mm. A simple tubing and syringe system was used to collect samples, with the tubing placed at the prescribed depth and then a volume secured in the large syringe. Flushing was performed between each sample to minimize contamination and ensure accurate sampling. Shoreline samples were also collected and processed in the laboratory. A summary of direct samples is provided in Table 3.4.

Table 3.4. Water samples collected at GSL for analysis at UWRL for TDS

Date	Sample ID	Depth (ft)	Temp (℃)	σ (μS/cm)	TDS (g/L)
11/5/2020	1	12	11.13	186250	189
	2	13	11.26	202983	236
	3	14	11.29	211667	250
	4	15	11.5	216067	293
	5	0.5	12.6	168300	160
	South Shore	0	-	170583	160
	North Shore	0	-	215983	265
5/13/2021	North Shore	0	-	-	294
	South Shore	0	-	-	151
7/20/2021	North Shore	0	-	-	313
	South Shore	0	-	-	169

Direct measurements were then juxtaposed to indirect continuous salinity measurements using an In-Situ AquaTroll 600 multi-parameter water quality sonde, which measured σ and was calibrated to ±5%. Instrumentation location was selected following general measurements via kayak approximately 1 km north and 1 km south of the breach and approximately 2 km east-to-west, which indicated generally uniform σ values adjacent to the density driven currents through the breach. Therefore, it was appropriate to install monitoring locations approximately 400 meters from the breach on the south bank of the causeway for southern water measurements (Fig. 3.3a) and on a pier approximately 10 m from shore and 800-m west of the WC Breach. Instruments were placed within a perforated PVC casing that allowed for any natural water circulation. The southern instrumentation casing extended out into the lake and was approximately 1/3 the flow depth from the lake bottom. Near the conclusion of this study the north measurement location was shifted to the north bank with an instillation similar to the south bank install, as prior storms had removed the instrument and casing from the pier. Field data were collected initially at 30 min interval continuously, but after November 2021 field data was sampled at 10 min intervals continuously; field data was downloaded from the sondes every 1–2-month period with routine calibrations performed before relaunching the sondes.

The USGS and other government agencies have field records of the Great Salt Lake extending more than 50 years. Regarding the 2017 breach, USGS field records include various buoys measuring σ at monthly intervals, located in the vicinity of the causeway (see Figs. 3.4, 3.5 and 2.1) but at a considerable distance from the breach. In addition, samples were collected by USGS at the breach on monthly intervals (locations 10010026 and 10010025) since 2017. At the breach an acoustic doppler velocimeter meter (ADVM) uplooker was placed by USGS in 2017 adjacent to a row of piers and at the bottom of the breach, directly below the north face of the bridge decking (see Fig. 3.6). The ADVM sensor is approximately 0.5 m from the lakebed and begins sampling 1.3 m from the lake bottom. USGS estimates velocity profiles at this location using the Index Velocity Method [25] with corresponding index rating and 9 vertical bins. During this study ADVM data was shared with USU, but the official review and online publication of the data by USGS was underway and had not yet been completed. In addition to salt concentrations and velocity measurements, the USGS monitored WSE at an adjacent pier in the northern section (see Fig. 3.3b), at a pier to the east of the breach in the southern section, and at the breach (see Fig. 2.2b and 3.5).

(**a**) (**b**)

Figure 3.3. Field sampling for σ and TDS from shore in the southern portion (a) and at a pier in the northern portion (b) of the Great Salt Lake.

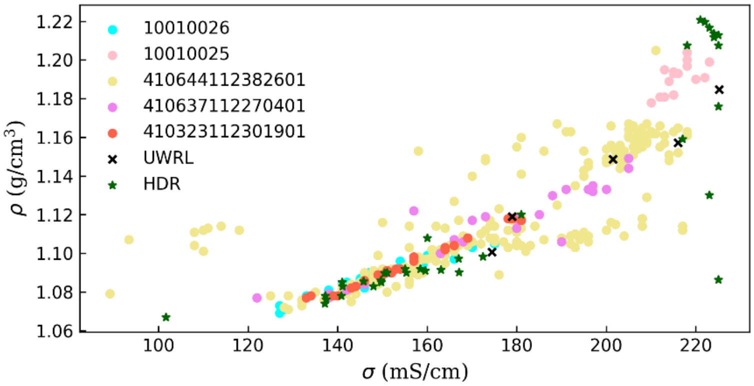

Figure 3.4. Saltwater density ρ as a function of specific conductivity σ for the Great Salt Lake (USGS, 2020). Note the station numbers refer to USGS monitoring stations. Several samples measured by UWRL and HDR (HDR 2019,2020) are also included on the plot for juxtaposition with USGS measurements.

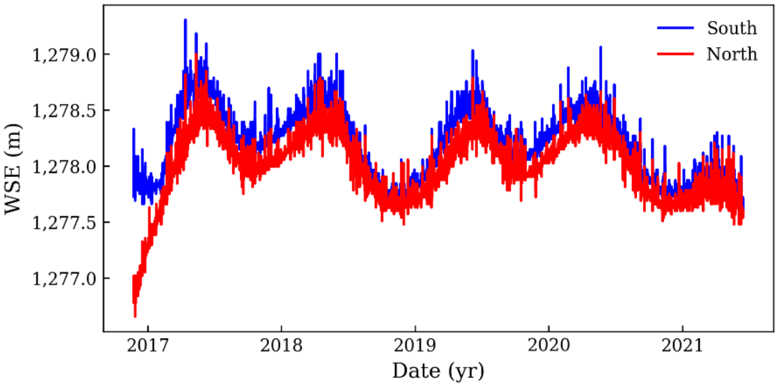

Figure 3.5. Northern and southern WSE for the Great Salt Lake at USGS stations 10010100 (North) and 10010000 (South). The average WSE difference between north and south is around 0.15m (0.5ft) since construction of the West Crack breach finished in late 2016. (USGS, 2020)

As shown in Figs. 3.4 and 3.5, some variability in field measurements were recorded, which are a function of instrument accuracy but more due to lake dynamics and temporal variations in response to climate, weather patterns, etc. These factors were considered when selecting boundary conditions for the computational fluid dynamics (CFD) simulations and a case that is representative of the density driven bidirectional flow patterns and specific velocity data and corresponding WSEs along with a sensitivity analysis of densities and velocity profile location.

A vertical temperature array was installed at the GSL in April of 2021 (originally planned for 2020 launch but boat coordination with USGS was required). The array was comprised of 4-in PVC casing that had been drilled along the length to form a honey-comb pattern of large perforations. The casing was fastened via metal pier clamps (one above surface, one at the bottom of the breach) to a central pier located on the north side of the breach. Within the casing was a series of Hobo temperature sensors at 1 ft spacing attached to a plastic cable. Thin circular plastic discs were placed every 12 inches to separate or partition flows between temperature sensors. The completed installation is shown in Fig. 3.7 and the first set of temperature data is plotted in Fig. 3.8. Additional analyses are planned with this data to augment the CFD analysis and to gain additional insights into the flow structure. As shown in Fig. 3.8, there is clear temperature stratification except when weather events cause vertical mixing and a more uniform temperature profile.

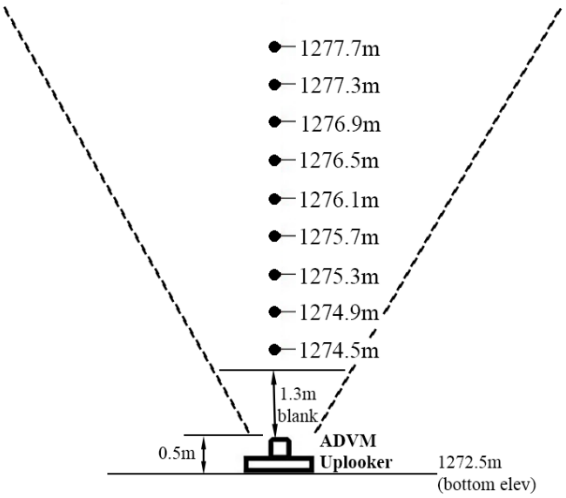

Figure 3.6. Velocity field measurement setup of the ADVM uplooker, which also corresponds to the elevations at which the CFD model is queried (a) (based on information provided by USGS through personal communication).

Figure 3.7. Water temperatures measured in West Crack Breach at 1ft intervals beginning 1ft above the channel bottom and ending 13ft above the channel bottom.

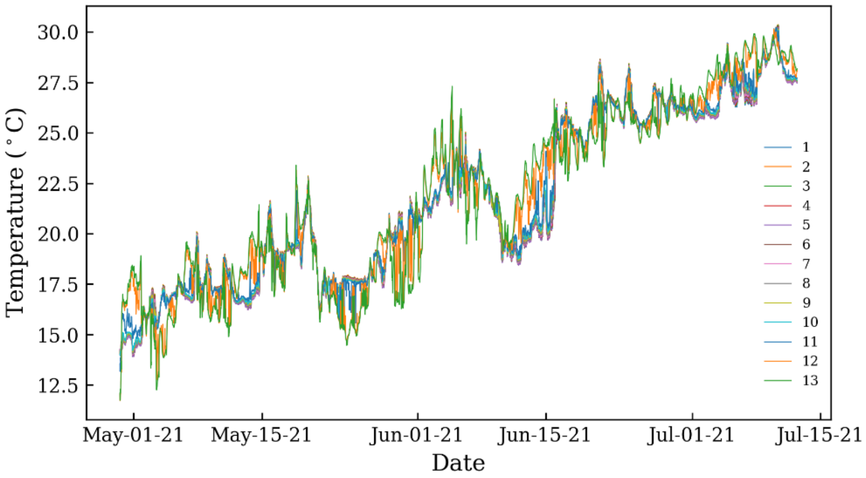

Figure 3.8. Temperature profile data at the West Crack Breach from May to July 2021.

4.0 2D CFD Modeling of the Bidirectional Flow

4.1 2D Model

In this study, FLOW-3D^{TM} by Flow Science, Inc.© was used to numerically simulate the density-driven flow through the Great Salt Lake causeway for all three flow conditions. Geometry for the model consisted of bathymetry provided by USGS and HDR Inc. (bridge and breach designer and contractor). HDR provided as-built bathymetry of the breach and nearly 3400ft of causeway measured shortly after construction (Fig. 4.1a). Bathymetry north and south from the breach was linearly interpolated from USGS bathymetry and joined via CAD as a single geometric surface (Fig. 4.1b and 4.1c).

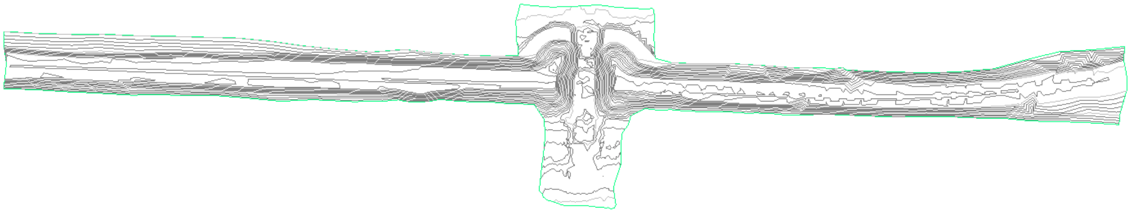

(a) (HDR, 2017)

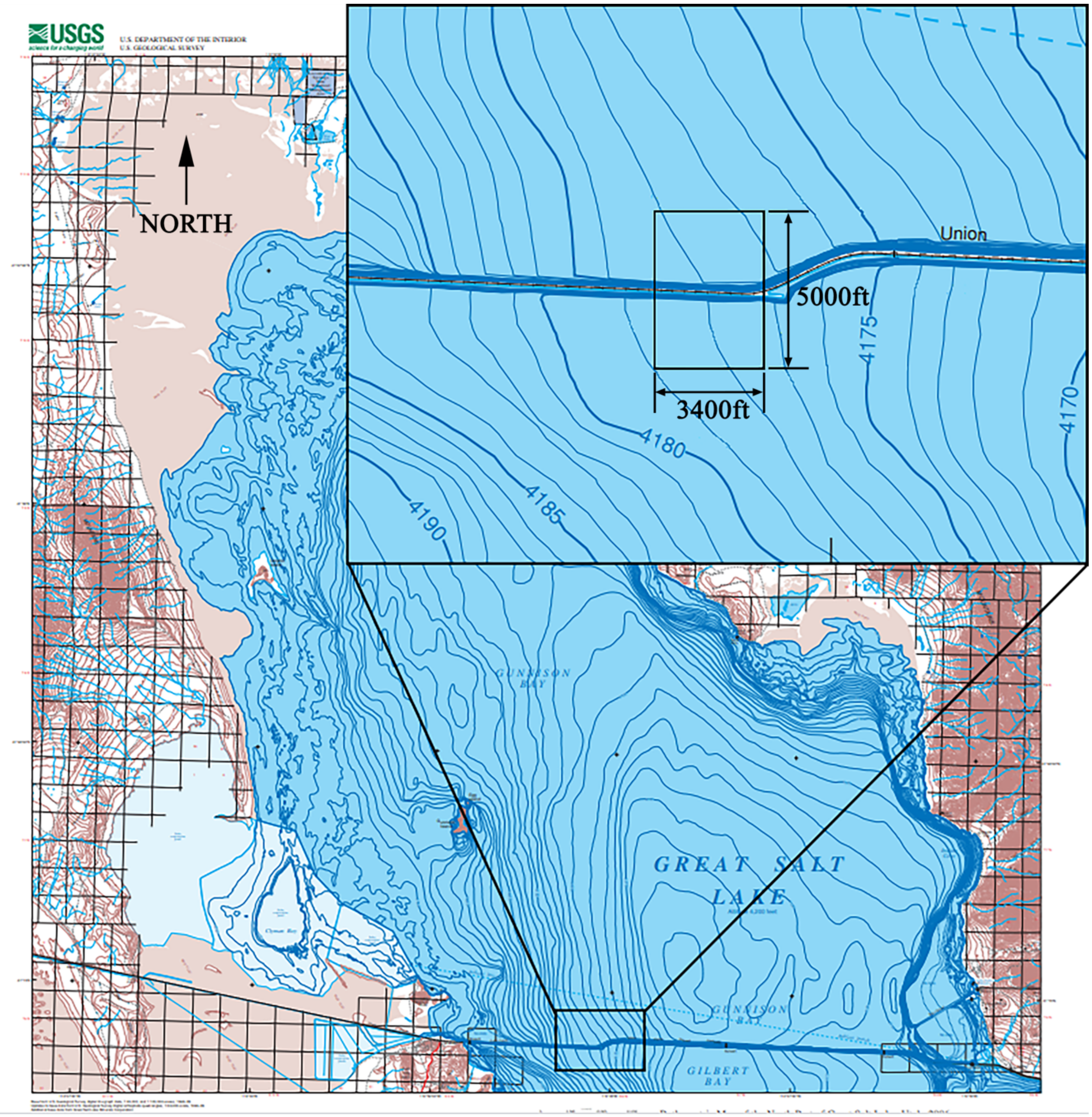

(b) (Baskin and Turner, 2006)

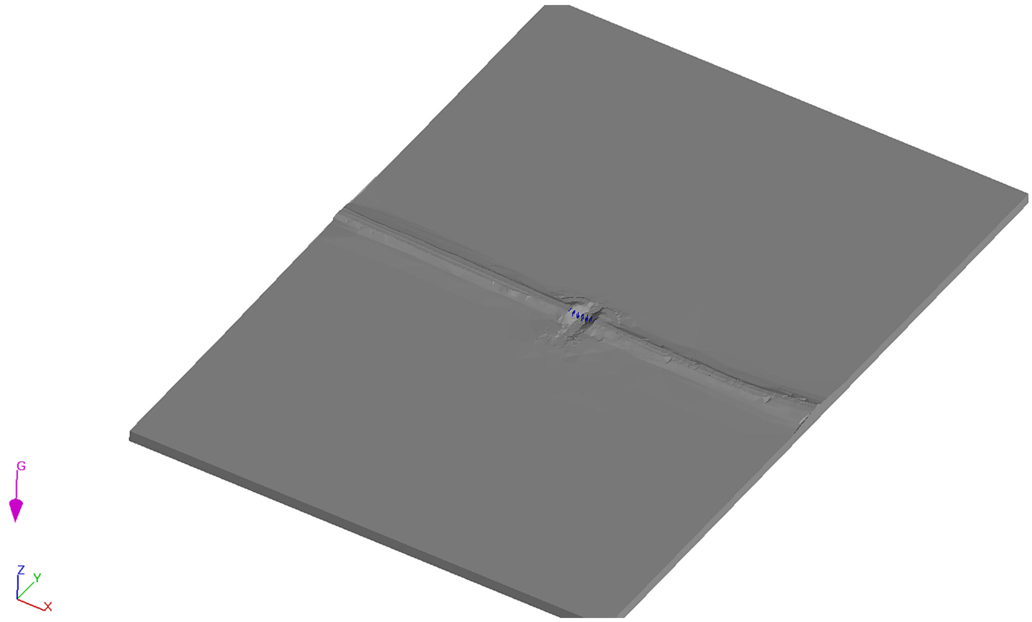

(c)

Figure 4.1. Combination of HDR bathymetry (a) with USGS bathymetry (b) into a combined surface (c) for use in the CFD simulations.

CFD model development included an initial phase in which, different aspects of the model were tested in a 2D setup (employing full 3D equations), with the spanwise direction represented using single cell thick layer of elements. 3D simulations are discussed in subsequent sections. The primary purpose of the 2D simulations was preparation for the 3D simulations by exploring various model parameters and grid convergence, which were later confirmed for suitability in the full domain simulations.

The selected CFD solver used the finite-volume method the FLOW-3D Volume-of-Fluid (VOF) method [29]. The computational mesh consisted of a single block with single-cell width in the E/W direction through the breach center. The north and south boundaries were assigned pressure conditions with separate WSEs and densities, and the east and west boundaries were assigned symmetry conditions. Initial conditions for the north and south lake sides extended from the breach center to the corresponding north and south pressure boundaries (Fig. 4.1).

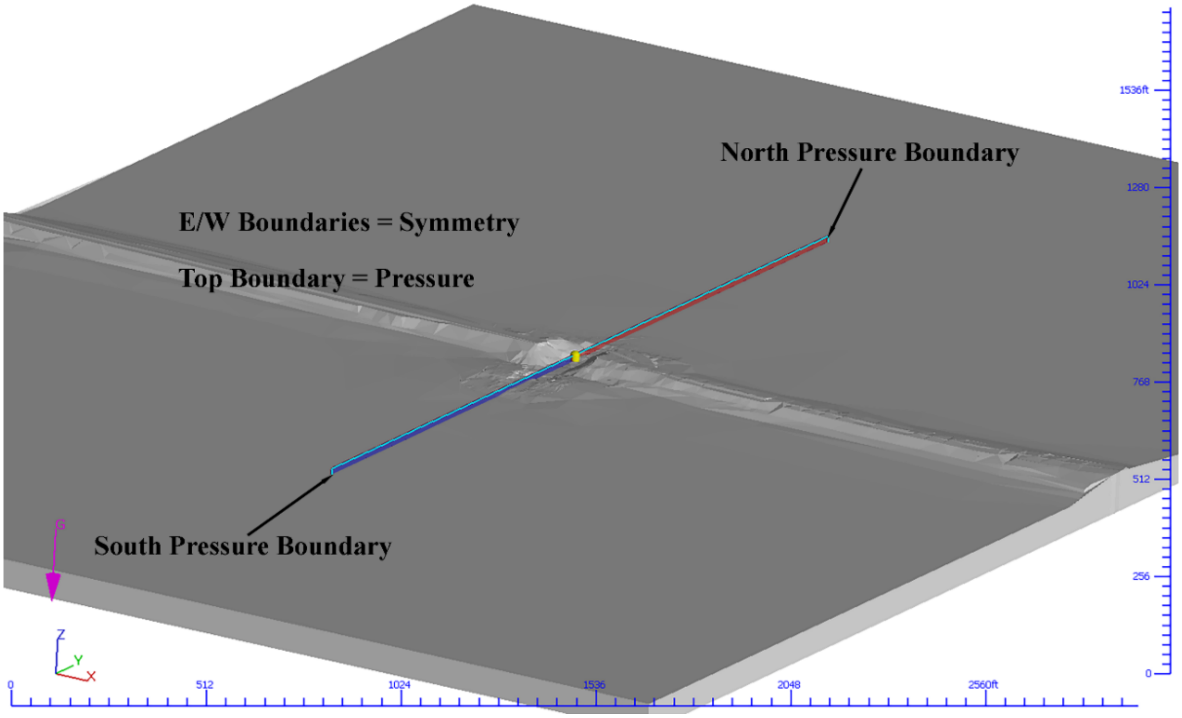

Figure 4.1. Model setup for two-dimensional simulations. The initial conditions are shown as blue and red regions that meet in the breach at t = 0 seconds simulation time.

For this effort, the size of the cell mesh, the turbulence closure scheme, the density evaluation model, and the momentum advection scheme are all critical components that were systematically evaluated when constructing the CFD model.

First, the 2D simulations were used to explore appropriate cell sizes and a grid independence study. The domain was discretized uniformly for each cell size, with eight cubic cell sizes ranging from 1ft to 0.1ft (Table 4.1). Only cell size was adjusted between each simulation with all other parameters left unchanged. Probes placed in the breach center measured flow velocities for juxtaposition of simulation results to field data. A comparison of steady-state velocities showed a differential in fluid velocity until a cell size of about 0.5ft. Further refinement of mesh cell size below 0.5 ft caused minimal change in fluid velocity, so convergence was assumed to have been achieved at 0.5ft.

Table 4.1. Summary of grid convergence study

Sim (#)	Turbulence	ρ_S (kg/m^3)	ρ_N (kg/m^3)	EL_S (m)	EL_N (m)	Cell size (m)	Cell count
1	*k*-ω	1056.5	1159.6	1277.9	1277.8	0.30	49,400

2	*k*-ω	1056.5	1159.6	1277.9	1277.8	0.23	83,208
3	*k*-ω	1056.5	1159.6	1277.9	1277.8	0.18	134,323
4	*k*-ω	1056.5	1159.6	1277.9	1277.8	0.15	192,400
5	*k*-ω	1056.5	1159.6	1277.9	1277.8	0.12	286,000
6	*k*-ω	1056.5	1159.6	1277.9	1277.8	0.09	528,687
7	*k*-ω	1056.5	1159.6	1277.9	1277.8	0.08	696,800
8	*k*-ω	1056.5	1159.6	1277.9	1277.8	0.03	4,368,000

Initial results are presented in Fig. 4.2 where streamwise or y-velocities are compared at four locations to the field data obtained by USGS. As illustrated, for this model setup at most probe locations, a mesh finer than about 0.5 to 0.6 ft is not necessary. With the entire velocity profile plotted as a function of grid size, we observe the classic over resolution of the domain for cell sizes smaller than about 0.25 ft (Fig. 4.2).

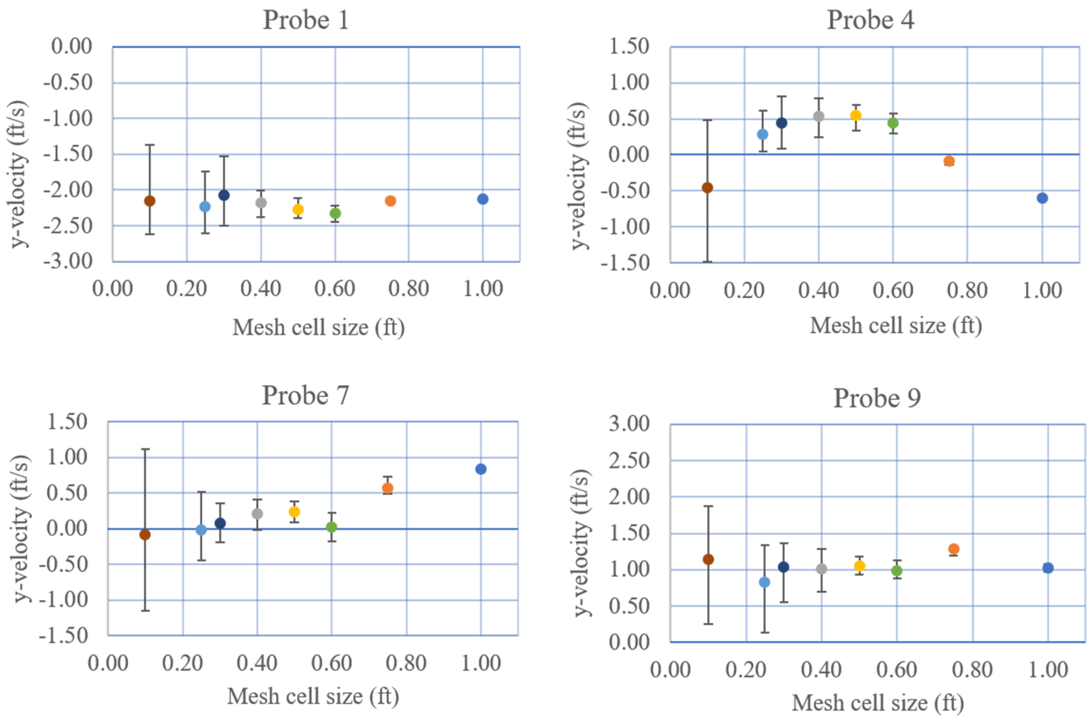

Figure 4.2. Mesh convergence for 2D simulations. Only four of the nine probe data are shown, but the remaining five probe data show similar trends of convergence near the 0.5ft cell size. The plot whiskers represent the range of velocity fluctuation in the

simulation, and the scatter points are the average velocities recorded by the probe.

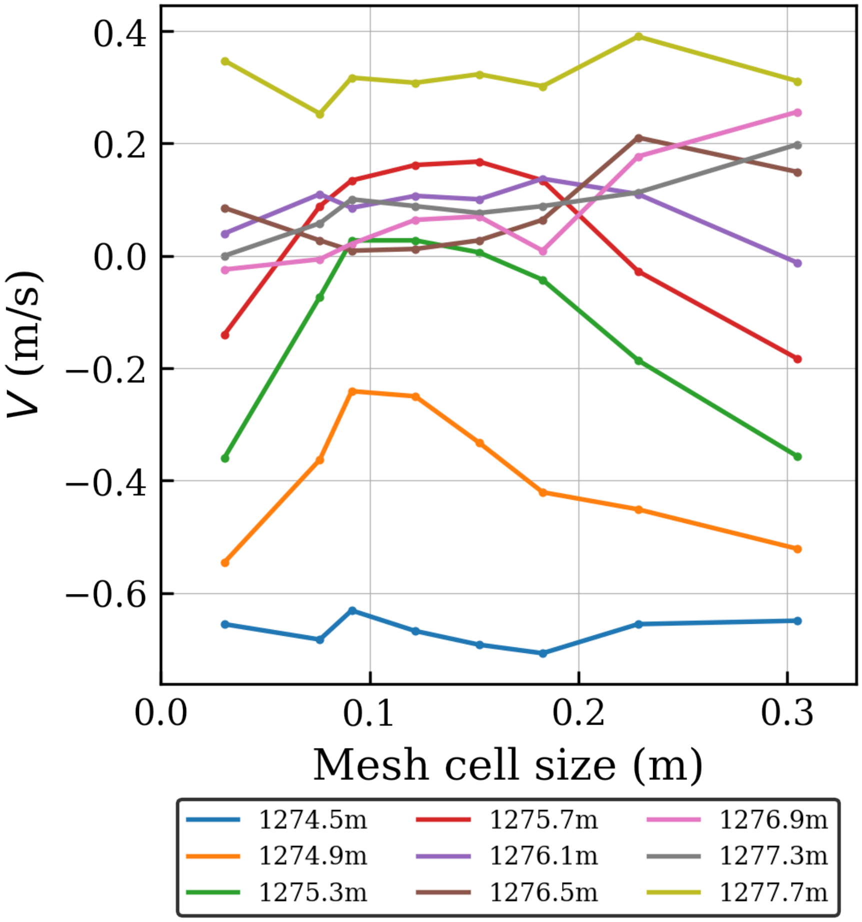

Figure 4.3. Velocities as a function of cell size illustrating over-refinement of the domain.

Flow3D provides multiple models for the computation of viscous stresses and turbulence quantities in the numerical solution. The models provided include *k*-ε, *k*-ω, *Renormalized Group k-ε (RNG- k-ε)*, and *Large Eddy Simulation (LES)* (Flowscience, 2008). These models were tested in the 2D simulation and compared via flow velocity in the same manner as the cell-size sensitivity simulations (Table 4.2). As anticipated due to the nature of these two closure schemes, the k-ε and the RNG k-ε, schemes had unsatisfactory performance (relative to field data) as shown in Fig. 4.4 for bidirectional flows. Interestingly, use of the LES model (compared to k-ω) resulted in reduced simulation clock times by about 30%. Although the k-ω showed promising levels of agreement to field data, the LES scheme provided improved resolution by resolving main turbulence features except for subcell eddies. Due to these factors, the turbulence closure used for the final 3D model was LES. Details of the LES solver include: it is the non-dynamic Smagorinsky model [30,31] that computes all turbulent flow structures that can be resolved by the computational grid, and the sub-grid turbulence effects are modeled by kinematic eddy viscosity, $v_T=(cl)^2S$, where c is the Smagorinsky coefficient defined as 0.1 [32], l is the sub-grid length scale and S is the strain rate tensor; the first-order momentum advection scheme and first-order volume-of-fluid advection were used with an implicit pressure solver with GMRES subspace size of 15, interblock boundary coefficient of 0.25, and volume fraction cleanup of 0.05.

Table 4.2. Summary of turbulence scheme testing

Sim (#)	**Turbulence**	**ρ_S (kg/m^3)**	**ρ_N (kg/m^3)**	**EL$_S$ (m)**	**EL$_N$ (m)**	**Cell size (m)**	**Cell count**
9	*k*-ω	1056.53	1159.60	1277.90	1277.75	0.15	192,400
10	*LES*	1056.53	1159.60	1277.90	1277.75	0.15	192,400
11	*k*-ε	1056.53	1159.60	1277.90	1277.75	0.15	192,400
12	*RNG k*-ε	1056.53	1159.60	1277.90	1277.75	0.15	192,400

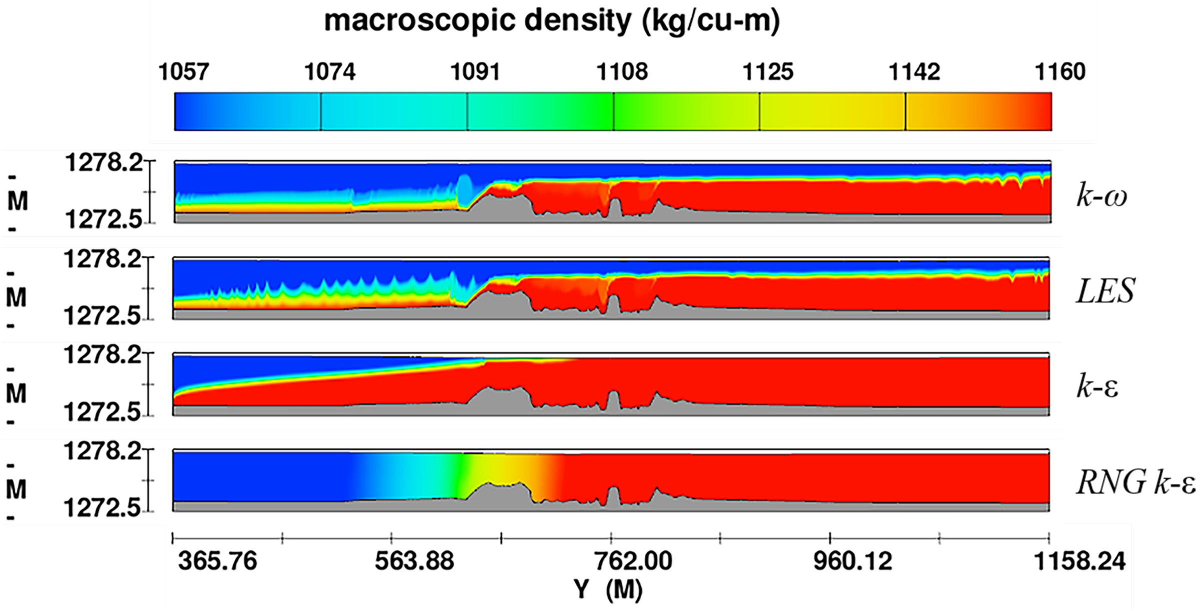

Figure 4.4. Illustrated results of the four turbulence closure schemes simulated in this study. The LES scheme was ultimately chosen for use in 3D simulations.

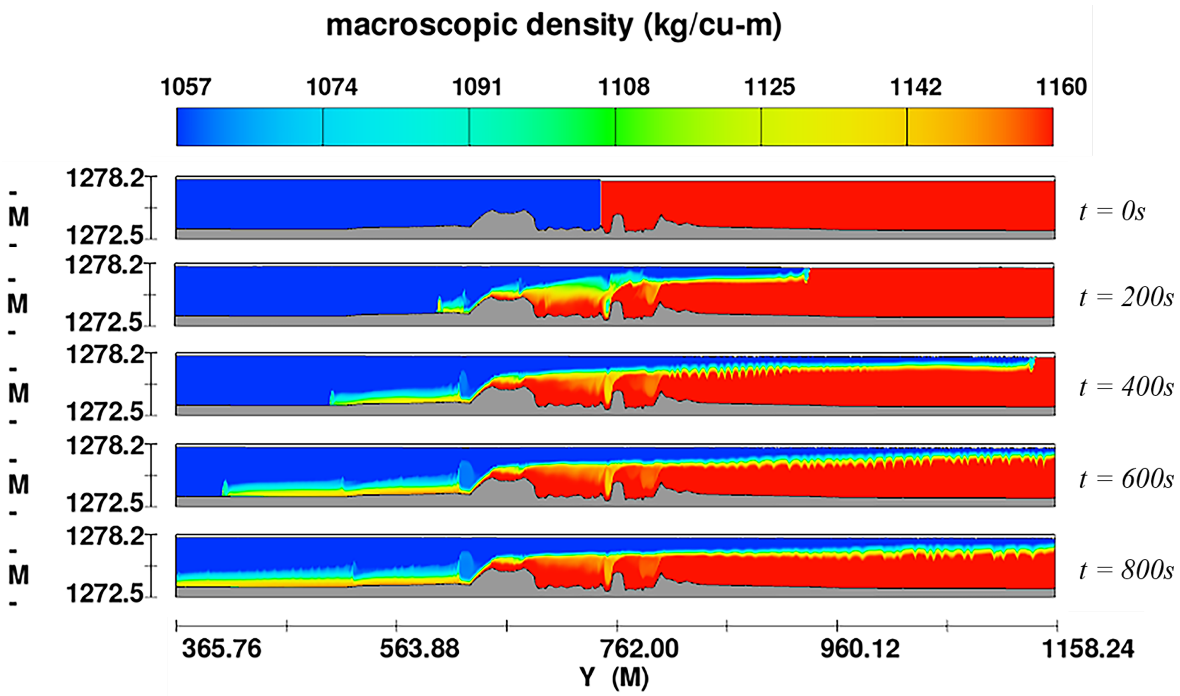

Figure 4.5. Evolution of the bi-directional flow case in a 2D simulation from 0 to 800 seconds with a 0.5ft cell size and LES turbulence closure.

With a cell size and turbulence scheme selected, density models could be explored. This solver has four options for density evaluation. Here were tested the 1) density as a function of hydraulic parameters (i.e., temperature, etc.), 2) a first-order approximation, and 3) a second-order monotonicity preserving approximation (Table 4.3). Initial results indicated unsatisfactory predictions for the first two schemes (Sims 13 and 14) with the second-order monotinicity preserving scheme producing very reasonable results, which was thus selected for final simulations (Figure 4.6).

Table 4.3. Summary of density models tested herein.

Sim (#)	ρ Evaluation
4	Second-order
13	First-order
14	Function of other quantities (e.g., temperature or scalars)

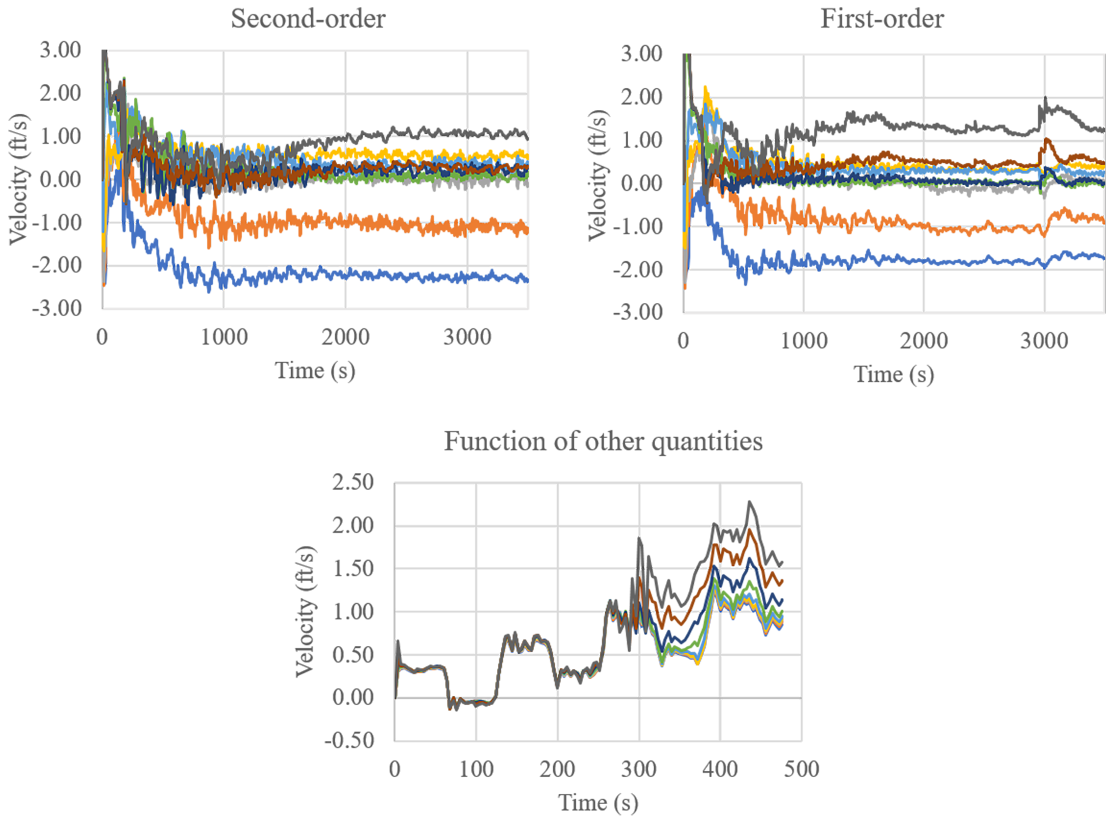

Figure 4.6. Visual comparison of density models via velocity timeseries where the second-order model produced the most satisfactory results. The different colored lines in the plots represents the nine velocity probes.

With the fully constructed 2D model, steady-state results were studied to formulate appropriate model extents for the 3D simulations, specifically the distance required between north and south boundaries. An example of simulation results is presented in Fig. 4.5.

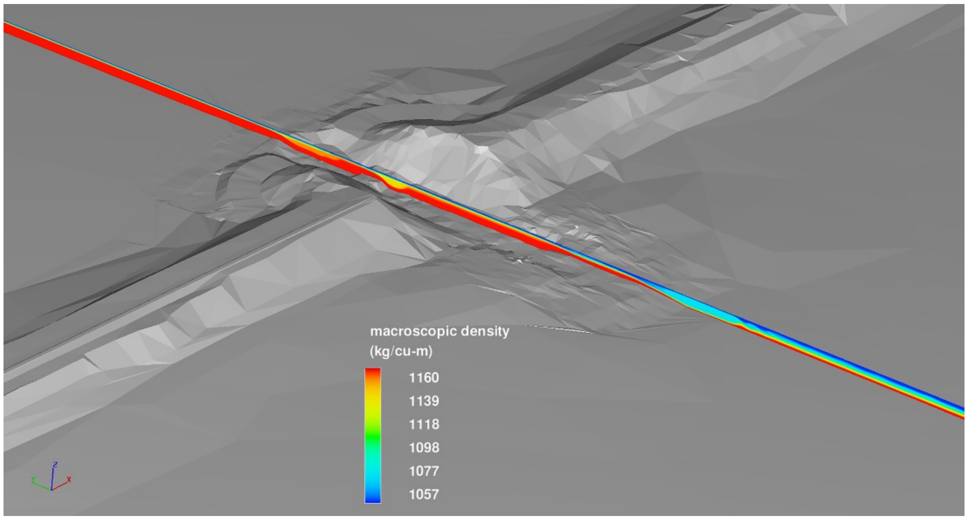

Figure 4.5. Results for consideration of north and south boundary condition distances from breach.

5.0 3D CFD Model of the Bidirectional Flow through the breach

Modeling work on bi-directional flow through the breach has been reported in a paper submitted to the Journal *Water* by MPDI on June 30, 2021. At the time of issuing this report this manuscript was under review. Following is the paper as submitted.

CFD Model of the Density-driven Bidirectional Flows through the West Crack Breach in the Great Salt Lake Causeway

Michael Rasmussen[1], Som Dutta[2,*] and Brian Crookston[3,*]

[1] Research Assistant, Dept. Civil and Environ. Engineering, Utah Water Research Laboratory, Utah State University. michael.rasmussen@usu.edu
[2] Assistant Professor, Dept. Mechanical and Aerospace Engineering, Utah State University. som.dutta@usu.edu
[3] Assistant Professor, Dept. Civil and Environ. Engineering, Utah Water Research Laboratory, Utah State University. brian.crookston@usu.edu
* Correspondence: brian.crookston@usu.edu, Tel: +1 (435) 797-0247; som.dutta@usu.edu, Tel.: +1 (435) 797-0583

Abstract: Stratified flows and the resulting density-driven currents occur in the natural environment and also as a result of urbanization. At the Great Salt Lake, the northern and southern portions of the lake are divided by an east-to-west causeway that disrupts natural lake currents and significantly increases salt concentrations in the norther portion. To support management efforts to address rising environmental and economic concerns, the causeway was recently modified to include a new breach that typically exhibits a strong density-driven bidirectional flow pattern. To obtain much needed insights into the hydraulic performance of this hydraulic structure and the exchange between the two sections of the lake, a field campaign coupled with CFD modeling was undertaken. Results from this study indicate that the vertical velocity profile in the breach is sensitive to density differences between flow layers along with breach geometry and water surface elevations. The CFD model was able to accurately represent the bidirectional flows through the breach. Also included herein are details of the CFD model and refinement efforts along with velocity profile prediction results.

Keywords: density-driven flow; saltwater lake; bidirectional flow; stratification, large eddy simulation, West Crack Breach.

5.1. Introduction

Saline lakes represent 23 percent by area, and 44 percent by volume of all lakes on Earth [1]. Saline lakes can be found in diverse environments, though most of them are located in places that have arid climate. Some of the major saline lakes are Caspian Sea, Great Salt Lake (GSL) in Unites States, and Lake Urmia in Iran. Importance of these lakes can be gauged from the fact that often times they are close to urban centers (e.g. GSL is near the

Salt Lake City), and have thriving shipping, fishing, mineral and tourism industries. In addition to direct economic benefits, saline lakes and the surrounding swamp provide unique habitats for birds and other fauna. Climate-change propelled droughts and increases in human consumption, have resulted in shrinkage of these saline lakes across the world [2]. Some examples of saline lake desiccation due to over consumption that has occurred in the last 100 years are, shrinkage of Lake Urmia in Iran [3], and Owens Lake in California that was entirely desiccated in 1940. One of the first recorded incident of human consumption leading to saline lake desiccation is in the Tarim Basin, leading to the downfall of the Loulon Kingdom in 645 CE [4]. Desiccation of saline lakes and the resulting alarming decline in important ecosystems have been documented in the past [2,5,6]; and this has led to a renewed interest in preserving these systems, as some of these saline lakes have seen calamitous decline in lake levels in the last 20 years [7]. The current paper is about a hypersaline lake, the Great Salt Lake, which is also facing aforementioned issues related to over consumption, eventual potential desiccation and related ecosystem issues [2]. The ecosystems are under imminent threat due to ongoing drought and increasing water usage, leading to more than 10 ft drop in lake level in the last 150 years, and the water level currently being at the lowest in recorded history.

More specifically the current paper describes the effort to develop a computational fluid dynamics (CFD) model of the density-driven flow that occurs at the breach in the causeway of the GSL. Going forward, in section 2 we discuss about GSL it's unique features, in section 3 we discuss about the methods we used to develop the CFD model of the density-driven flow, and in section 4 we discuss the results from the model and what it tells us about the dynamics of the flow through the breach in the GSL.

5.2. Great Salt Lake and the West Crack Breach

The Great Salt Lake (GSL) is a significant resource to Utah, contributing more than \$1.3 billion annually to Utah's economy through mineral extraction and its world-leading brine shrimp production [8,9]. Recreational attractions connected to GSL also play a significant part in the local economy, primarily due to GSL's unique ecosystem that provides habitat for almost 5 million migratory birds every year [10]. As a result, significant research and monitoring efforts have been undertaken for decades [11], especially since the construction of the Union Pacific Railroad Company (UPRR) causeway in 1959. This causeway divides approximately 1/3 of the lake from the southern portion (see Fig. 1), which has altered its characteristics including natural circulation, water and salt balances, etc. [12]. For example, since 1959 the northern part of GSL has become more saline while salt content of the southern arm, which has significant freshwater inflows, has reduced [11,13]. Two culverts were built in the causeway in 1959 to facilitate water connectivity between the northern and southern sections. Subsequently another breach created in 1984 near the western end of the causeway. The original culverts were decommissioned in December 2013 with a new West Crack (WC) Breach (see Fig. 2) opened in December 2016. During these 3-years, water surface elevation, WSE, of the North-arm of the lake was observed to have dropped significantly, illustrating the importance of the flow though the breach on the water and salt balance of GSL. Despite the different connections between the North and South arms of the lake, the saline concentration of the North has on-an-average been significantly higher than the South (~ 100 kg/m^3).

The difference in salinity between the northern and southern part of the GSL results in formation of density-difference driven flow through the breach in the causeway. In general, WSE of the South-arm is always higher than the North-arm. If there was no difference in density between the two sides, the flow through the breach would have been South to North. Higher density of the North-arm results in the water coming from the south to float over the North-arm water, and the water from the north to plunge below the water coming from the south. This results in a bi-directional flow through the breach, where in the upper water column typically flow north while the lower portion flows south. Consequently, this flow results in formation of a stable and stratified but hydraulically complex deep brine layer (DBL) in the southern arm of GSL. The connection between the salinity-difference driven gravity-current flowing through the breach and formation of DBL is succinctly illustrated by the disappearance of the DBL during a three-year period when the last culvert was closed in December 2013 and a new breach was opened in December 2016 [15].

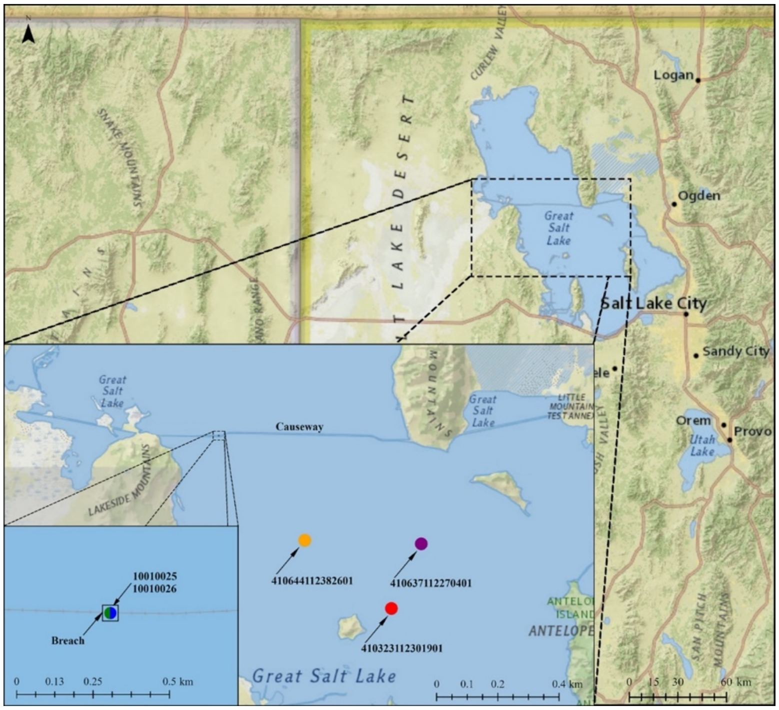

Figure 5.1. The Great Salt Lake located in the state of Utah in USA. Insets show the causeway that divides the lake into a Northern-arm and Southern-arm, and the location of the West Crack (WC) Breach in the causeway. Also shown are the USGS measurement stations, data from which was used to select the boundary conditions of the CFD model.

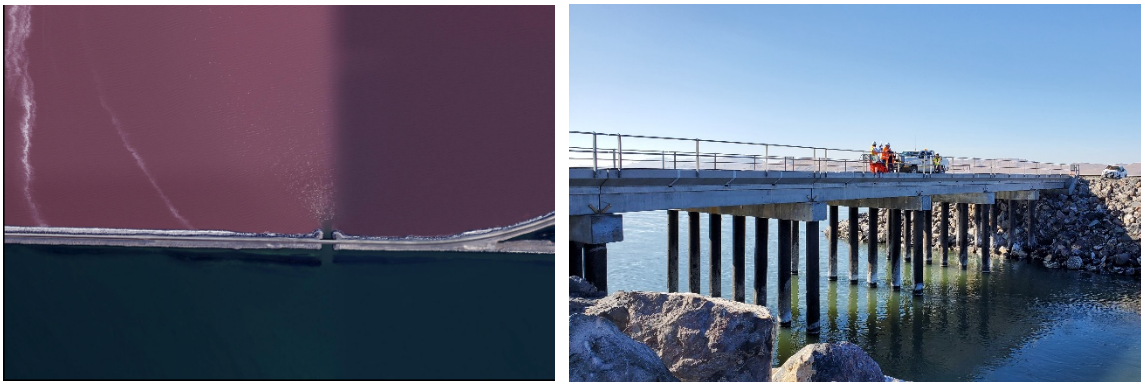

(**a**) (**b**)

Figure 5.2. (a) Satellite image of the causeway and the West Crack (WC) Breach. The hyper-saline northern arm of the lake has a pink color due to presence of microbes that thrive in the hyper-saline environment [14] (b) Picture of the WC Breach taken from the northern side of the causeway, during the field-campaign in October 2020. The picture illustrates the structure of the breach, showing the three rows of six piers that are in the water, and affect the flow going through the breach.

Although the DBL may be influenced by other factors, analyses had shown strong sensitivity of salinity in the southern arm of GSL to the geometry and adjacent submerged berms of the new breach [16]. This essentially points to the fact that the new WC Breach is the location where most of the exchange of water and salt occurs between the North and South arms of the lake. Thus, in order to correctly estimate the water and salt mass balance between two parts of the lake, it is imperative to model the flow and salt transport through the WC Breach accurately. Accurate estimation of the total flow and salinity through the WC Breach is needed for accurate prediction of the long-term health of its ecosystem and related industries via the evolution of GSL's salinity profile [17,18]. Additionally, a better understanding of the bidirectional buoyancy-driven flow through the WC breach will provide us insights into how the openings in the causeway could be used for effective brine management in the future [16,19].

One of the first dedicated hydraulics model to estimate the flow going through the culverts in the causeway was developed by Holley and Waddell [20], and later advanced by Loving et al. [11] to estimate GSL salinity and bidirectional flow through the causeway. While that model is capable of calculating the bidirectional flow through the causeway openings, those calculated flows are not in good agreement with measured flows, especially for the WC breach. This is not completely unexpected due to the fact that Holley and Waddell's model was developed for bi-directional flow through culverts, which are significantly different geometrically from the bridges built over the breach (see Fig. 2). The newer connections have components (e.g., piers) that are expected to make the flow highly three-dimensional (3D). Thus, the complex bidirectional flow though the WC breach warrants the use of a computational fluid dynamics (CFD) modeling approach, in order to accurately capture the dynamics. In spite of the flow in the GSL being highly three-dimensional and complex, there has only been very few studies that have used 3D hydrodynamic modeling to study different aspects of the lake. Spall [21,22] used 3D hydrodynamic models that incorporated baroclinic and barotropic responses, tidal forcing, wind stresses, Coriolis effects, surface thermal forcing, inflows, outflows, and transport of salt, heat and passive scalars. Spall investigated the effects of surface heat flux and wind forcing on the spatio-temproal variations in the flow patterns within the southern arm of GSL. Neither of the studies modeled the spatio-temporal dynamics of the DBL in GSL, or the bidirectional flow passing through the causeway openings. Thus, our goal is to develop a model that captures the complex interaction between the bidirectional flow and the hydraulics structure of the breach. The model will be developed using the multiphase CFD solver that can track the interface (fluid-fluid or fluid-air) between different phases. These solvers have been used successfully to study variable density flows and various complex multiphase flow problems, e.g., multiphase sewage flows in water reclamation plants [23], estimation of flow discharge through hydraulic structures [e.g., 24], etc. In the next section we discuss the steps taken to develop the computational fluid dynamics (CFD) model, including field measurement campaign, which was required to understand the flow and measure data that was used to define boundary conditions of the CFD model.

5.3. Materials and Methods

5.3.1. Field Campaign

Field measurements were conducted at the WC Breach of the Great Salt Lake causeway, located approximately 53 km northwest of Salt Lake City and about 27 km west of Promontory Point. At this location lake depths were on average less than about 6 meters. Field data were collected from October 1, 2020 to June of 2021 with supplemental data obtained from USGS who have been collecting field data from the time the WC Breach was completed. Field observations were made via shore access and by kayak (see Fig. 3) and prioritized specific conductance (σ) measurements at and adjacent to the breach along with visual observations.

Water samples were collected initially at multiple locations north and south of the causeway breach at specific flow depths (e.g., 0.15 m to 4.6 m at approximately 0.3 m spacing), with samples processed back at the lab for Total Dissolved Solids (TDS). Locations were GPS located and depths were measured with a field tape accurate to ±30 mm. A simple tubing and syringe system was used to collect samples, with the tubing placed at the prescribed depth and then a volume secured in the large syringe. Flushing was performed between each sample to minimize contamination and ensure accurate sampling. Shoreline samples were also collected and processed in the laboratory. Direct measurements were then juxtaposed to indirect continuous salinity measurements using an In-Situ AquaTroll 600 multi-parameter water quality sonde, which measured σ and was calibrated to ±5%. Instrumentation location was selected following general measurements via kayak approximately 1 km north and 1 km south of the breach and approximately 2 km east-to-west, which indicated generally uniform σ values adjacent to the density-driven currents through the breach. Therefore, it was appropriate to install monitoring locations approximately 400 meters from the breach on the south bank of the causeway for southern water measurements (Fig. 3a) and on a pier approximately 10 m from shore and 800-m west of the WC Breach. Instruments were placed within a perforated PVC casing that allowed for any natural water circulation. The southern instrumentation casing extended out into the lake and was approximately 1/3 the flow depth from the lake bottom. Field data was sampled initially at 30 min interval continuously, but after November 2021 field data was sampled at 10 min intervals continuously; field data was downloaded from the sondes every 1–2-month period with routine calibrations performed before relaunching the sondes.

The U.S. Geologic Survey (USGS) and other government agencies have field records of the Great Salt Lake extending more than 50 years. Regarding the 2017 breach, USGS field records include various buoys measuring σ at monthly intervals, located in the vicinity of the causeway (see Figs. 4 and 1) but at a considerable distance from the breach. In addition, samples were collected by USGS at the breach on monthly intervals (locations 10010026 and 10010025) since 2017. At the breach an acoustic doppler velocimeter meter (ADVM) uplooker was placed by USGS in 2017 adjacent to a row of piers and at the bottom of the breach, directly below the north face of the bridge decking (see Fig. 6). The ADVM sensor is approximately 0.5 m from the lakebed and begins sampling 1.3 m from the lake bottom. USGS estimates velocity profiles at this location using the Index Velocity Method [25] with corresponding index rating and 9 vertical bins. During this study ADVM data was shared with USU but official review and online publication of the data by USGS was underway and had not yet been completed. Due to uncertainty in the specific location of the ADVM relative to the pier in the transverse direction, the CFD portion of this study considered vertical profiles at 10 distances from the respective piers, as noted in Fig. 6b. In addition to salt concentrations and velocity measurements, USGS monitored WSE at an adjacent pier in the northern section (See Fig. 3b), at a pier to the east of the breach in the southern section, and at the breach (see Fig. 2(a) and 5).

The CFD model required density inputs for the boundary conditions on the north and south sections of the lake. Field instrumentation provided the needed SC measurements that were converted to corresponding water densities, ***ρ*,** using linear interpolation of USGS data [26], data provided to USGS by HDR who performed monitoring during and after construction (27,28) and data collected for this study (Utah State University – Utah Water Research Laboratory (UWRL)), see Fig. 4. In addition to SC, the TDS was also referenced for selecting density, with a conversion from TDS to density via a conversion equation employed by USGS [11]. The final range of north and south densities selected for testing was based upon the UWRL continuous SC measurements and the monthly TDS measurements.

(**a**) (**b**)

Figure 5.3. Field sampling for SC and TDS from shore in the southern portion (a) and at a pier in the northern portion (b) of the Great Salt Lake.

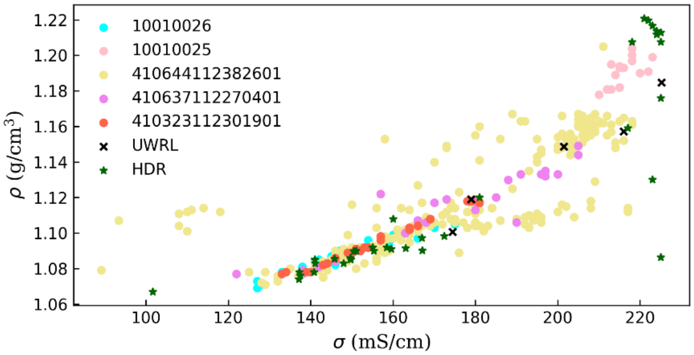

Figure 5.4. Saltwater density *ρ* as a function of specific conductance *σ* for the Great Salt Lake.

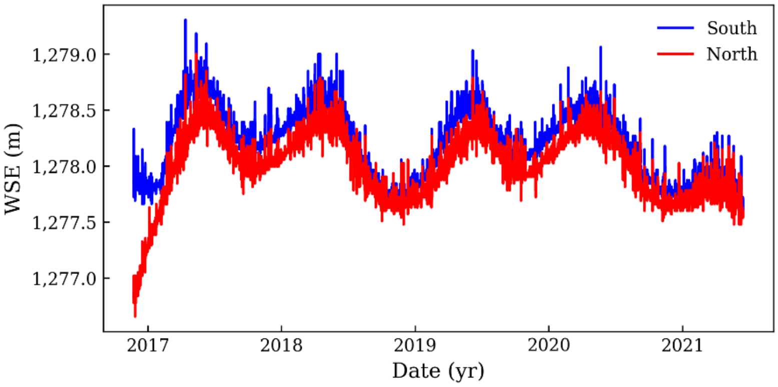

Figure 5.5. Northern and southern water surface elevations WSE for the Great Salt Lake at the West Crack (WC) Breach (completed in 2017).

As shown in Figs. 4 and 5, some variability in field measurements have been recorded, which are a function of instrument accuracy but more due to lake dynamics and temporal variations in response to climate, weather patterns, etc. These factors were considered when selecting boundary conditions for the computational fluid dynamics (CFD) simulations and a case that is representative of the density driven bidirectional flow patterns and specific velocity data and corresponding WSEs along with a sensitivity analysis of densities and velocity profile location.

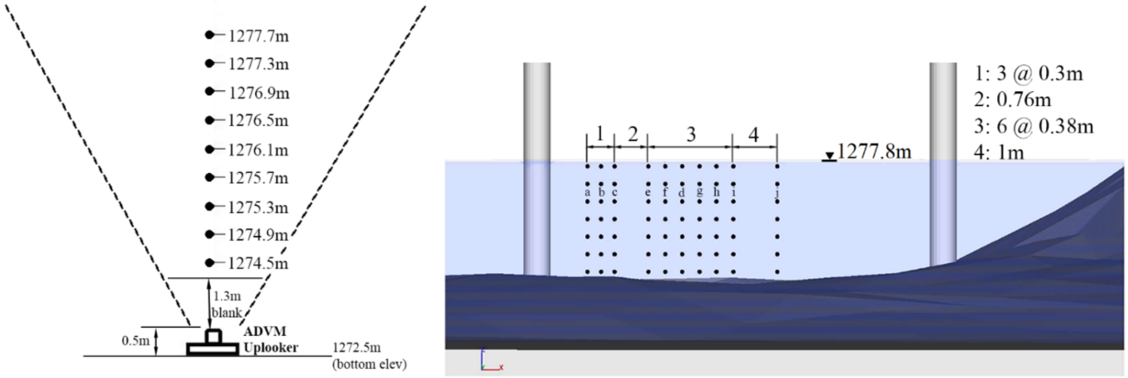

(a) (b)

Figure 5.6. Velocity field measurement setup of the ADVM uplooker, which also corresponds to the elevations at which the CFD model is queried (a) (*based on information provided by USGS through personal communication*) and sampling locations in the CFD model (b) due to uncertainty in ADVM location relative to bridge piers.

5.3.2. Numerical Model

In this study, FLOW-3D^{TM} by Flow Science, Inc.© was used to numerically simulate the density-driven flow through the Great Salt Lake causeway for the typical bidirectional case (surface flows to the north with subsurface flows to the south). CFD model development included an initial phase in which, different aspects of the model were tested in a 2D setup, with the spanwise direction represented using single cell thick layer of elements. This was followed by the main phase in which, 3D simulations were conducted with the computational domain covering the entire breach, and adjacent portions of the lake and causeway.

The selected CFD solver used the finite-volume method and the model was a single-fluid model with the free-surface resolved spatially and temporally via the FLOW-3D Volume-of-Fluid (VOF) method [29]. This study tested four turbulence schemes, the k-ε, the RNG, k-ω, and LES. Turbulence closure schemes were tested for both the 2D and 3D modeling phases, and the best performance (relative to field data) was given by the LES and the k-ω model. Interestingly, use of the LES model (compared to k-ω) resulted in reduction in wall-clock time of the simulation by 1.3x for 2D simulations. Due to these factors, the turbulence closure used for the final 3D model was LES. The LES in the solver is the non-dynamic Smagorinsky model [30,31] that computes all turbulent flow structures that can be resolved by the computational grid and the sub-grid turbulence effects are modeled by kinematic eddy viscosity, $v_T=(cl)^2S$, where c is the Smagorinsky coefficient defined as 0.1 [32], l is the sub-grid length scale and S is the strain rate tensor. The first-order momentum advection scheme and first-order volume-of-fluid advection were used with an implicit pressure solver with GMRES subspace size of 15, interblock boundary coefficient of 0.25, and volume fraction cleanup of 0.05. The bathymetry, causeway, piers, etc. were numerically represented as solids by the Fractional Area/Volume Obstacle Representation (FAVOR) method.

This solver has four options for density evaluation. Here were tested the 1) density as a function of hydraulic parameters (i.e., temperature, etc.), 2) a first-order approximation, and 3) a second-order monotonicity preserving approximation. Initial results indicated unsatisfactory predictions for the first two schemes with the second-order monotinicity preserving scheme producing very reasonable results, which was thus selected for final simulations.

5.3.2.1. Model domain and boundary conditions

The 3D numerical domain was 295 meters by 275 meters centered on the breach (see Fig. 7). Hexahedral cells of different dimensions were employed to resolve different parts of the domain (see Fig. 8a). Grid convergence [33] was studied for both 2D and 3D models; the grid convergence for the 2D model included eight cell sizes refinements ranging from 0.3 m to 0.03 m, and the grid convergence for the 3D model included three cell size refinements ranging from 0.3 m to 0.08m. Results from the grid-convergence indicated solution independence was achieved for cells of 0.15 m (see Fig. 8b). For this study the final discretization of the main phase domain was comprised of two mesh blocks of 0.3 m cubic cells linked in series, with two nested blocks with 2:1 cell refinement at the boundary (i.e., the second nested block cell size was $x=y=z=0.08$ m). The number of cells in the final 3D simulations were 23.4 million.

The northern boundary conditions were assigned a WSE_N of 1,277.76 m and northern saltwater density $\rho_n=1180.22$ kg/m^3, based upon field data (noted in red region as P in Fig. 7). Similarly, the southern boundary conditions were assigned a WSE_S of 1,277.82 m, or 0.06m higher and a southern saltwater density $\rho_s=1097.75$ kg/m^3 (noted as P in blue region in Fig. 7). The bottom boundary condition was defined as a wall and the top boundary was a Dirichlet boundary condition with atmospheric pressure set to 0=gage pressure. Note that diffusion at the fluid-no fluid interface is managed by a fluid-volume correction (<±0.01%). Initial boundary conditions were defined for each main mesh block with fixed water surface elevations and water densities corresponding to the respective northern and southern boundaries.

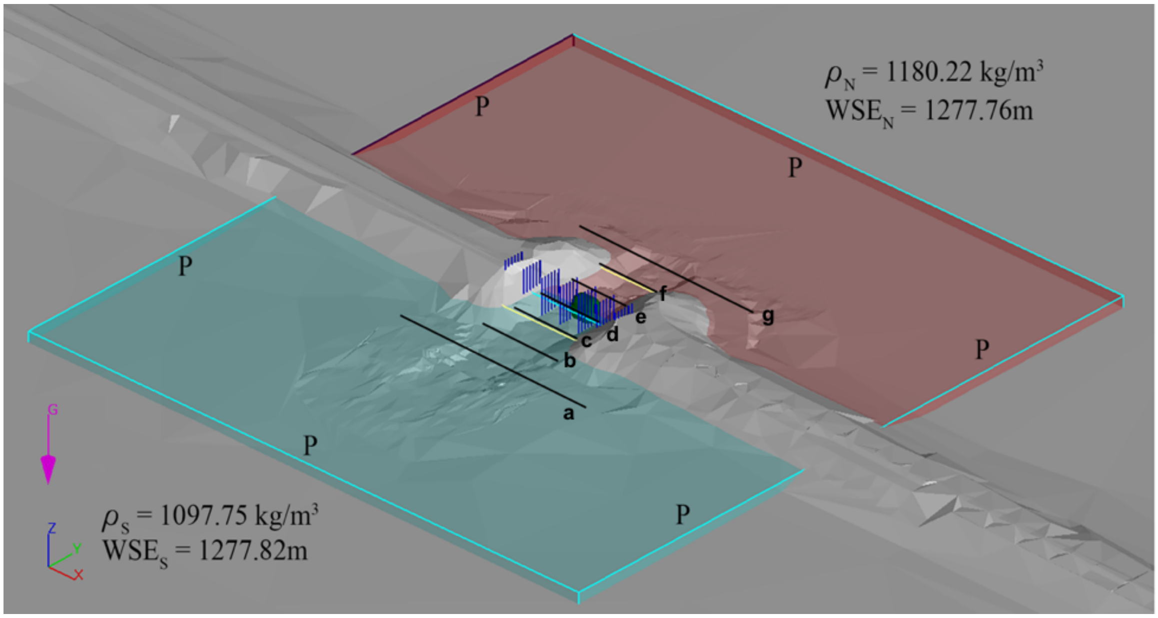

Figure 5.7. The computational domain with boundary conditions of the CFD model. In the coordinate system of the model, positive X corresponds to West-to-East direction, and positive Y corresponds to the South-to-North direction. The locations (bold-black lines) of seven vertical slices (12 m apart) in the model are also noted, which were used for analyzing the flow through the breach.

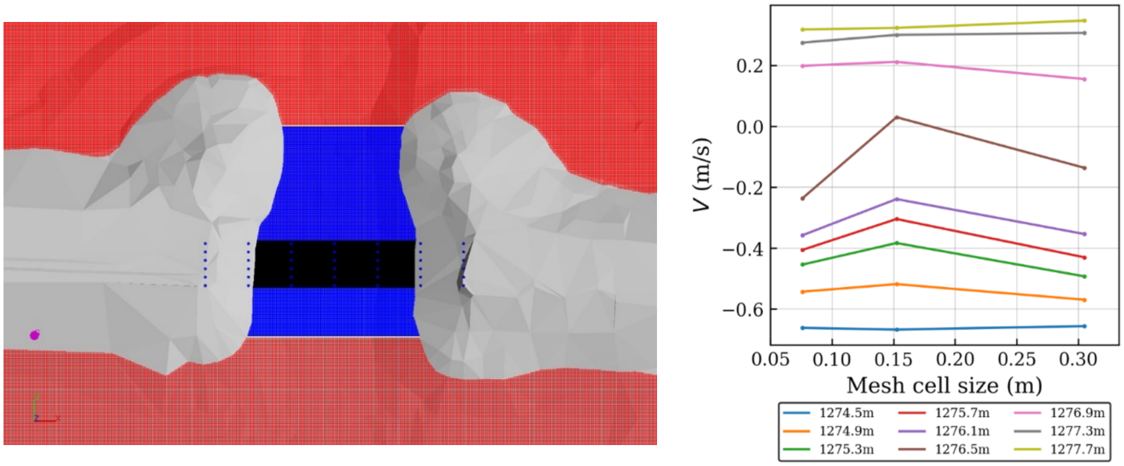

(a) (b)

Figure 5.8. An overview of the final mesh configuration with nested blocks (a). The red region has mesh size of 0.3 m, the blue region within the breach has mesh size of 0.15 m, and black region of the domain is the region surrounding the bridge piers and has a mesh size of 0.08 m. (b) The grid convergence for the 3D simulations shows that a 0.15 m mesh should be enough to capture the flow field. Velocity at nine different elevations in

the water-column was monitored. Apart from one point, the streamwise (y-direction) velocity did not show appreciable change with reduction of mesh size from 0.15m to 0.08 m. The vertical elevations at which the velocity is probed correspond to the elevations at which the USGS ADVM measured streamwise velocity (see Fig. 6).

5.4. Results and Discussion

5.4.1. Model comparison with field measurement

Once the mesh resolution study was completed, the veracity of the 3D model was tested against the unpublished velocity profile measured at the WC breach by USGS using the ADVM uplooker (see Fig. 6). Several unknown parameters needed to be considered while comparing the CFD model results with the field measurements. First, the exact density difference $\Delta\rho$ between the Northern and Southern arms of the lake was uncertain. As described in section 3.1 (and Fig. 4), the field data indicated that there was a small range of possible density values for the Northern part of the lake. This was primarily due to lack of robust relationship between specific conductance (σ) measured at the GSL and the corresponding extreme salinity, which is near saturation. Naftz et al. [34] developed an equation of state for the hypersaline water of GSL, but that equation only performs well if the salinity of the water is already known. Thus, for the current study 5 cases with different densities between the North and South arms of the lake were simulated (see Table 1). The basis of choosing ρ_S and ρ_N values was discussed in section 3.

Table 5.1. Density difference $\Delta\rho$ and the difference in WSE imposed for the 3D simulations. A range of $\Delta\rho$ was tested due to field data and corresponding uncertainty in estimation of ρN.

Sim (#)	ρ_S (kg/m^3)	ρ_N (kg/m^3)	$\Delta\rho$ (kg/m^3)	**ΔWSEL** (m)
1	1097.8	1169.9	72.1	0.061
2	1097.8	1180.2	82.4	0.061
3	1099.8	1195.7	95.9	0.061
4	1097.8	1200.8	103.0	0.061
5	1097.2	1212.7	115.5	0.061

The second source of uncertainty was the exact location of the ADVM uplooker, with respect to the central column of piers at the WC Breach. It is known that the uplooker is located slightly north to the northern-most pier of the central column, and within 1.5-2.5 meters east of the that pier. In order to ascertain the potential location of the uplooker, we probed the streamwise velocity at multiple locations east of the pier (see Fig. 6). The computed streamwise velocities at four different distances from the central pier, and for different density difference have been plotted in Fig. 9. The results clearly show that the correct density difference $\Delta\rho$ between the Northern and Southern sides of GSL is ~ 82.4 kg/m^3, and the location of the uplooker is about 1.5 m east of the pier. Given the uncertainty in measuring field data, the comparison between the measured and computed velocity (V)profiles is satisfactory (Fig. 10). The only points in the profile that do not compare well, which have more than 50 percent error, are V at the interface of the North-South and South-North flows. This is not unexpected, as there is some uncertainty in the field velocity profile at this interface and this section is more challenging to simulate numerically as there is a sudden change in density and velocity. However, these results are considered satisfactory for management efforts of the lake.

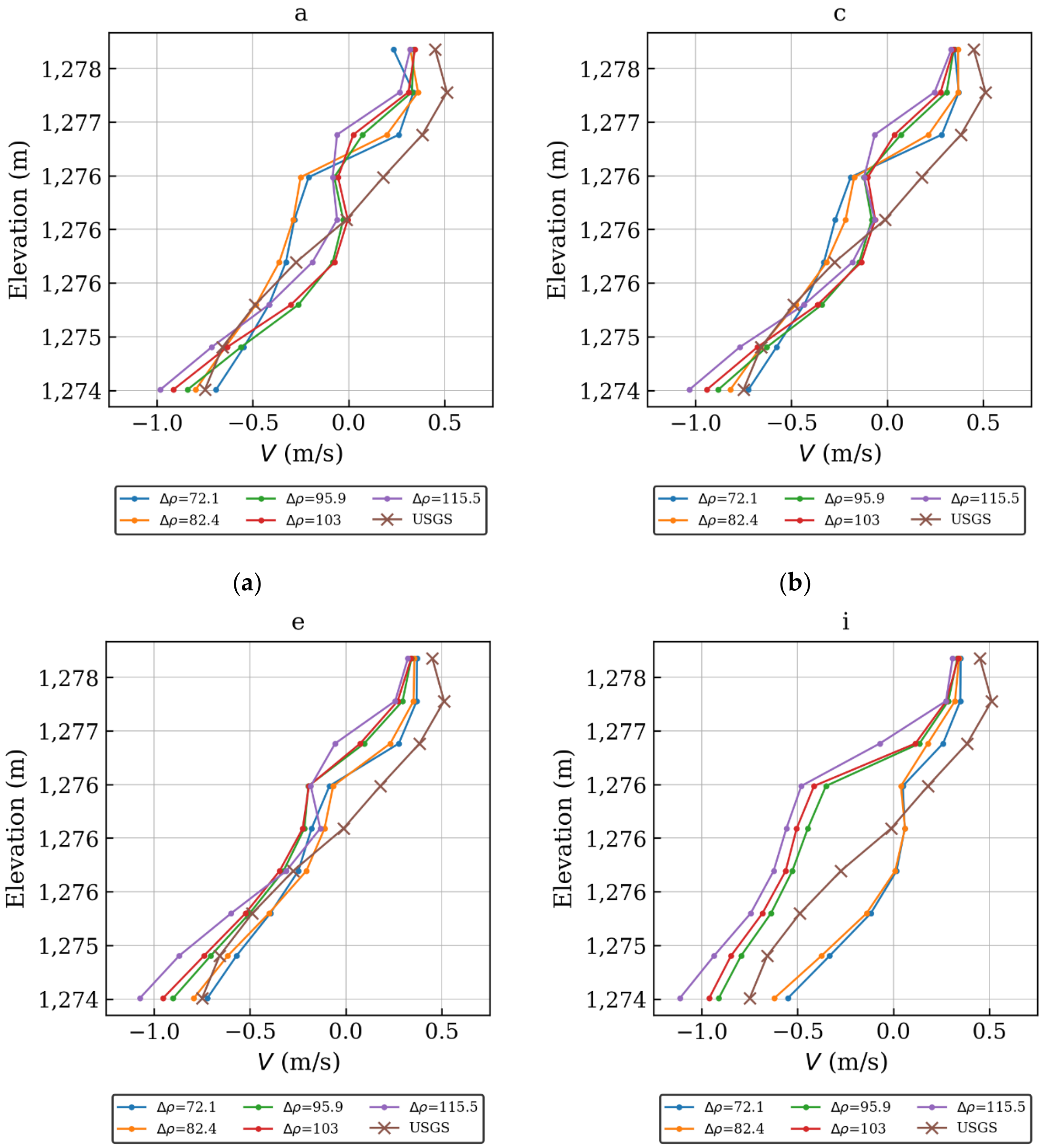

(**a**) (**b**)

(**c**) (**d**)

Figure 5.9. CFD predicted velocity profiles at the WC breach for different density differences at profile location a, (a), at location c, (b), at location e (c), and at location i (d). Note that locations c and e show good agreement with USGS field data, for density difference ~ 0.16 slugs/ft^3 (which is case 2, 82.4 kg/m^3).

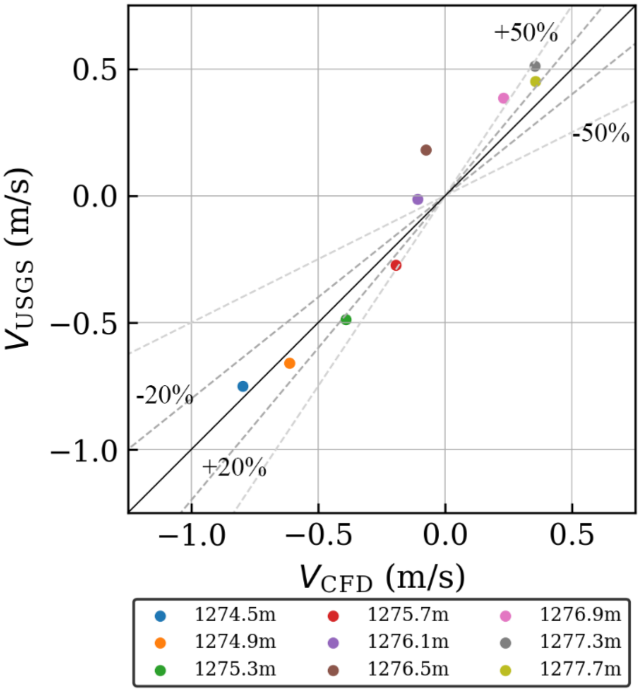

Figure 5.10. Comparison between the measured (V_{USGS}) and computed (V_{CFD}) velocity profiles. For all but one point in the profile, V_{CFD} is within 20-50 percent of the measured field data. The R^2=0.9578.

5.4.2. Simulated Flow Field

Based on the field observations (see Fig. 11), the general dynamics of the flow is clear; hypersaline water from the north side of the lake plunges below the south side water that is flowing South to North (S-N) just before entering the breach. This creates a relatively thick and denser bottom current flowing North to South (N-S), and a relatively thinner and less dense S-N current flowing at the surface. As this bottom current exits the breach it spreads laterally and thins as it travels south, with its thickness decreasing with distance away from the breach. To provide a general overview of the hydrodynamics at the breach, ρ and the South to North (y-direction) velocity V has been plotted for the vertical-plane orthogonal to the X-axis and going through the center of the breach (Figs. 12 and 13). CFD results clearly capture the dynamics observed in the field and the simulation results provide more insights about formation of the density drive bidirectional flow pattern (N-S and S-N currents). In agreement with field observations, the thickness of the distinct layers of the flow are similar with the bottom layer being relatively thicker with a non-negligible velocity. The hypersaline water from the north can be seen to maintain its thickness some distance from the causeway, eventually forming the deep brine layer (DBL). The hypersaline northern current also appears to go through a subsurface hydraulic jump just after it plunges and before entering the central part of the breach, which is a function of the submerged dike or berm specifically placed to manage flows through the WC Breach. The hypersaline N-S current can be seen to accelerate just after plunging under the incoming S-N flow. The S-N flow also accelerates while going through the breach and can be seen to travel much further into the northern side than the density plots indicate. In order to get a clearer view of the flow evolution, vertical planes orthogonal to the S-N (y-direction) direction have been plotted at 12-meter interval starting south of the breach (Fig. 14).

Figure 5.11. View from the WC breach at the Great Salt Lake Causeway looking north. Surface flows move from south to north (bottom to top of photo). Note the radial pattern at the surface, providing indication of the relatively lighter water from the south floating over the heavier northern water. Similar radial mixing pattern at the surface can also be observed in the CFD simulation (see fig. 12).

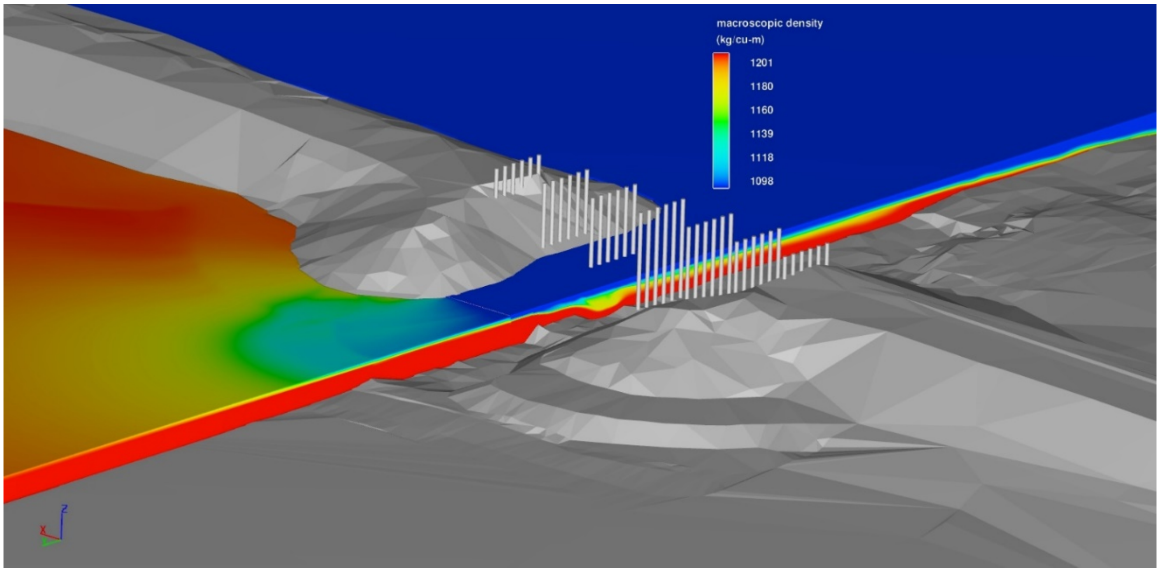

Figure 5.12. Isometric view of the density within the lake. Higher density water from the north (red) plunges below the lighter water (blue) from the south. At the breach the thickness of both the layers are similar. The layer of water from the south gets appreciably thinner once it enters the northern arm. The hypersaline water from the north can be seen to maintain its thickness longer, eventually forming the deep brine layer (DBL). The hypersaline northern current also seems to go through a subsurface hydraulic jump, just after it plunges and before entering the central part of the breach.

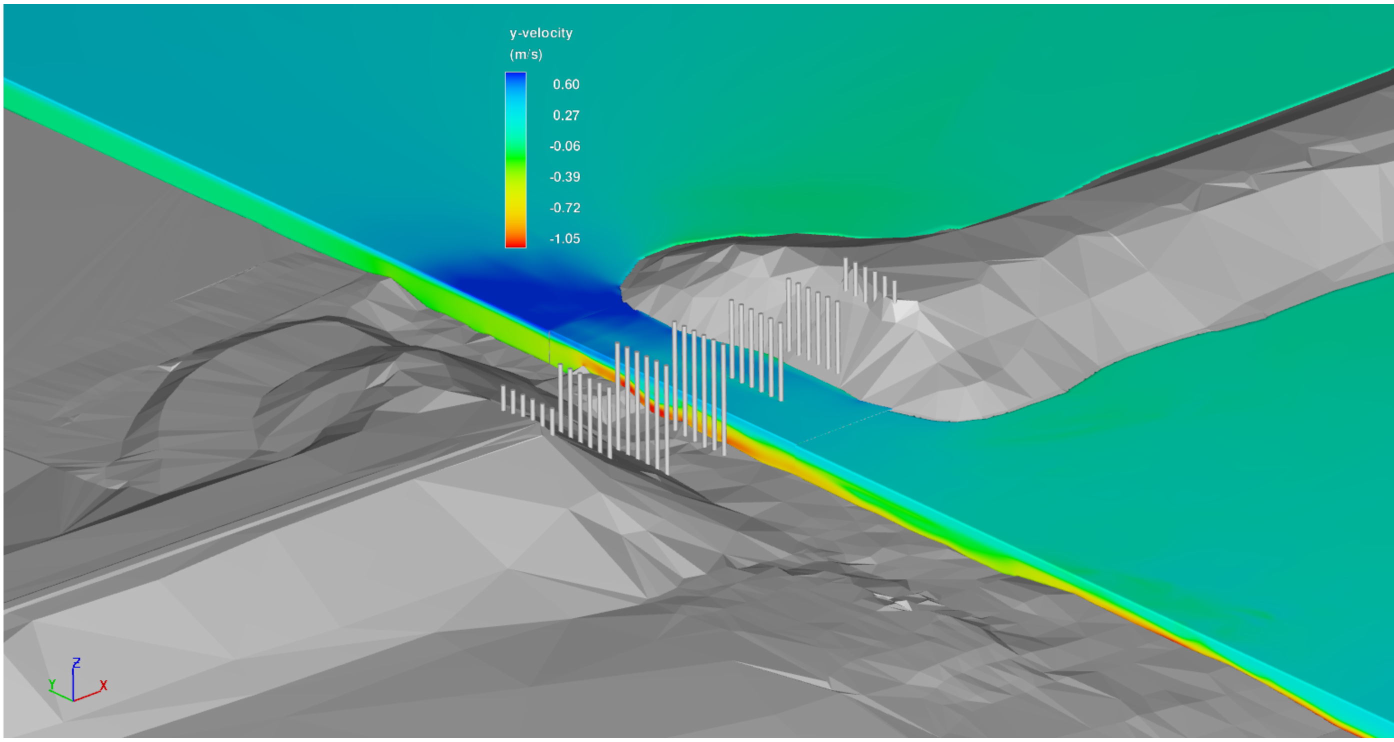

Figure 5.13. Isometric view of the velocity *V* in the y-direction, with the positive velocity corresponding to the south to north flow. The hypersaline N-S current can be seen to accelerate just after plunging under the incoming S-N flow. The S-N flow also accelerates while going through breach (blue) and can be seen to travel much further into the northern side than the density plots indicate.

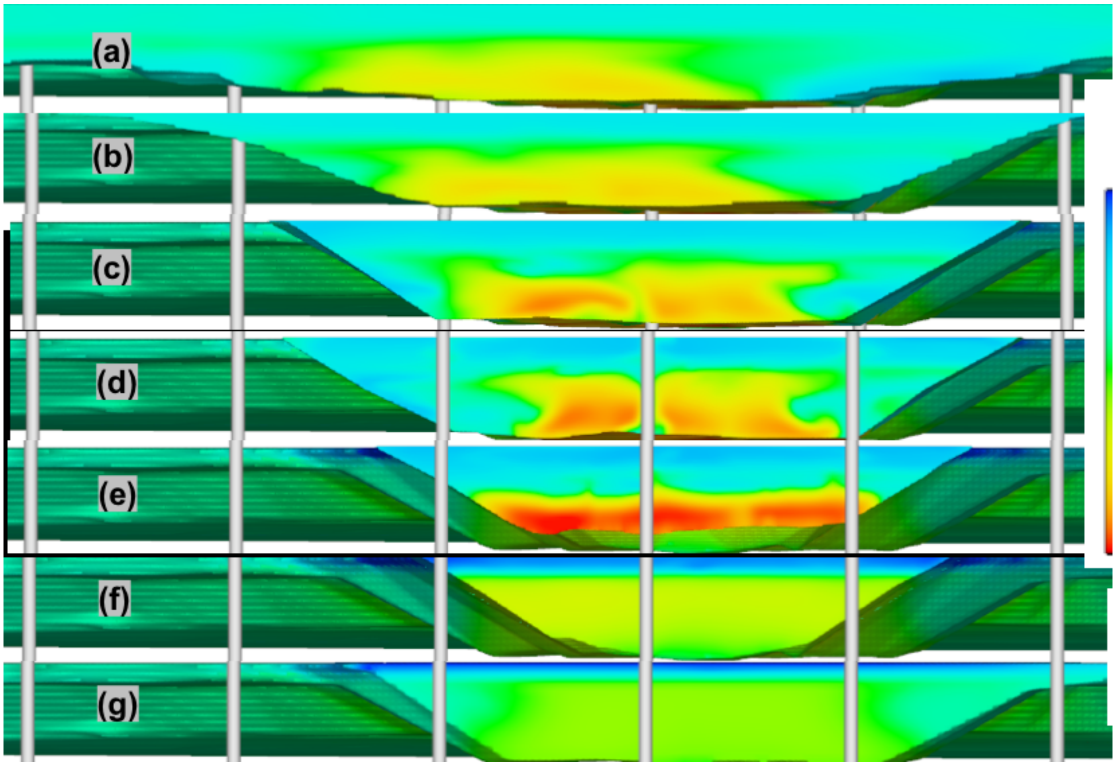

Figure 5.14. Velocity *V* in the y-direction at seven different vertical slices along the breach. The location of the slices has been illustrated in Fig. 6. (a) Is the southernmost slice, and every slice after that is at a distance 12 m northward. The N-S current is coming out of the plane, and the S-N current is into the plane. Slices (a-c) are to the south of the piers, slices (e-g) are to the north of the piers, and slice (d) is within the columns of piers. The effect of the piers on structure of the flow, especially the N-S bottom current can be seen between (e) and (d). Effect of the piers can still be observed in (c), even though the slice is south to the piers. By the time the N-S current comes to slice (b), the effect of the piers is not evident. From (b) to (a), the hypersaline current does not show much change.

It can be observed that the flow has a clear bidirectional form, though the thickness of the N-S bottom current and the S-N top layer flow change spatially. In panel (a) we observe a distinct N-S flowing bottom layer which is still realtively thick, but is primarily confined to the center of the channel. The flow has expanded laterally a little, but is still mostly flowing along the channel dredged up during the construction of the breach. Charting the evolution of the N-S current, starting from the northernmost slice (fig. 14g), we can observe the current accelerate and decrease in thickness as it approaches the breach. The current accelerates from about 0.2 m/s to about 1 m/s in a span of 24 meters. The approximate densimetric Froude number of the bottom current at the location of the uplooker measurement is about 0.7. Thus, there is a chance that the flow might become supercritical while accelerating towards the breach, and then go through a subsurface hydraulic jump. Additionally, the piers of the breach can be observed to have induced mixing and decrease the density stratification. This can be inferred from the sudden increase in bottom layer thickness going from panel (e) to (d). The effect of the piers on the structure of the N-S current can be observed 12 meters downstream (see fig. 14c). Going further south, the bottom current further decreases in thickness (see fig. 12) but retains velocities around 0.8-0.9 m/s. This N-S current transforms to become the dense bottom layer (DBL).

The S-N flow, which is confined to the top layer of the water column, can be observed to be accelerating while approaching the breach. While flowing among the piers, the S-N flow covers more area in the cross-section that the N-S flow. Though by the time the flow comes through the breach (fig. 14e), the water column gets divided into two distinct parts. Within 24 meters, the S-N current gets confined within 1/10th of the water column, while accelerating to about 0.6 m/s. This S-N current now has a densimetric Froude number of about 1.2 and is supercritical.

In order to further understand the flow at different elevations, density and velocity magnitude at four different layers have been plotted in Fig. 15.

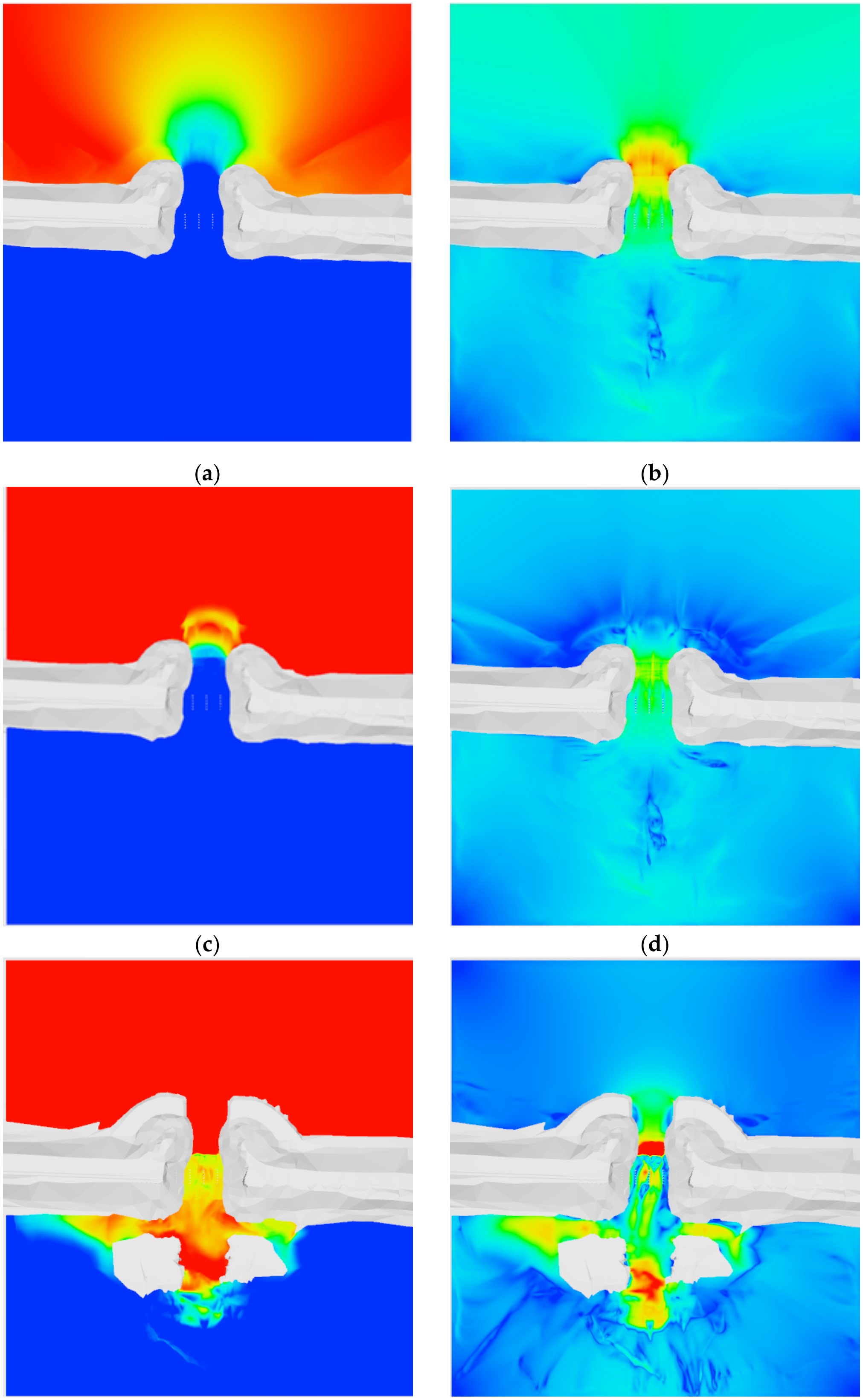

(a) (b)

(c) (d)

(e) (f)

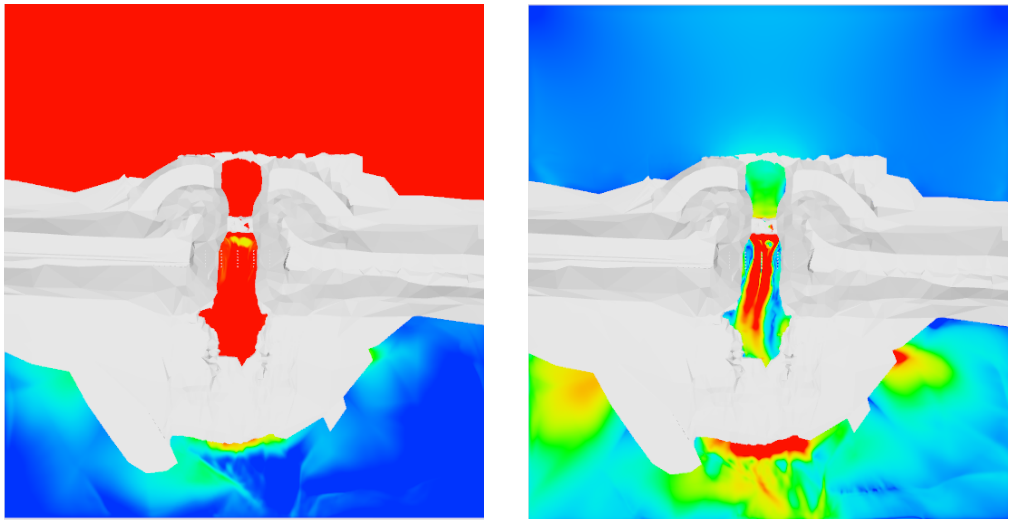
(g) (h)

Figure 5.15. CFD density driven bidirectional flow results for density (left column) and velocity magnitude *V* (right column) in plan at the water surface (a) and (b), at 1.1 m from the surface (c) and (d), at 2.5 m from the surface (e) and (f), and near the bottom of the lakebed (3.4 m from surface) (g) and (h). Note that the bottom elevation of the breach is 1272.5 m.

The flow at the surface is primarily S-N, and the current can be seen to be expanding radially away from the WC breach. This matches with the field observations, where this current confined to the top-layer of the water column was observed up to 1000 meters north of the WC breach. The next layer at 1.1 m from the surface, the flow has relatively high velocity while going through the breach, especially once the S-N flow has crossed the piers and is get-ting pushed further up in the water-column. The next layer at 2.5 m below the surface, the flow is dominated by the N-S current, though there are parts where this layer is near/passing-through the interface between the two currents. The bottom current can be observed to be coming through the breach and continuing along the central channel (see Fig. 15g), while some of it spills over to the sides. This plunging of the N-S current might lead to overturning of the flow, leading to enhanced mixing near the edges of the breach on the south side (see fig. 14c). The N-S current also seem to go through relatively high acceleration after entering the breach (fig. 14f), and this is also the zone where the N-S current plunges towards the bottom. The layer at about 3.4 m from the surface (fig. 15g, h) is dominated by the bottom hugging N-S current. We observe high velocities within the dredged channel. We also see how the bottom topography affects the bottom current. We can observe the distinct berm (bottom sill) in North of the breach, which can used to reduce the N-S flow, and consequently the DBL. Though how effective it will be, or how high it has to be made to impact the DBL is not well understood. This CFD model, can be modified and used to study the effect of the berm. It can also be observed that the bottom of the lake on the southern side increases in elevation just after the dredged region of the breach. This will have a significant effect on the mechanism of the DBL formation and will be studied in detail in the future.

5.5. Conclusions

The density-driven bidirectional current through recently completed West Crack Breach at the Great Salt Lake Causeway was simulated with an LES CFD model to support management efforts that include environmental and economic concerns. Modeling was based upon a field campaign and datasets provided by USGS. Results from this study indicate that the vertical velocity profile in the breach had good agreement with the unpublished USGS velocity profile data with an $R^2=0.9578$ generally within 20 to 50%. The model is sensitive to density differences between flow layers along with breach geometry and water surface elevations, which is also the case for lake flows through the WC Breach. The results also indicate that this flow pattern and mass exchange through the breach can be influenced by the submerged dike and that a hydraulic structure rating curve can be successfully developed for hydrologic modeling of the Great Salt Lake.

5.6. Patents

None

Supplementary Materials: none

Author Contributions: Conceptualization, S.D. and B.M.C.; methodology, S.D and B.M.C.; software, M.R., B.M.C and S.D.; validation, M.R., B.M.C and S.D.; formal analysis, M.R., B.M.C. and S.D.; field investigation, B.M.C and S.D.; resources, S.D. and B.M.C.; data curation, M.R.; writing—original draft preparation, B.M.C and S.D.; writing—review and editing, S.D., M.R., and B.M.C.; visualization, M.R.; supervision, S.D. and B.M.C.; project administration, S.D.; funding acquisition, S.D. and B.M.C. All authors have read and agreed to the published version of the manuscript.

Funding: This research was funded by the Utah Department of Natural Resources through the 2020 Division of Forestry, Fire, and State Lands Grant. This research was also funded by the State of Utah though Utah State University and the Utah Water Research Laboratory.

Data Availability Statement: Some or all data, models or code that support the findings of this study are available from the corresponding authors upon reasonable request. Please not that at the time of this study

USGS velocity data was preliminary as it had not yet completed final review and publication of data online per USGS policy.

Acknowledgments: The authors thank Dr. Bethany Neilson and Dr. David Tarboton for their support of this study. The authors are also appreciative to Utah DNR and USGS Great Salt Lake office, specifically Ryan Rowland, Michael Freeman, and Travis Gibson.

Conflicts of Interest: The authors declare no conflict of interest. The funders had no role in the design of the study; in the collection, analyses, or interpretation of data; in the writing of the manuscript, or in the decision to publish the results.

5.7. References

[1] Messager, M. L., Lehner, B., Grill, G., Nedeva, I. and Schmitt, O. (2016). Estimating the volume and age of water stored in global lakes using a geo-statistical approach. *Nat. Commun*. 7, 13603..

[2] Wurtsbaugh, W. A., Miller, C., Null, S. E., DeRose, R. J., Wilcock, P., Hahnenberger, M., and Moore, J. (2017). Decline of the world's saline lakes. *Nature Geoscience*, 10(11), 816-821.

[3] AghaKouchak, A., Norouzi, H., Madani, K., Mirchi, A., Azarderakhsh, M., Nazemi, A., and Hasanzadeh, E. (2015). Aral Sea syndrome desiccates Lake Urmia: call for action. *Journal of Great Lakes Research*, 41(1), 307-311.

[4] Mischke, S., Liu, C., Zhang, J., Zhang, C., Zhang, H., Jiao, P., & Plessen, B. (2017). The world's earliest Aral-Sea type disaster: the decline of the Loulan Kingdom in the Tarim Basin. *Scientific reports*, 7(1), 1-8.

[5] Gross, M., (2017). The world's vanishing lakes. *Curr. Biol. 27*, 43–46

[6] Jellison, R., Williams, W. D., Timms, B., Alocer, J. & Aladin, (2008). N. V. in Aquatic Ecosystems: Trends and Global Prospects (ed. Polunin, N. V. C.) *Cambridge Univ. Press* 94–112

[7] Case, H. L. I. et al., (2013). Salton Sea Ecosystem Monitoring and Assessment Plan Open- File Report 2013–1133, United States Geological Survey

[8] Bioeconomics, Inc., (2012). Economic significance of the Great Salt Lake to the State of Utah. Prepared for State of Utah Great Salt Lake Advisory Council. http://www.gslcouncil.utah.gov/docs/GSL_FINAL_REPORT-1-26-12.PDF

[9] Wurtsbaugh, W., C. Miller, S. Null, P Wilcock, M. Hahnenberger, F Howe. (2016). Impacts of Water Development on Great Salt Lake and the Wasatch Front. White Paper to the Utah State Legislature. Prepared by Utah State University, Utah Division of Water Resources, Salt Lake Community College, and Utah Division of Wildlife Resources.

[10] WHSRN (2016). Western Hemisphere Shorebird Reserve Network. www.whsrn.org

[11] Loving, B.L., K.M. Waddell, C.W. Miller. (2000). Water and salt balance of Great Salt Lake, Utah, and simulation of water and salt movement through the causeway, 1987-98. U.S.G.S Water- Resources Investigations Report 00-4221. Salt Lake City, UT.

[12] Waddell, K.M., E.L. Bolke. (1973). The effects of restricted circulation on the salt balance of Great Salt Lake, Utah. Utah Geological Survey Water Resources Bulletin 18.

[13] Stephens, D. W. (1990). Changes in lake levels, salinity and the biological community of Great Salt Lake (Utah, USA), 1847–1987. *Hydrobiologia*, 197(1), 139-146.

[14] Baxter, B. K. (2018). Great Salt Lake microbiology: a historical perspective. International Microbiology, 21(3), 79-95.

[15] Yang, S., Johnson, W. P., Black, F. J., Rowland, R., Rumsey, C., and Piskadlo, A. (2020). Response of density stratification, aquatic chemistry, and methylmercury to engineered and hydrologic forcings in an endorheic lake (Great Salt Lake, USA). *Limnology and Oceanography*, 65(5), 915-926.

[16] White, J. S., Null, S. E., and Tarboton, D. G. (2015). How do changes to the railroad causeway in Utah's Great Salt Lake affect water and salt flow?. *PloS one*, 10(12), e0144111.

[17] Barnes, B. D., and Wurtsbaugh, W. A. (2015). The effects of salinity on plankton and benthic communities in the Great Salt Lake, Utah, USA: a microcosm experiment. Canadian Journal of Fisheries and Aquatic Sciences, 72(6), 807-817.

[18] Naftz, D. L., Cederberg, J. R., Krabbenhoft, D. P., Beisner, K. R., Whitehead, J., and Gardberg, J. (2011). Diurnal trends in methylmercury concentration in a wetland adjacent to Great Salt Lake, Utah, USA. *Chemical Geology*, 283(1-2), 78-86.

[19] Null, S.E., W.A. Wurtsbaugh, and C Miller. (2013). Can the causeway in the Great Salt Lake be used to manage salinity? Friends of Great Salt Lake Newsletter 19 (1&2)

[20] Holley, E. R., and Waddell, K. M. (1976). Stratified Flow in Great Salt Lake Culvert. Journal of the Hydraulics Division, 102(7), 969-985.

[21] Spall, R.E. (2009). A Hydrodynamic Model of the Circulation within the South Arm of the Great Salt Lake. International Journal of Modelling and Simulation, 29:2, 181-190.

[22] Spall, R. E. (2011). Basin-Scale Internal Waves Within the South Arm of the Great Salt Lake. International Journal of Modelling and Simulation, 31(1), 25-31.

[23] Dutta, S., Tokyay, T. E., Cataño-Lopera, Y. A., Serafino, S., & Garcia, M. H. (2014). Application of computational fluid dynamic modelling to improve flow and grit transport in Terrence J. O'Brien Water Reclamation Plant, Chicago, Illinois. *Journal of hydraulic research*, 52(6), 759-774.

[24] Crookston, B. M., Anderson, R. M., & Tullis, B. P. (2018). Free-flow discharge estimation method for Piano Key weir geometries. *Journal of Hydro-environment Research*, 19, 160-167.

[25] Levesque, V.A. and Oberg, K.A. (2012). Computing discharge using the index velocity method. U.S. Geological Survey Techniques and Methods 3-A23. U.S. Department of the Interior, U.S. Geologic Survey. 148p. Reston, Virginia.

[26] U.S. Geological Survey (USGS) (2020). National Water Information System Data for the Nation. https://waterdata.usgs.gov/nwis/

[27] HDR (2020) 2019 Annual Data Monitoring Report. https://documents.deq.utah.gov/water-quality/standards-technical-services/gsl-website-docs/uprr-causeway/DWQ-2020-003963.pdf

[28] HDR (2021) 2020 Annual Data Monitoring Report. https://documents.deq.utah.gov/water-quality/standards-technical-services/gsl-website-docs/uprr-causeway/DWQ-2021-002902.pdf

[29] Hirt, C. W., & Nichols, B. D. (1981). Volume of fluid (VOF) method for the dynamics of free boundaries. *Journal of computational physics*, 39(1), 201-225.

[30] Smagorinsky, J. (1963). General circulation experiments with the primitive equations: I. The basic experiment. *Monthly weather review*, 91(3), 99-164.

[31] Germano, M., Piomelli, U., Moin, P., & Cabot, W. H. (1991). A dynamic subgrid-scale eddy viscosity model. *Physics of Fluids A: Fluid Dynamics*, 3(7), 1760-1765.

[32] Pope, S. B. (2001). Turbulent flows, Cambridge

[33] Roache, P. J. (1998). Verification and validation in computational science and engineering. p. 895. Albuquerque, NM: Hermosa.

[34] Naftz, D. L., Millero, F. J., Jones, B. F., & Green, W. R. (2011). An equation of state for hypersaline water in Great Salt Lake, Utah, USA. *Aquatic Geochemistry*, 17(6), 809-820.

6.0 West Crack Breach Rating Curve

One of the main objectives of the project was to develop a 3D CFD model that can model the flow through the breach. In the previous section the 3D CFD model was shown to successfully capture the bi-directional flow regime. Even though the bi-directional flow is what occurs at the breach most of the time, there are two other flow regimes that have been observed in the flow record. First, when almost all the flow through the breach goes from N-S direction, and second when all the flow goes from S-N direction. Both of these flow regimes, where almost all the flow goes from N-S or S-N occurs during wind events. Thus, we also test the CFD model to see if it can capture the N-S and S-N flows. We then used the model to study the sensitivity of the flow through the breach to changes in water surface elevation and density difference.

6.1 Model setup

As described in the previous section, the model has been developed using the volume of fluid based CFD solver Flow3D. The domain for the CFD simulations was made big enough to capture the development and evolution of the N-S and S-N currents, and such that the boundary effects do not adversely affect the dynamics of the flow at the breach.

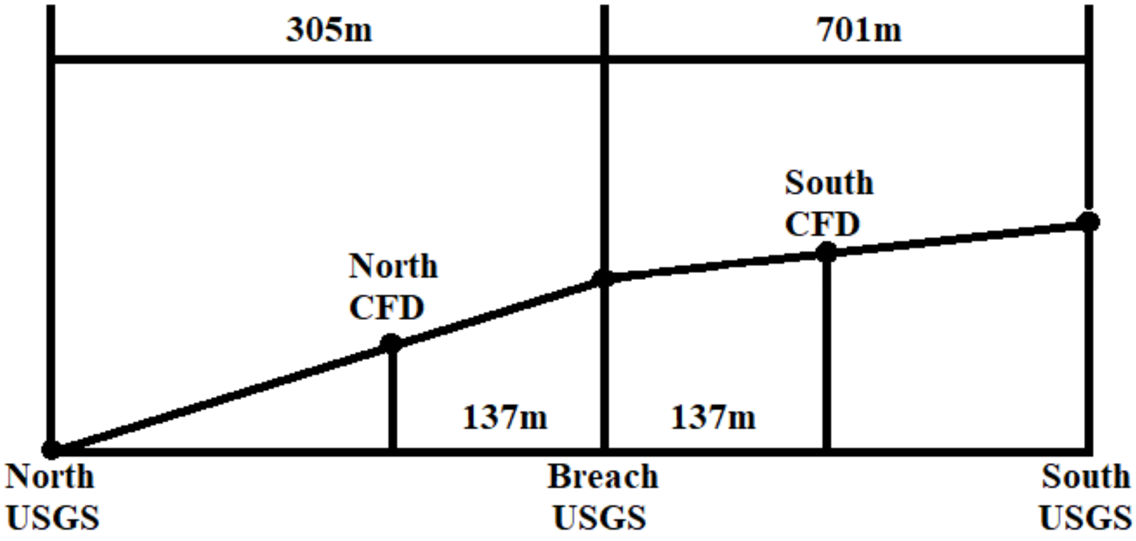

Figure 6.1: The diagram shows the distance of the WSE gauges, on the North and South side, from the breach. WSE at the breach and the USGS gauging stations North and South of the breach is used to approximate the WSE at the CFD domain boundaries.

The computational domain is of width 295 m and length 275 m (in the north-south direction), centered at the breach. All the three regimes of the flow through the breach is modeled assuming that the flow is quasi-steady. Thus constant values of WSE and water density are defined as the initial and boundary conditions. The density of water used for the simulations were based upon continuous specific conductance measurements on the North and South side of the breach (described in Chapter 3), compared against the monthly measurement of TDS taken by USGS and by our team during different field visits to the breach. Additionally, lack of a relationship between specific conductance and salinity for the lake made the estimation of density uncertain. Thus, we had to go through the process described in section 5, where the bidirectional flow simulations were conducted for different possible density difference between the North and the South side of the lake. This process led us to estimate the density difference between the North and South side of the breach to be 83 kg/m^3 during the month of November in 2020. In order to test the performance of the model for the wind-driven N-S and S-N flow events, two wind events from the month of November were chosen. For the bidirectional flows, estimating the WSE at the CFD domain boundary using the method illustrated in figure 6.1 works perfectly. For the wind-driven events we used the same methodology, though the uncertainty of the estimate used for defining the boundary condition is higher in these cases. This could be attributed to the unsteadiness (waves, etc.) observed at the breach during wind events.

6.2 Dynamics of bidirectional flow at the breach

The validated bidirectional flow simulation has been used to analyze the spatial evolution of the flow through the breach (figure 6.3). The vertical and the south to north (S-N) velocities have been plotted for 7 planes that are orthogonal to the y-axis. The relative positions of the planes have been illustrated in figure 6.2. In general the flow can be divided into two parts, the bottom N-S flow and the top S-N flow, but this division is not clear at all the cross-sections. One can observe that the enhanced mixing produced by the piers, as the flow evolved from having sharp stratified layers at cross-section **e** to more diffused layers at cross-sections **d-c**. Enhanced mixing can also be interpreted from substantial velocity in the vertical direction at cross-sections **d-c**.

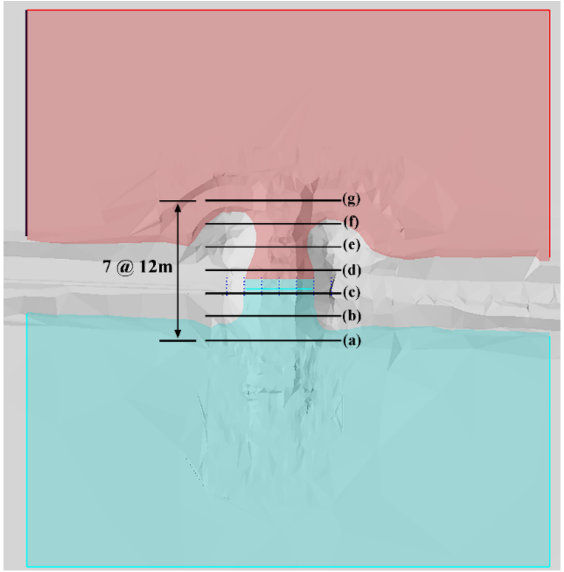

Figure 6.2: Position of the planes for which the vertical and S-N velocities have been plotted. The planes are at a distance 12 m from each other, with plane [d] among the piers

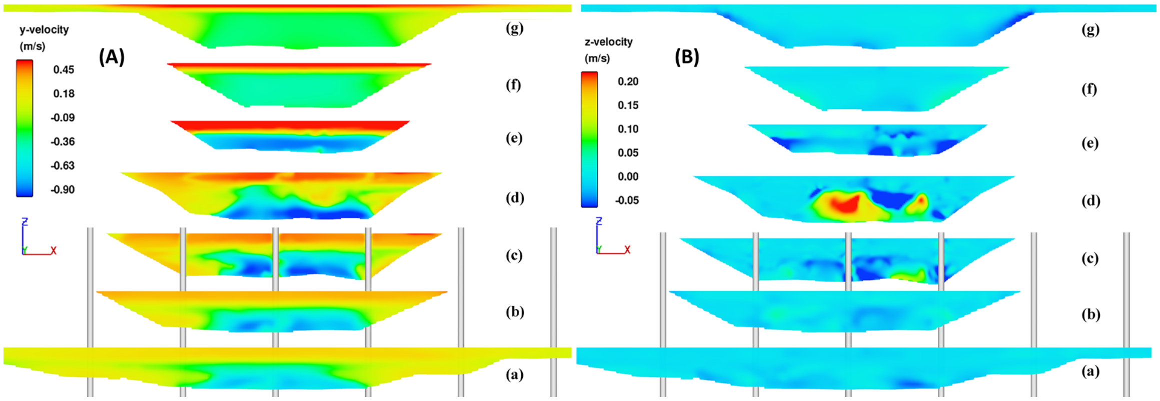

Figure 6.3 Velocity at the breach in the y (A) and z (B) direction has been plotted at seven different planes, orthogonal to the y-axis. The location of the slices has been illustrated in Fig. 6.2 (a) Is the southernmost slice, and every slice after that is at a distance 12 m northward. Slices (a-c) are to the south of the piers, slices (e-g) are to the north of the piers, and slice (d) is within the piers. The S-N flow can be observed to be pushed to the top half of the cross-section, and once it reaches the northern side of the breach, it is confined to a thin high-velocity top layer.

6.3 Dynamics of N-S flow at the breach

The N-S flow usually occurs during sustained north to south wind events. below the south arm water and form a sustained bottom current that continues to move southward, eventually forming the deep brine layer (DBL). N-S winds lead to reduction in WSE difference between the South and North arms of the lake at the breach, allowing the higher density North arm water to push back the S-N flow through the breach. This leads to the flow registered by the USGS ADVM uplooker to show sustained N-S flow through the breach. We used the CFD model developed for the bidirectional case, and changed the WSE at the boundaries to the values observed during the wind-event. We did not explicitly add the wind-induced shear at the water-surface in the CFD model, to test the hypothesis that the local effects of the wind are not necessary to capture the general pattern of the flow through the breach. The steady state velocity results from the CFD model was compared against the velocity measured by USGS at the breach (see figure 6.4).

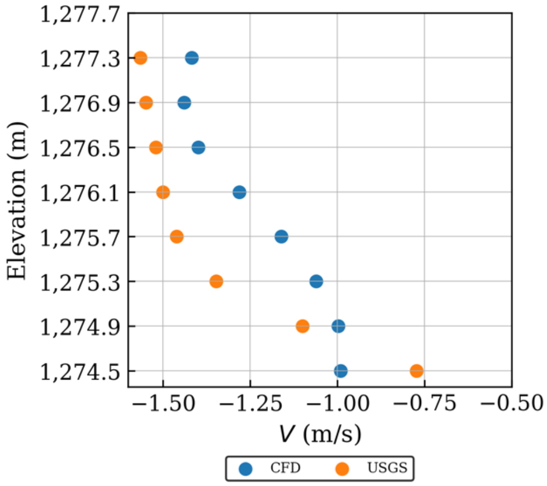

Figure 6.4: Comparison of CFD model velocities with USGS measured velocities for the N-S flow case. The correlation between observed and predicted velocity is $R^2 = 0.69$. The exact values differ, though the trend of the velocity profile is captured by the model.

Comparing the modeled and observed velocity profiles (figure 6.4) show that the model is able to capture the pattern of the flow, though the model for most parts underestimates the velocity. Further investigation is required to improve this. Possible solutions might be related to small uncertainties in the difference in density between N and S side. The model might also be improved by including the wind-induced stresses at water surface. Next, the details of the flow at the breach has been studied using the y and z velocities at different cross-sections (figure 6.6 -6.7).

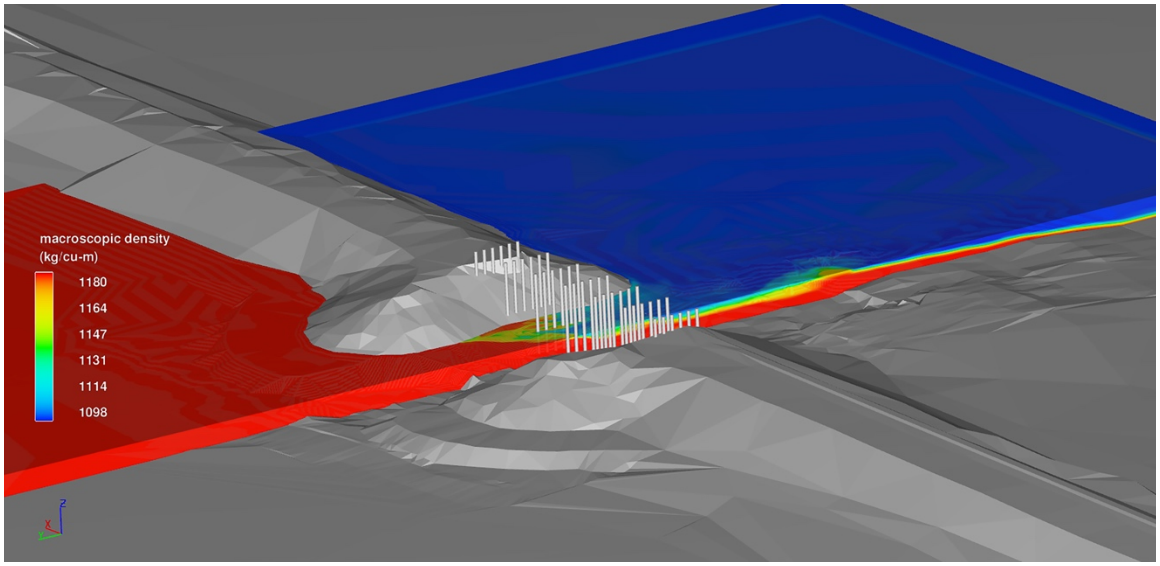

Figure 6.5: Isometric view of the N-S flow. Northern arm water is colored red, and has higher density, and the southern arm water is colored blue and has lower density. The higher-density north water can be observed to be present across the water-column, even after the flow has entered the piers. The piers can be seen to induce mixing, making the density of the top-layer less dense. The North arm water can then be observed to plunge

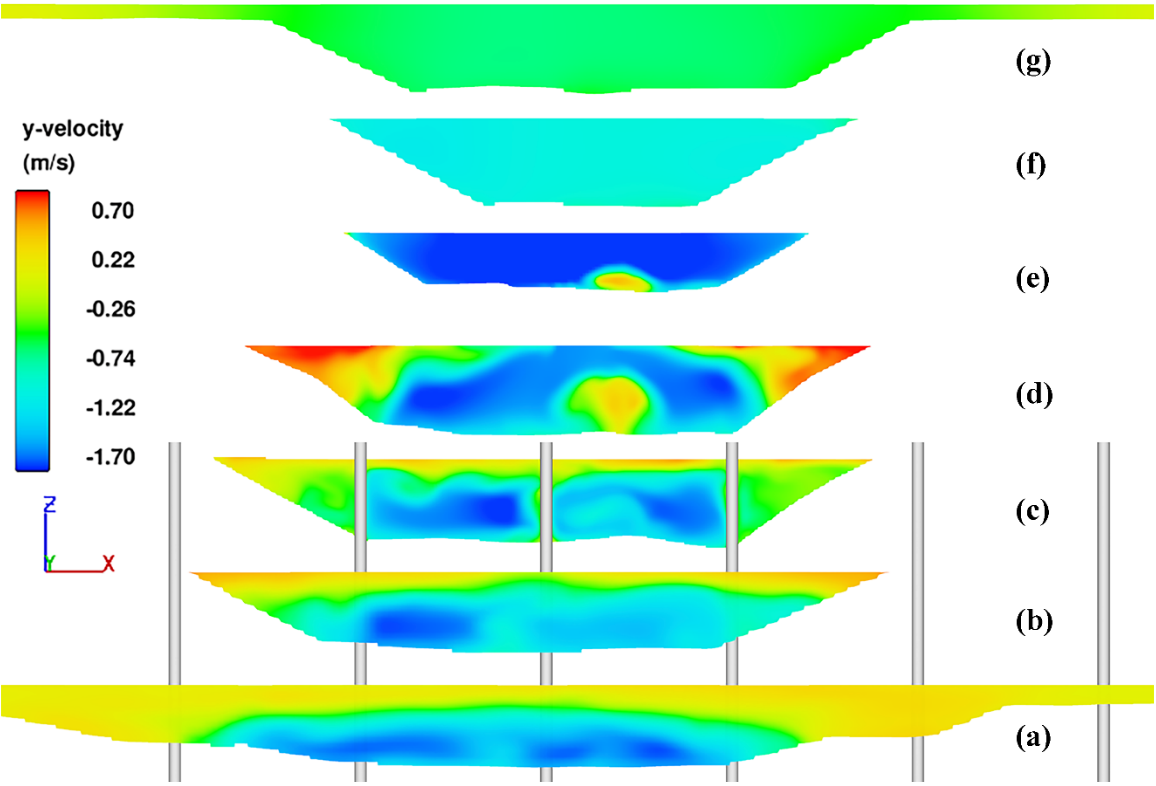

Figure 6.6: y-velocity at different cross-sections for the N-S flow case. As expected, most of the flow at cross-section **(e)** is going southward. Though, there is a small region of the low-velocity near the bottom where the flow is moving north. This small region of northward flow gets bigger at the cross-section within the piers

The flow at cross-section **(e)** (fig. 6.6) as expected is dominated by the N-S flow, though one can observe a small region of northward flow, which increases in size at cross-section **(d)**. One can also observe S-N flow regions at the top edges of the cross-section **(d)**. The reason for this pattern becomes clear, when one observes the corresponding z-velocity panels (figure 6.7). One can clearly observe multiple secondary flow cells at cross-section **(d)**, remnants of which can also be seen at cross-sections **(e)** and **(c)**. Cross-section (d) is present within the array of piers, and secondary flow patterns are formed due to pier induced mixing. The mixing process brings in lighter fluid from the top toward the bottom, which then starts to move up due to buoyancy. This produces secondary flow cells. Though, this pier induced mixing is very quickly suppressed, as the strong secondary flow patterns are not observed in cross-sections 24 m north and south of **(d)**.

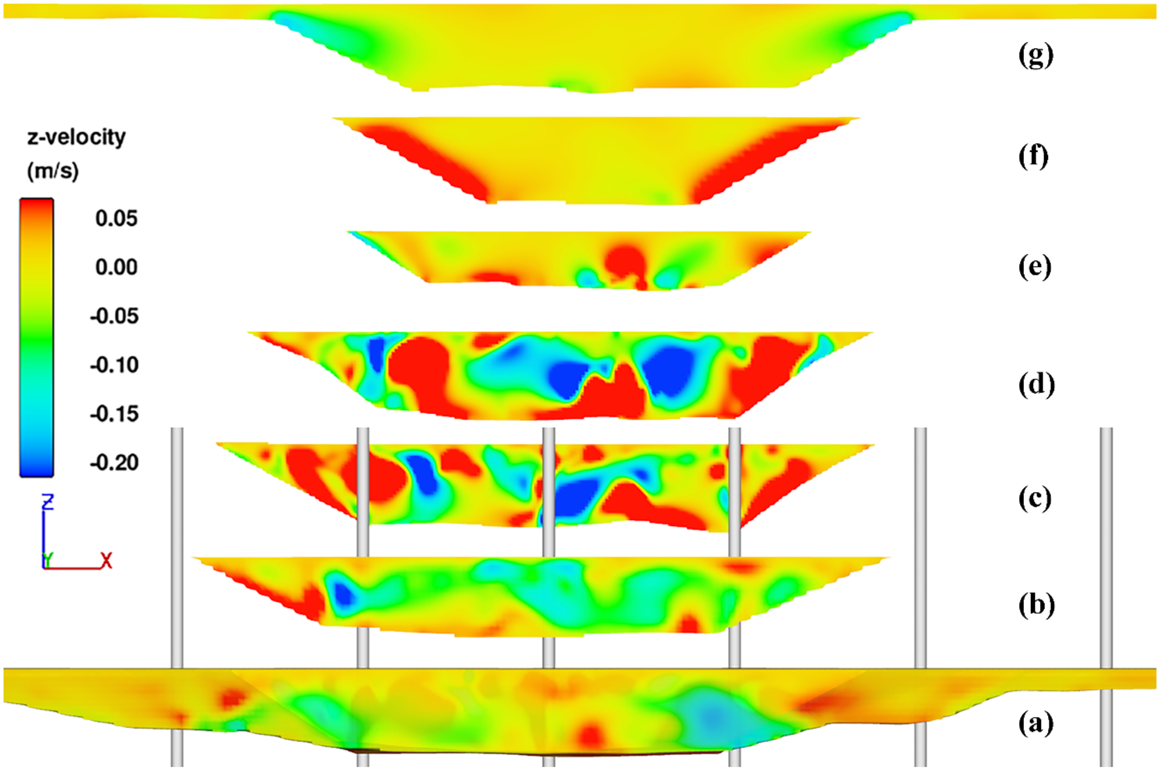

Figure 6.7: Cross-sections for z-velocity in the N-S flow case. Cross-section **(d)** show multiple secondary flow cells, which may be attributed to mixing induced by the presence of the piers.

6.4 Dynamics of S-N flow at the breach

The S-N flow usually occurs during sustained south to north wind events. S-N winds lead to increase in WSE difference between the South and North arms of the lake at the breach, allowing the lower density South arm water to push the N-S flow through the breach. This leads to the flow registered by the USGS ADVM uplooker to show sustained S-N flow through the breach. We used the CFD model developed for the bidirectional case, and changed the WSE at the boundaries to the values observed during the wind-event. We did not explicitly add the wind-induced shear at the water-surface. The steady state velocity results from the CFD model was compared against the velocity measured by USGS at the breach (see figure 6.8).

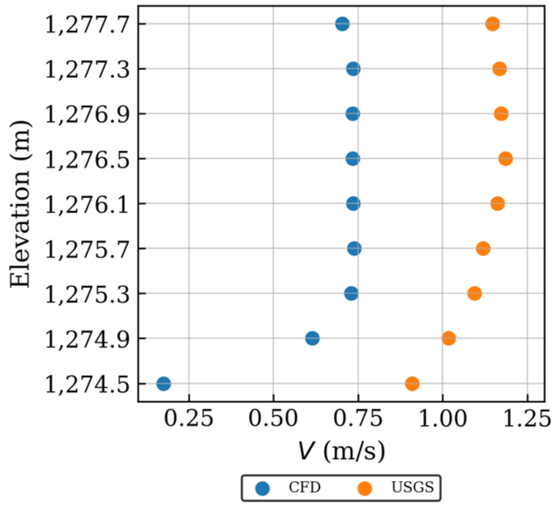

Figure 6.8: Comparison of CFD model velocities with USGS measured velocities for the S-N flow case. The correlation between observed and predicted velocity is $R^2 = 0.82$. The trend of the velocity profile is captured by the model.

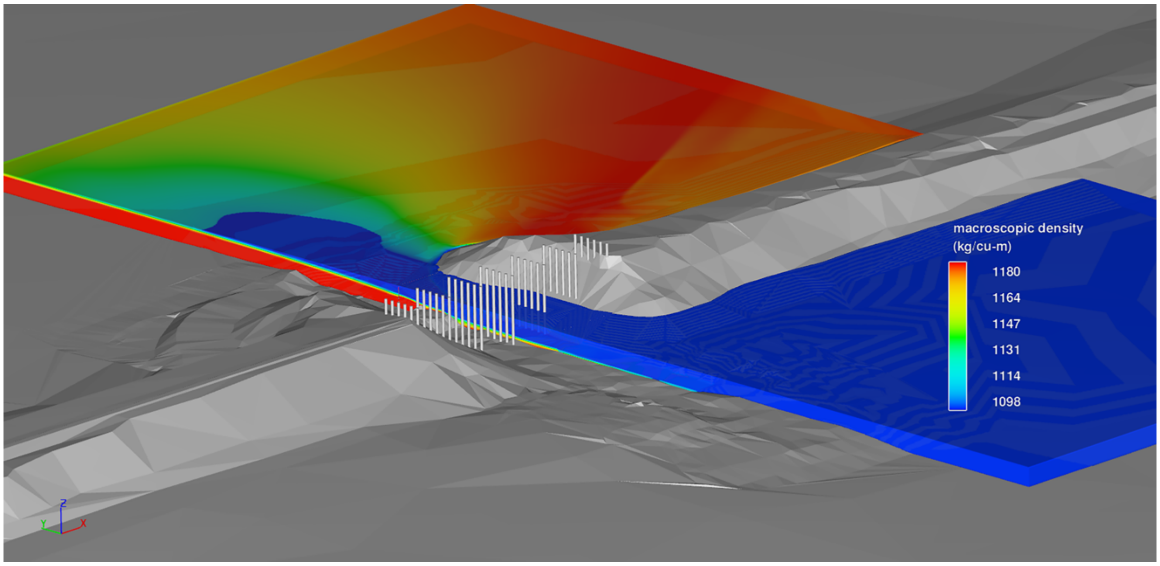

Figure 6.9: Isometric view of the S-N flow. South arm water is colored blue, and has lower density. The lower-density southern water can be seen to be pushing the northern flow, though a low-velocity intrusion of the N-S flow at the bottom can be observed to have leaked into the southern side of the lake. The once the flow from the south side reaches north of the breach, it is pushed up into the upper part of the water column. The extent to which the lower-density surface-plume travels to the northern side is higher than previously observed for the bi-directional flow.

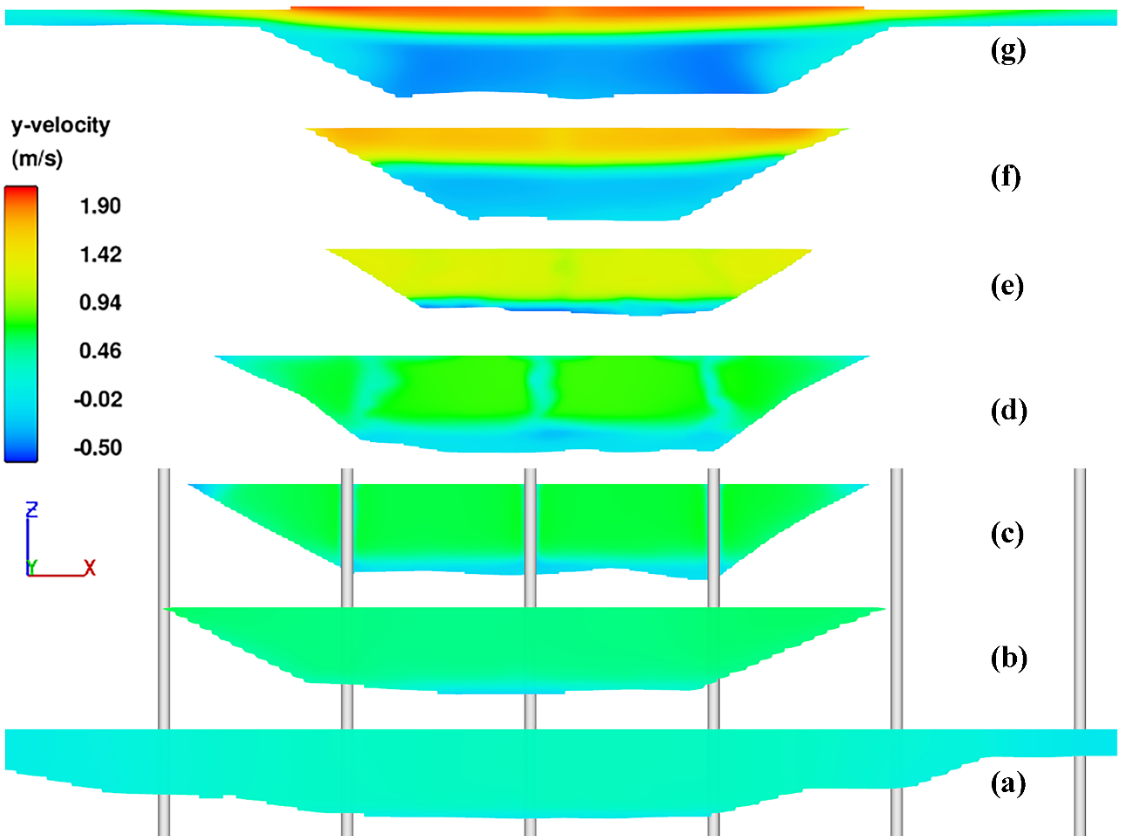

Figure 6.10: y-velocity at different cross-sections for S-N flow. A low-velocity N-S intrusion can be observed near the bottom in cross-section **(e)**. This intrusion gets weaker as one moves southward. The S-N flow can be observed to be pushed to half of the water-column within 12 m of **(e)**, within 1/4th of the water column within 24 m from **(e)**.

The model was able to successfully capture the general pattern of the flow, though the predicted velocity is lower than the observed ($R^2 = 0.82$). Further improvement in the model will be attempted by including the effect of the wind-induced shear at the water surface. The dynamics of the flow is further analyzed by plotting the mixing pattern of the flow (figure 6.9) and the velocities at different cross-sections.

The S-N flow covers major portion of the cross-sections while going through the breach, but one can observe the presence of a low-velocity intrusion confined to the bottom. This flow has also been observed by USGS during S-N flow events, and despite the ADVM uplooker not showing any signs of it, the discharge estimates by USGS account for it. The ADVM uplooker cannot capture it because it does not measure the bottom 1.8 m of the flow. Another interesting observation is that the extent of pier induced mixing in the S-N flow is lower than the N-S flow. This may be attributed to the fact that the velocities of the N-S flow is about 3-4 times the S-N flow, which makes the possibility of pier induced mixing more probable.

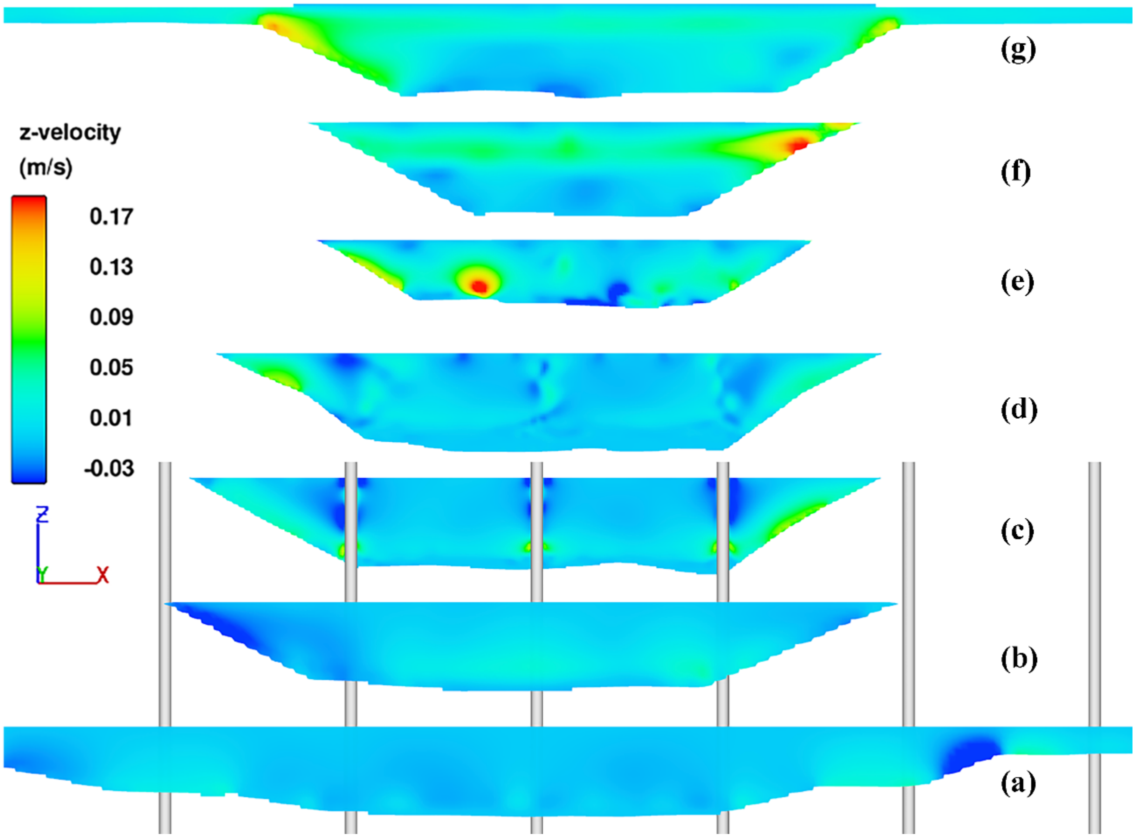

Figure 6.11: z-velocity at different cross-sections for the S-N flow. Effect of the piers on the flow can be observed **(c-d)**. Downward vertical velocity can be observed within the N-S core of the flow in cross-sections **(f-g)**, and this can be attributed to the N-S flow getting pushed under the dominant S-N flow, while it approaches breach.

6.5 Potential effect of changing lake level and North-South density difference on the bidirectional flow discharge

In last few sections we have displayed the veracity of the three-dimensional CFD model to successfully capture the flow through the breach, especially for the bidirectional flow case. Development of the model took multiple 2D and 3D simulations, to figure out the optimal computational mesh size, turbulence closures, domain size, etc. The whole process required us to conduct almost 50 simulations (see Appendix E). The validated CFD model was used to simulate potential scenarios in which the lake level increases/decreases by 0.3 – 0.9 meters. The range of lake-level change is based upon observed lake level within the last 20 years. The decrease in lake-level cases if for simulating scenarios in which the GSL level drops further due to persistent drought and increase in water use. The simulations were setup by taking the validated bidirectional case (chapter 5) as the base case, and the WSE was increased or decreased by the same amount, for both sides of the breach. This is based on the assumption that increase or decrease in general lake-level will change both sides of the lake equally. It was assumed that change in lake-level will not affect the density of the north and south arm. The N-S and S-N flow discharge are presented in figure 6.12. Effect of change in density difference between the North and South arm of the lake was also modeled, and the results have been plotted in figure 6.13.

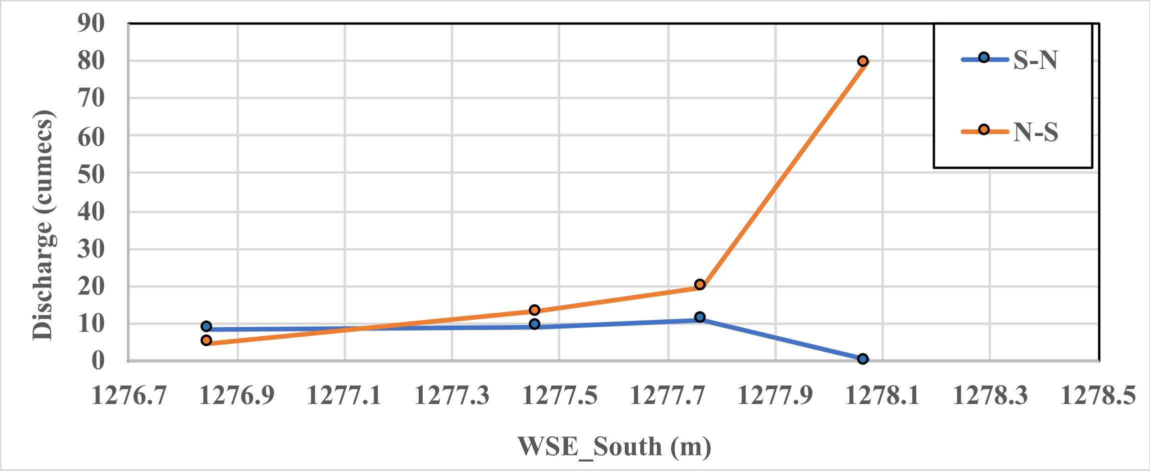

Figure 6.12: At the current scenario, the N-S and S-N flow are at about 10 and 20 cubic meter per second (cumecs). Decrease in lake-level lead to major reduction in N-S flow, with 0.91 meter decrease resulting in N-S flow reducing to about 5 cumecs. The corresponding change to S-N flow is small. On the other hand, increase in lake level by 0.3 m results in complete stop in the S-N flow and N-S flow increasing to ~ 80 cumecs.

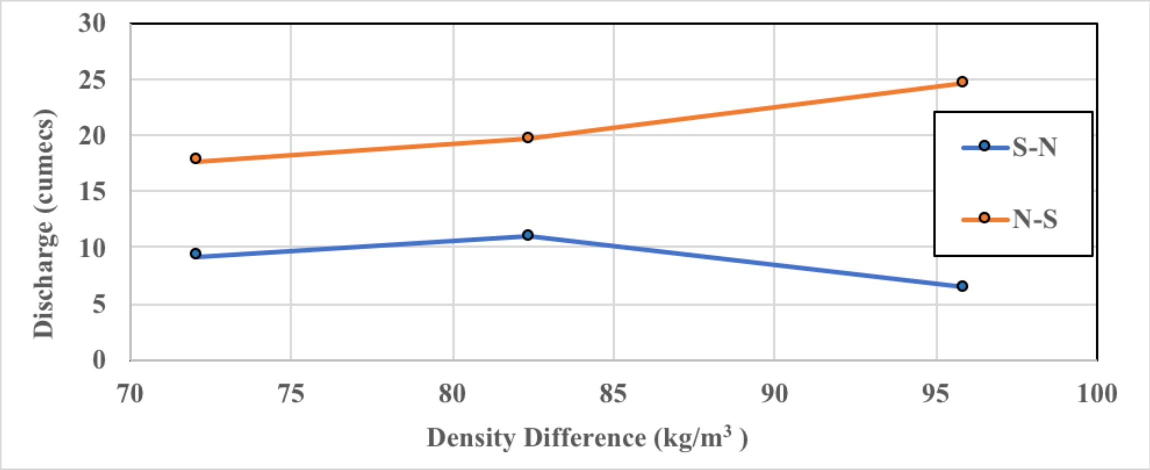

Figure 6.13: At the current scenario, the N-S and S-N flow are at about 10 and 20 cubic meter per second (cumecs). At the same lake level, decrease in density difference between the North and South arms of the lake will result in decrease in N-S flow, but no appreciable change in S-N flow, whereas increase in density difference between the two sides will result in substantial increase in N-S flow, and substantial decrease in S-N flow.

7.0 Deep Neural Network Based Flow Model

Artificial Neural Networks (ANN) and Deep Neural Networks (DNN) are artificial means of creating a system that mimics the natural learning process (Bruton, 2019). Artificial Neural Networks are comprised of layers which are made up of a collection of nodes. The nodes are the basic computing unit of the system. Nodes sum the weighted average of input information to then pass to the next layer (Ghosh, 2014). Networks are comprised of an input layer, hidden layers, and an output layer. The network is used to map n-dimensional input layer to an m-dimensional desired output layer (Ghosh, 2014, Sit 2021). The input layers of a network are the first layer built into the network. The input layer is the n-dimensional information given to the network. This information is then passed to the hidden layers of the system comprised of various nodes, weights, and biases. This process is continued until the information is fed to the output layer. The output layer is the final layer of the network, and provides the prediction form the model (Sit, 2021).

The ANN then compares the produced output to a validation training set. The Weights are adjusted in the layers according to the learning rate set to the system (The default learning rate of TensorFlow is set to 0.001) (Tensorflow.org). The information is then back propagated through the layers and the weights are adjusted to improve the accuracy of the model (Saharei, 2021). This process is repeated for each training set (Saharei, 2021). Data pool are the total pool of information that is comprised to feed to the model. The Data pool is subdivided into three different groups: Training Data, Testing Data, and Validation Data. Training data is subdivided into training batches. Training Batches, or batches, are a group of training data that the system is given to find patterns. The network sets or updates the node weights when it has run through all the data in the training batch (Gupta, 2013). A collection of training batches run for all the training data is known as an epoch. When completing any epoch, the system tests the information against the validation data to ensure that the information is valid to data that it has not seen. If the network is overly complicated for the problem it is trying to resolve it can overfit the data. Overfitting is when the network attempts to hard memorize the information that it is given, and then reproduce these same numbers without finding relationships between variables (Ying).

During the training of any ANN or DNN the goal of training is to maintain the training loss below the validation loss for the model. Each of these loss parameters are calculated after each epoch is run. The information is stored in the network training data. In addition, the training loss being lower than the validation loss, steady decrease in both parameters is desired. Jumpy or sporadic behavior in modeling can be attributed to an overly complex network arrangement. The network may be attempting to model the noise that is found in the data that was collected (Saharei, 2021). Another possibility is that the batches are too large or small that the network is unable to adequately find connections between the data entries that are included in the training data. All these parameters must be included in the final result to formulate the most accurate model possible.

7.1 Data pre-processing

Just as important as the way that the model is trained, is the type of information that it is given (Altun, 2017). Data Preprocessing ensures that the information that is given to the system has all the needed parts, and will accurately represent the system that is being modeled. Data preprocessing is a major step in ensuring that the model is able to produce accurate results. The cleaner the data is before being given to the model, the less noise that can be modeled by the network during the training procedure. The GSL model allowed for extensive data preprocessing. Data was collected using United States Geological Survey's (USGS) instrumentation sites at the West Crack breach. Multiple sites were used, including sites 10010025-27 (www.waterdata.usgs) near the breach, and other stations where specific conductance data was collected on a monthly to bi-monthly basis (USGS gauges shown in Figure 7.1).

Data was available at these sites from varying time periods. For the majority of sites information was available from the year 2017 to 2021. Data was collected and compiled into one master data set. The parameter fields that was compiled into the master data set were the WSE north of the breach, WSE south of the breach, WSE at the breach, wind speed at the breach, wind direction at the breach, individual cell velocities measured by the USGS ADVM, USGS estimated N-S and S-N discharge. All information was compiled into one Microsoft excel file and used as the data pool for network development. After the compilation of the information, it was noted that holes were present in the information.

Missing information ranged from a single point to strings of multiple data point. These were due to different instrument maintenance related issues. The GSL during normal bi-directional flow cases is fairly steady, that is change in WSE, discharge etc., doesn't happens slowly. So the hypotheses was that interpolation between windows of 15 to 30 minutes were reasonable, expect for when the flow transitions between the different regimes. To account for small window errors python NumPy and pandas were used to interpolate between missing data points. Time windows that were larger than this were not interpolated due the lack of confidence in the interpolated values.

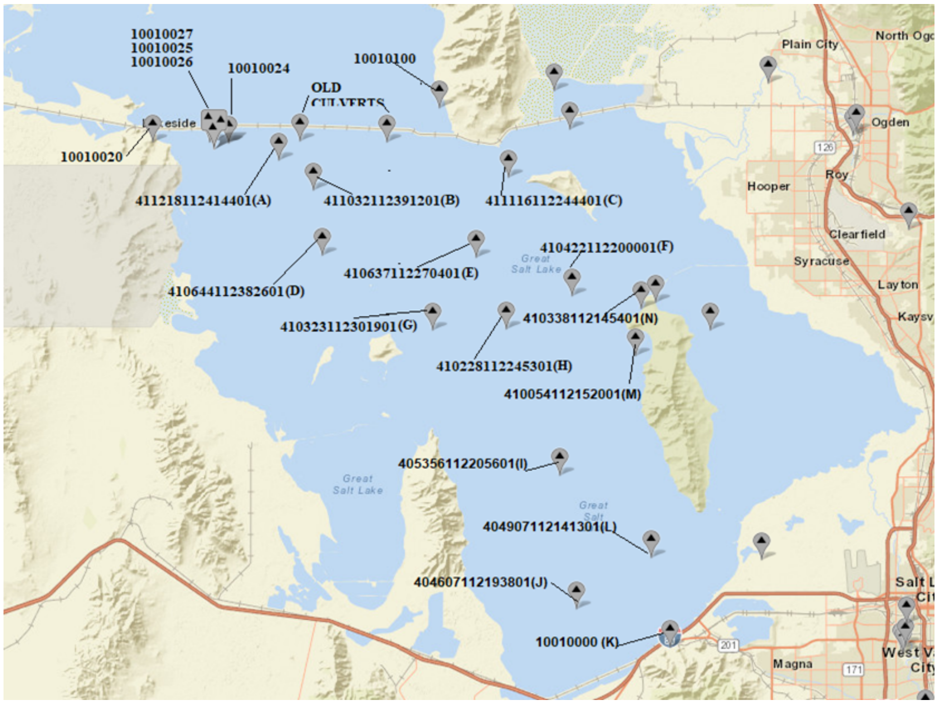

Figure 7.1: USGS Data collection sites at the GSL (maps.waterdata.usgs)

Interpolation provided the missing information and attributed to a more complete data pool to train the model. Data entries that were still missing information were removed from the data pool using the game python package pandas. Missing information from any data entry could be any of the five information pieces formally stated. During data processing it was noted that the information provided for discharge had faulty data contained in it. The discharge information had entries that were not consistent with the average discharge measured during the window period. A rolling average was used to compute the change in average discharge over an hour window. Transitions between time periods that were not in the standard 15-minute intervals were excluded from the rolling average, because they were not sequential entries. Percent changes over the 15 percent were analyzed to ensure they were reasonable for the system. Large percent changes were expected to occur during flow regime transitions.

The next set of data used to develop the model was density of the north and south arm. Due to uncertainty of the relationship between specific conductance and salinity, we used the specific conductance data in the model directly. The master data set mentioned in the previous paragraph has data at a 15-minute interval. While specific conductance data that was collected by USGS were averaged measurements taken once per month. The resulting issue was a lack of functional data for specific conductance during data collection of the other variables. Therefore, additional insight was needed. Thus, the USU team installed sondes in both the north arm and south arm of the lake. These instruments measured the specific conductance of the two arms at a 15-minute interval. The collected data was not during the same time period as the discharge data used in the network, but allowed for increased insight to how specific conductance data could be added to the data pool. Comparing the collected results from the sondes to the monthly measurements from USGS showed that they were similar measurement (see Figure 7.2).

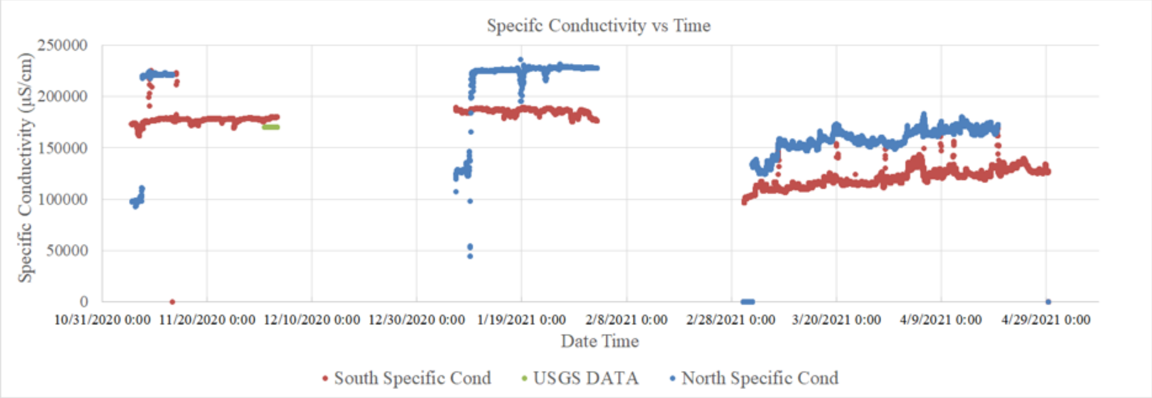

Figure 7.2: Time series of UWRL specific conductance of GSL North and South Arm compared to USGS measurements

The only value that was available for comparison was during November 2020. The USU monthly average of recorded data was within 5.29 percent of the USGS monthly measurement, as shown in Table 1. The time series of specific conductance recorded by USU at the west crack breach is shown in Fig 7.2.

Table 7.1: Comparison between USGS data and USU collected monthly average (µs/cm)

	South Arm Specific Conductance		
Month	USGS	USU	Percent Difference
Dec-2020	170000	179000	5.29

The resulting comparison shown in Table 1 and Fig. 3 showed that the recorded specific conductance data from USGS could be used as a monthly average data. The specific conductance information was then added to the filtered data pool. With the gaps in USGS samples a more comprehensive data log was needed for specific conductance measurements. Additional information was included using the sampling performed by HDR for the duration of 2017 to 2019. These measurements were recorded in the annual report data from HDR (HDR Reports 2018-2020). There was no time frame from HDR data available for comparison between the USU data. Two months were selected from each sampling year from all sampled months. The comparison between HDR data and USGS sampling is shown in Table 2.

Table 7.2: Comparison between USGS data and HDR annual report specific conductance measurements with percent error. (µs/cm)

	South Arm			North Arm		
Month	USGS	HDR	% Error	USGS	HDR	% Error
Aug-2017	145000	149600	3.17	218000	225000	3.21
Nov-2017	152000	149700	1.51	215000	219000	1.86
May-2018	138000	145300	5.29	215000	223000	3.72
July-2018	152000	149600	1.58	223000	223000	0.00
Feb-2019	166000	167100	0.66	222000	224000	0.90
Jun-2019	127000	137400	8.19	210000	225000	7.14

The comparison between USGS and HDR data showed that they were similar measurements with a max error of 8.19 % from the months that were compared. From this analysis it was decided that the use of HDR data would produce the most comprehensive list of specific conductance data for the model with reasonable error. From the UWRL time series information it was concluded that it was appropriate to use a monthly average for specific conductance. Therefore, all specific conductance measurements were set to the HDR sample measurement for the duration of the month in the data pool. The resulting preprocessing refined the network's data pool from 111,115 data entries to a final number of 27,204 data entries. The process allowed for a cleaner data set from the original information that was collect. In addition, the preprocessing allowed for greater accuracy in the model with reduced noise. To mitigate the chance of the network using overcorrecting for large variables and training to overcorrected values, the data pool for the network was normalized between 0 and 1. This allows the system to see all the same values but with much lower scalar values. The information input to the system is still the same, but the management of the network through training is easier [8]. The Resulting network output can be remapped to original values using the reverse process of normalization.

7.2 Testing and training of the networks

The data pool was separated into three distinct groups, training data, testing data, and validation data. The data was randomized and then split into different percentages. The same randomization was used in all tests. Randomization was only changed to ensure that model training results were not due to a specific split in the data pool. Data was split using an 80, 10, 10 split. Eighty percent was set for training, ten percent was set for both testing and validation data. The data pool that was used for the study contained 27204 data entries. Training data had 21763 entries, testing and validation had 2721 and 2720 data entries respectively. The ANN that was used in this study was implemented using Python, and packages contained in it. Python and all packages used in the study were used in Pycharm. The packages used in this study were Keras (Keras), Pandas, Numpy, Matplotlib, and Sklearn. Keras was used to develop the network, the other packages were used for data processing and visualization of results. Results of network testing were visualized using

Pycharm’s output as well as Tensor board to visualize the process of the network during training. A full graph of all networks trained is shown in Fig. 3.

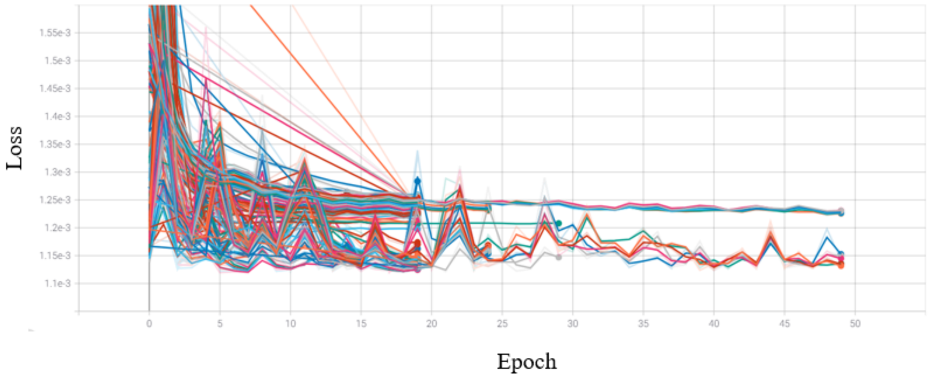

Figure 7.3: Graph of all training data tested and visualized using Tensor board

As shown in Fig. 7.3 the general trend for all tested network set ups was a decrease in both training and validation data. The Top set of lines is the collection of training losses, where the lower lines are the validation losses. It was noted which networks showed promise with final training and validation losses, and had general decreasing trends in the loss during training. For a network to perform well, the network was to maintain validation loss below training loss. In addition, the general trend of training needed to decrease as epochs were increased. Networks that produced smooth decreasing trends were testing using full data sets for longer epochs to determine R^2 values. These tests were performed in PyCharm and all visualization was done using PyCharm outputs. Through testing it was shown that not all networks that showed promise in Tensor board's visualization performed well in network training. The networks that showed the most promise were trained for various epoch lengths ranging from 10 to 400. Networks were compared through training information to establish which networks allowed for long training without overfitting to the information that was provided.

Network development was continued through PyCharm's output using trends that were noticed through Tensor board development. It was noted that a decreasing number of nodes through layers increased the accuracy of the model for discharge. Similar to the tapering method tested in Tensor board. It was decided that a tapering method would create the best working model for discharge. Batch size was another variable needed create a functional network. If a batch size is too large there is little learning in the model. If the batch size is too small it is prone to training to extreme data points, or training to data points that are out of the normal conditions. Batch sizes were conducted using Tensor board. In Fig. 3 it is noticed the jumps in validation loss at different epoch times. If the network is not able to see enough data points in a batch it cannot make connections between variables correctly. Training in batch size is shown in Fig. 7.4. All batch sizes from networks that were tested showed promise. As shown in Figure 7.4, all networks maintained a decreasing trend, with validation loss maintained under the training loss. The batch size that ended with the lowest validation loss at 50 epoch training length was the network using a batch size of 12. Therefore, the batch size for the final network was set to be 12 data entries.

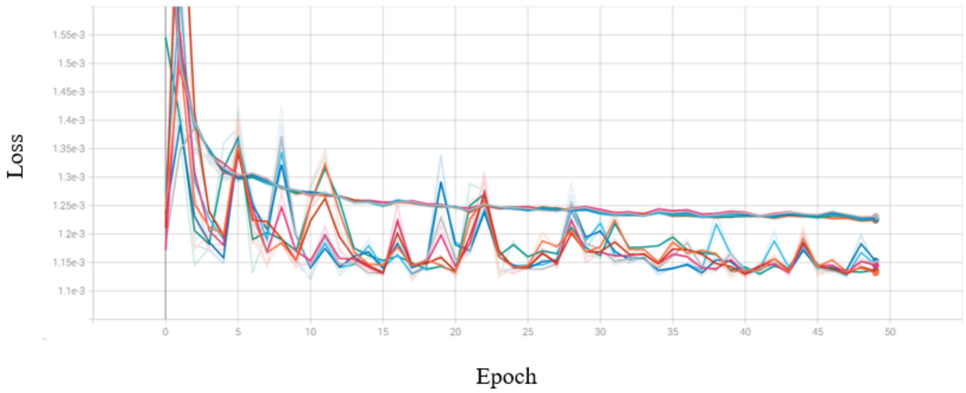

Figure 7.4: Training and Validation loss during batch size testing

7.3 Setup of the final deep neural network

The structure of the final ANN was decided through various tests that were preformed using a variety of network set ups. Decisions of the best performing network were driven by analyzing the loss function of each network after testing was performed. Patterns in the training development of the model were closely inspected for overfitting and for steady decreasing patterns in during training. The loss function that was selected for the network was the mean squared error. This function was selected for the variety of problems it has been used on, and to best model a regression fit. No other loss function was tested with. The variables that were adjusted for each model were the number of layers, nodes in each layer, activation function, batch size of training data, the number of epochs the network was trained for, and the optimizer that was used. The networks that showed decreasing behavior for both validation and test data were further tested to develop an optimized network.

The number of layers that were tested ranged from 2-8 layers including the input and output layers. The activation functions used were, rectified linear unit (Relu), LeakyRelu, and SoftMax. Nodes used in the network training ranged from 8-64. Typical network set up was developed using tapering that divided the number of nodes in each by two in each sequential layer. Batch sizes range from 8 – 20, and the epoch lengths ranged from 10 – 400. Longer epoch lengths were tested with networks that showed promise in not overfitting during long training. The best ANN that was found consisted of 6 layers, batch size of 12, Adam optimizer, and all dense layers using the Relu Activation function. An input layer of 7 nodes, the input was passed to a layer of 64 nodes. The third dense layer had 48 nodes. The fourth layer was made up of 32 nodes. The fourth dense layer was made of 16 nodes. The output layer was a single node without any activation function. The output of the network was the discharge given the input information. Structure of the network is shown in Fig. 7.5.

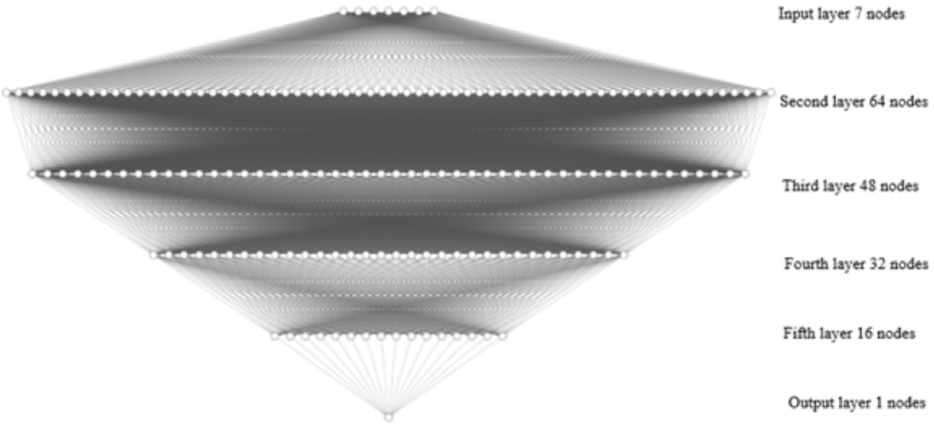

Figure 7.5: Structure of best performing artificial neural network (ANN) found during development, created using online resource (http://alexlenail.me/NN-SVG/index.html)

7.4 Results

As formerly stated, the best network consisted of 6 layers in total as shown in Fig. 7.5. Evaluation of the network performance was done by testing the test data against the prediction values from the model. Ideally these values would follow a linear trend with values following a line similar to y = x. The final network set up was tested with and without specific conductance as this is a measurement that is not available in the same way as the other inputs to the network.

The network without specific conductance data was trained for 50 epochs and the R^2 value for south to north flow was 0.918, with a north to south R^2 value of 0.909. The plots for testing data are shown in Fig. 7.6. When the network without specific conductance was trained for 150 epochs the R^2 values for south to north, and north to south were 0.920 and 0.902 respectively. The plots for these networks are shown in Fig. 7.7.

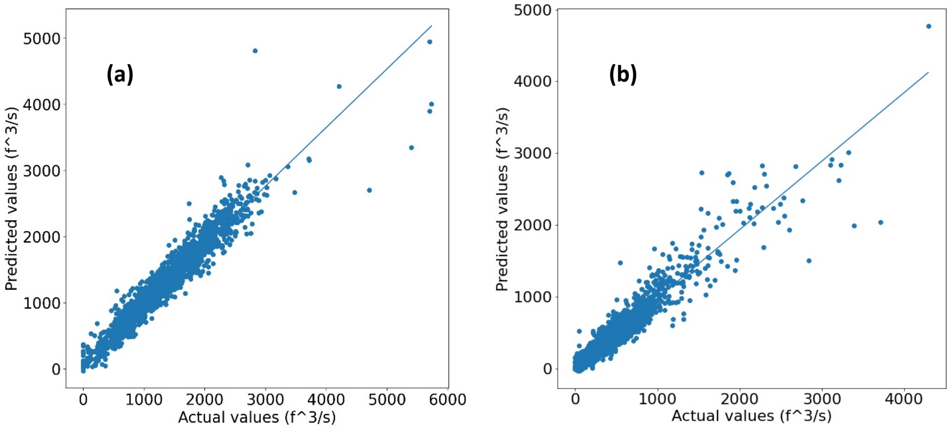

Figure 7.6: 50 epoch training length model without specific conductance, R^2 (0.918) plot for South to North flow (a), and R2 (0.909) plot for North to South flow (b)

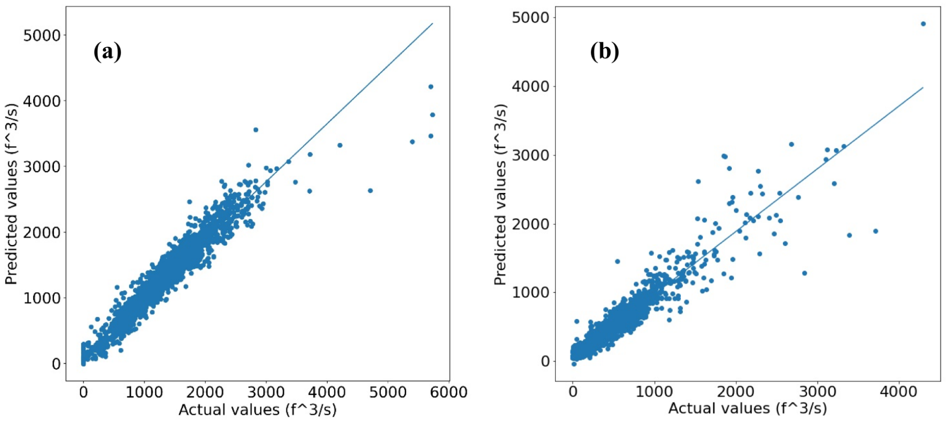

Figure 7.7: 150 epoch training length model without specific conductance, R^2 (0.920) plot for South to North flow (a), and R2 (0.903) plot for North to South flow (b)

The network including specific conductance data was trained for 50 epochs the R^2 for south to north flow was 0.9404, with the north to south R^2 value of 0.9026. The resulting plots from the testing data is shown in Fig 7.8. Additionally, the results from the same network trained for 150 epochs is shown in Fig. 7.9. The R^2 values for south to north flow, and north to south flow were 0.9443 and 0.8983 respectively.

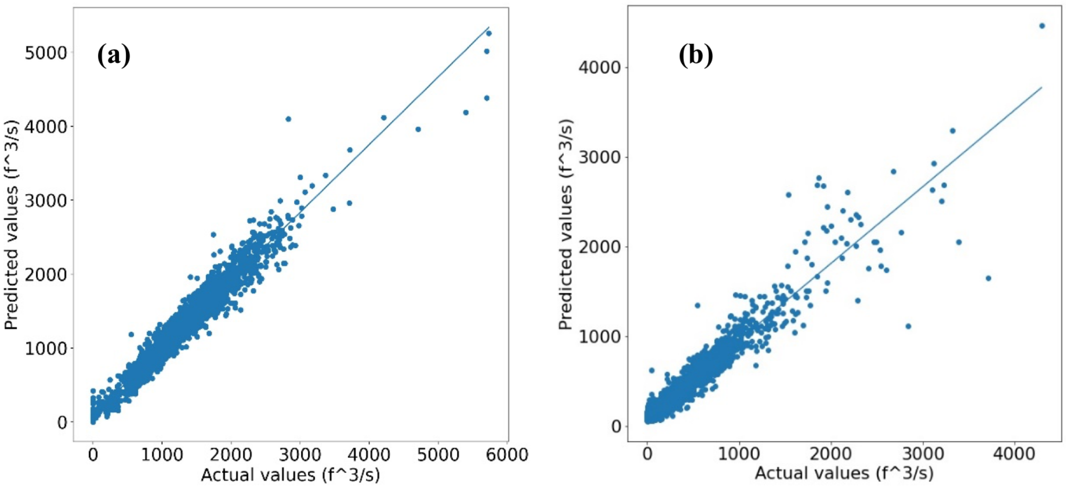

Figure 7.8: 150 epoch training length model including specific conductance, R^2 (0.94) plot for South to North flow (a), and R^2 (0.902) plot for North to South flow (b)

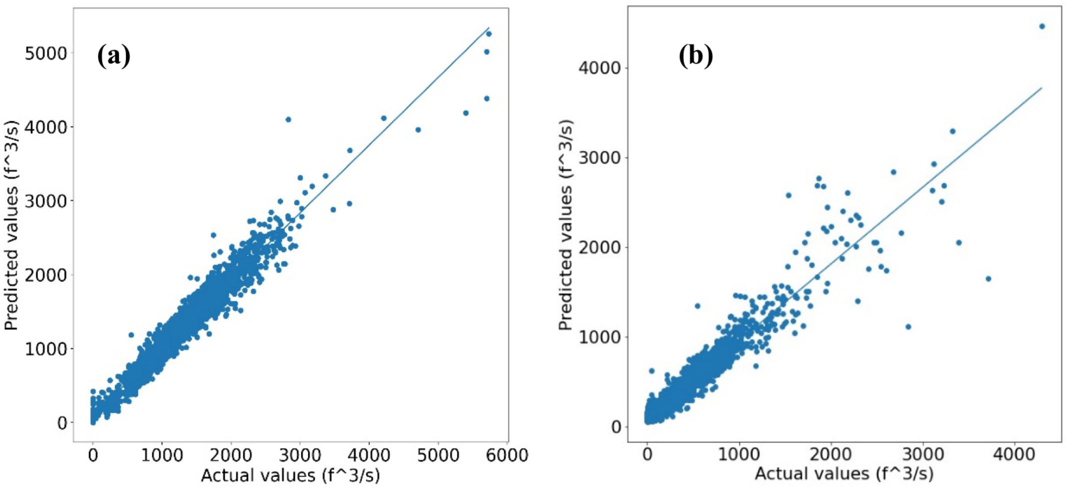

Figure 7.9: 150 epoch training length model including specific conductance, R^2 (0.944) plot for South to North flow (a), and R^2 (0.898) plot for North to South flow (b)

It was shown by both the R^2 values and the plots that specific conductance was able to improve the model's accuracy in predicting total discharge. The network trained for 50 epochs showed an improvement of 0.0227 in R^2 value by adding specific conductance. The North to south discharge for 50 epochs showed higher R^2 values without specific conductance data; but adding specific conductance allowed network training to be smoother throughout training. Training the network for 150 epochs allowed for additional insight. It was shown that adding specific conductance improved R^2 value for south to north flow by 0.0243 and north to south flow showed a similar trend of a more unsteady training without specific conductance data. Overall, it can be seen that implementing the specific conductance data allowed the model to increase in accuracy, and improved training of the model. If there were specific conductance data at the same time interval as the rest of the measurements it is expected that the accuracy of the model would continue to increase.

It is visible from the R^2 plots that for the majority of cases that the network was able to effectively predict the associated discharge for both north to south and south to north flow. The network performed well for the general cases of flow. It is noted that near the lower discharges and the higher discharges is where the network has the most difficulty. This is congregant with the thought process that the system is more complicated during single direction flow cases. The single direction flow requires one of the arms to have enough energy and the right conditions to overpower the processes of the other. Mainly hydrostatic pressure and density difference. These conditions can be difficult for the system to process without enough information. The Information that was provided to the system allowed for appropriate use during the general bi-directional cause present at the west crack breach. While the network showed that it was not able to accurately predict single flow resigns.

7.4 Discussion

Through this study it was shown that ANN was able to adequately predict the total discharge from one arm to the other at the west crack breach. It was shown that for general cases of bi-directional flow the ANN was able to predict the discharge with high fidelity. Our study also shows that the ANN approximation deteriorates as the model approaches extreme flow events, both in high and low discharge measurement. It was also shown that with the limitations of the ANN, the model was still able to perform better than a standard regression model. During development of the ANN the limitation in the amount of single flow event information led to the limitation of the model. If there was a larger data pool available for extreme flow event cases it is anticipated that the ANN would be able to have higher R2 values for all flow cases. In addition, the limited window when all need data was collected attributed to the limitation of the ANN model. To increase the amount of data available for use in ANN development would require continual measurements for an extended period of time. Additional research is needed to understand how best to collect all the data that is needed for better ANN development. There is potential that with more extreme flow event information a more well-rounded model can be created for all flow cases. This would require more information to be available at a variety of lake conditions. If the information was available it

8.0 Final Summary of Work

The density-driven current through the West Crack of the Great Salt Lake Causeway exhibit three conditions: flows north to south, bidirectional flows, and flows south to north. These three cases were simulated with a computational fluid dynamics model and an Artificial Neural Network Model to support management efforts that include environmental and economic concerns. Modeling was based upon a new field campaign and datasets provided by USGS.

Results from this study indicate that this CFD model can accurately simulate all three flow cases. Also, results from the ANN model show excellent agreement and a rating curve could be used for management efforts. For the bidirectional case, which is most common, the vertical velocity profile in the breach had good agreement with the unpublished USGS velocity profile data with an $R^2=0.9578$ generally within 20 to 50%. The CFD model is sensitive to density differences between the north and south waters, along with breach geometry and water surface elevations, which is also the case for the actual lake flows through the WC Breach. The results also indicate that flow patterns and mass exchange through the breach can be influenced by the submerged dike and that a hydraulic structure rating curve can be successfully developed for hydrologic modeling of the Great Salt Lake.

These results suggest that additional research is needed to study flows through the breach for lower lake levels, as perhaps lower lake levels, such as during a drought, may result in undesirable exchange levels. Finally, the rating curve developed in this study merits additional research to explore other breach geometries and climate effects to increase its robustness.

9.0 References

AghaKouchak, A., Norouzi, H., Madani, K., Mirchi, A., Azarderakhsh, M., Nazemi, A., and Hasanzadeh, E. (2015). Aral Sea syndrome desiccates Lake Urmia: call for action. *Journal of Great Lakes Research*, 41(1), 307-311.

Altun, Y., Mielikäinen, K., Stefanoski, J., Machine Learning and Knowledge Discover in Databases, September, 2017

Baskin, R.L., and Turner, J., 2006, Bathymetric map of the north part of Great Salt Lake, Utah: U.S. Geological Survey Scientific Investigations Map 2006–2954.

Barnes, B. D., and Wurtsbaugh, W. A. (2015). The effects of salinity on plankton and benthic communities in the Great Salt Lake, Utah, USA: a microcosm experiment. Canadian Journal of Fisheries and Aquatic Sciences, 72(6), 807-817.

Baxter, B. K. (2018). Great Salt Lake microbiology: a historical perspective. International Microbiology, 21(3), 79-95.

Bioeconomics, Inc., (2012). Economic significance of the Great Salt Lake to the State of Utah. Prepared for State of Utah Great Salt Lake Advisory Council. http://www.gslcouncil.utah.gov/docs/GSL_FINAL_REPORT-1-26-12.PDF

Brunton, S., Noack, B., Koumoutsakos, P. Annual Review of Fluid Mechanics Machine Learning for Fluid Mechanics, Annual Reviews August 2019

Case, H. L. I. et al., (2013). Salton Sea Ecosystem Monitoring and Assessment Plan Open- File Report 2013–1133, United States Geological Survey

Crookston, B. M., Anderson, R. M., & Tullis, B. P. (2018). Free-flow discharge estimation method for Piano Key weir geometries. *Journal of Hydro-environment Research*, 19, 160-167.

Dutta, S., Tokyay, T. E., Cataño-Lopera, Y. A., Serafino, S., & Garcia, M. H. (2014). Application of computational fluid dynamic modelling to improve flow and grit transport in Terrence J. O'Brien Water Reclamation Plant, Chicago, Illinois. *Journal of hydraulic research*, 52(6), 759-774.

Germano, M., Piomelli, U., Moin, P., & Cabot, W. H. (1991). A dynamic subgrid-scale eddy viscosity model. *Physics of Fluids A: Fluid Dynamics*, 3(7), 1760-1765.

Ghosh, M.,Dutta, S., Sen, D. Sediment Flushout from Pond and River Diversion Barrages by Gate Operation, Water Resour Manage, September 2014

Gupta, N. Artificial Neural Networks, Network and Complex Systems, Vol. 3, No. 1, 2013

Gross, M., (2017). The world's vanishing lakes. *Curr. Biol. 27*, 43–46

HDR (2020) 2019 Annual Data Monitoring Report. https://documents.deq.utah.gov/water-quality/standards-technical-services/gsl-website-docs/uprr-causeway/DWQ-2020-003963.pdf

HDR (2021) 2020 Annual Data Monitoring Report. https://documents.deq.utah.gov/water-quality/standards-technical-services/gsl-website-docs/uprr-causeway/DWQ-2021-002902.pdf

HDR, Annual Reports, 2017-2019, received directly from HDR, https://documents.deq.utah.gov/water-quality/standards-technical-services/gsl-website-docs/uprr-causeway/

HDR Inc., GSL breach and causeway bathymetry, 2017.

Hirt, C. W., & Nichols, B. D. (1981). Volume of fluid (VOF) method for the dynamics of free boundaries. *Journal of computational physics*, 39(1), 201-225.

Holley, E. R., and Waddell, K. M. (1976). Stratified Flow in Great Salt Lake Culvert. Journal of the Hydraulics Division, 102(7), 969-985.

http://alexlenail.me/NN-SVG/index.html

https://keras.io/

https://maps.waterdata.usgs.gov/mapper/index.html

https://waterdata.usgs.gov/nwis/uv?site_no=10010025 https://waterdata.usgs.gov/nwis/uv?site_no=10010026

https://waterdata.usgs.gov/nwis/uv?site_no=10010027

https://www.tensorflow.org/api_docs/python/tf/keras/optimizers/Adam

Jellison, R., Williams, W. D., Timms, B., Alocer, J. & Aladin, (2008). N. V. in Aquatic Ecosystems: Trends and Global Prospects (ed. Polunin, N. V. C.) *Cambridge Univ. Press* 94–112

Levesque, V.A. and Oberg, K.A. (2012). Computing discharge using the index velocity method. U.S. Geological Survey Techniques and Methods 3-A23. U.S. Department of the Interior, U.S. Geologic Survey. 148p. Reston, Virginia.

Loving, B.L., K.M. Waddell, C.W. Miller. (2000). Water and salt balance of Great Salt Lake, Utah, and simulation of water and salt movement through the causeway, 1987-98. U.S.G.S Water- Resources Investigations Report 00-4221. Salt Lake City, UT.

Messager, M. L., Lehner, B., Grill, G., Nedeva, I. and Schmitt, O. (2016). Estimating the volume and age of water stored in global lakes using a geo-statistical approach. *Nat. Commun*. 7, 13603..

Mischke, S., Liu, C., Zhang, J., Zhang, C., Zhang, H., Jiao, P., & Plessen, B. (2017). The world's earliest Aral-Sea type disaster: the decline of the Loulan Kingdom in the Tarim Basin. *Scientific reports*, 7(1), 1-8.

Mohammed, I. N. and D. G. Tarboton, (2012), "An examination of the sensitivity of the Great Salt Lake to changes in inputs," Water Resour. Res., 48(11): W11511, http://dx.doi.org/10.1029/2012WR011908.

Mohammed, I. N. and D. G. Tarboton, (2011), "On the Interaction between Bathymetry and Climate in the System Dynamics and Preferred Levels of the Great Salt Lake," Water Resour. Res., 47: W02525, http://dx.doi.org/10.1029/2010WR009561.

Naftz, D. L., Cederberg, J. R., Krabbenhoft, D. P., Beisner, K. R., Whitehead, J., and Gardberg, J. (2011). Diurnal trends in methylmercury concentration in a wetland adjacent to Great Salt Lake, Utah, USA. *Chemical Geology*, 283(1-2), 78-86.

Naftz, D. L., Millero, F. J., Jones, B. F., & Green, W. R. (2011). An equation of state for hypersaline water in Great Salt Lake, Utah, USA. *Aquatic Geochemistry*, 17(6), 809-820.

Null, S.E., W.A. Wurtsbaugh, and C Miller. (2013). Can the causeway in the Great Salt Lake be used to manage salinity? Friends of Great Salt Lake Newsletter 19 (1&2)

Pope, S. B. (2001). Turbulent flows, Cambridge

Roache, P. J. (1998). Verification and validation in computational science and engineering. p. 895. Albuquerque, NM: Hermosa.

Sahraei, A., Chamorro, A., Kraft, P., Breuer, L. Application of Machine learning Models to Predict Maximum Event Water Fractions in Streamflow, Frontiers in Water, June 2021

Sit, M., Demiary, B., Xiang, Z., Ewing, G., Sermei, Y., Demir, I. A comprehensive Review of Deep Learning Applications in Hydrology and Water Resources, Water Science & Technology, accessed July 2021

Smagorinsky, J. (1963). General circulation experiments with the primitive equations: I. The basic experiment. *Monthly weather review*, 91(3), 99-164.

Spall, R.E. (2009). A Hydrodynamic Model of the Circulation within the South Arm of the Great Salt Lake. International Journal of Modelling and Simulation, 29:2, 181-190.

Spall, R. E. (2011). Basin-Scale Internal Waves Within the South Arm of the Great Salt Lake. International Journal of Modelling and Simulation, 31(1), 25-31.

Stephens, D. W. (1990). Changes in lake levels, salinity and the biological community of Great Salt Lake (Utah, USA), 1847–1987. *Hydrobiologia*, 197(1), 139-146.

U.S. Geological Survey (USGS) (2020). National Water Information System Data for the Nation. https://waterdata.usgs.gov/nwis/

Waddell, K.M., E.L. Bolke. (1973). The effects of restricted circulation on the salt balance of Great Salt Lake, Utah. Utah Geological Survey Water Resources Bulletin 18.

White, J., S. E. Null and D. G. Tarboton, (2014), "More than meets the eye - managing salinity in Great Salt Lake, Utah," Lakeline Magazine, North American Lake Management Society, Fall 2014, 25.

White, J. S., Null, S. E., and Tarboton, D. G. (2015). How do changes to the railroad causeway in Utah's Great Salt Lake affect water and salt flow?. *PloS one*, 10(12), e0144111.

WHSRN (2016). Western Hemisphere Shorebird Reserve Network. www.whsrn.org

Wurtsbaugh, W. A., Miller, C., Null, S. E., DeRose, R. J., Wilcock, P., Hahnenberger, M., and Moore, J. (2017). Decline of the world's saline lakes. *Nature Geoscience*, 10(11), 816-821.

Wurtsbaugh, W., C. Miller, S. Null, P Wilcock, M. Hahnenberger, F Howe. (2016). Impacts of Water Development on Great Salt Lake and the Wasatch Front. White Paper to the Utah State Legislature. Prepared by Utah State University, Utah Division of Water Resources, Salt Lake Community College, and Utah Division of Wildlife Resources.

Yang, S., Johnson, W. P., Black, F. J., Rowland, R., Rumsey, C., and Piskadlo, A. (2020). Response of density stratification, aquatic chemistry, and methylmercury to engineered and hydrologic forcings in an endorheic lake (Great Salt Lake, USA). *Limnology and Oceanography*, 65(5), 915-926.

Ying, X., An Overview of Overfitting and its Solutions, Journal of Physics: Conference series, Volume 1168, Issue 2

10.0 Personnel

Som Dutta, PhD

Principal Investigator - Utah State University: Som is interested in studying complex multiphase flow and morphodynamics phenomena in the natural and the built environment, using high-fidelity computational fluid dynamics (CFD). The range of phenomena he is interested in varies from exploring the mechanism underlying drag reduction by shark denticles (skin), dispersal of oil and contaminant in oceans and rivers, to fundamental dynamics of moving bodies in stratified environments. Som's primary training has been modeling complex environmental fluid mechanics phenomena in various environments. In the past he has been involved in hydrodynamic modelling of unidirectional and buoyancy driven flows in the Chicago River system, sediment and sludge laden flows in water reclamation plants, and high-speed flows through the diversion channel of the world's fourth largest hydro-electric dam (Belo Monte Dam, Brazil).

Brian M. Crookston, Ph.D., PE

Co-Principal Investigator - Utah State University: Brian's research and consulting experience is focused on water sustainability and resiliency including hydraulic structures, fluvial hydraulics, flooding, risk analyses and potential failure modes. Brian has been involved in over 300 domestic and international water resource projects that have included physical and numerical modeling tools, field studies, and machine learning algorithms. Prior to joining USU in 2018, Brian was the water resources technical lead for Schnabel Engineering where Brian lead a multi-year study for Del-DOT and DNREC for state-owned dams including field inspections, hydrologic studies, embankment erosion and failure, monte-carlo analyses, flooding impacts, inundation limits, and hydraulic structure modeling and analyses using 2- and 3-dimensional hydrodynamic models with the results provided as an online interactive portfolio via GIS database.

Bethany Neilson, Ph.D.

Team Member – Senior Expert – Utah State University

Dr. Neilson's expertise is on heat and mass transport in natural systems. Her research is primarily focused on the collection of field data sets fundamental to numerical modeling and identification of dominant fate and transport mechanisms. Her career has focused on quantifying groundwater/surface water interactions and the associated influences on instream water quality and temperature regimes. These efforts have spanned desert rivers, arctic river systems, low gradient agricultural rivers, and high gradient mountain streams. More recently, her research efforts have focuses on understanding the role of groundwater/surface water exchanges on instream temperatures and carbon fluxes in areas of continuous permafrost; groundwater exchanges throughout continuous permafrost landscapes and their controls on carbon and nitrogen delivery to streams and rivers; groundwater exchanges and influences on longitudinal solute trends in karst mountainous watersheds; instream temperature, nutrient, and habitat responses to the development of beaver dam complexes; and groundwater/surface water exchange influences on heat and nutrient transport in highly regulated river reaches.

David Tarboton, Ph.D.

Team Member – Senior Expert – Utah State University

Dr. Tarboton's expertise is in surface water hydrology and hydrologic modeling. He and his students have extensively studied and modeled the hydrology of Great Salt Lake and the watersheds that drain to it (Mohammed and Tarboton 2011, 2012). He was part of the CH2M team developing the Integrated Water Resources Management (IWRM) model for Great Salt Lake Basin. He also worked with Biowest on evaluating the environmental impact of Compass Minerals proposed evaporation pond expansion and on a previous Utah Forest, Fire and State Lands Project (White et al., 2014, 2015) examining the impacts of alternative UPRR causeway bridge opening scenarios on water and salt flow through the causeway. He has also worked on the sensitivity of lake levels to changes in inputs, and on the interaction between bathymetry and climate in lake dynamics.

Michael Rasmussen

Team Member – Graduate Student / Research Assistant

Michael is a graduate student in the Civil and Environmental Engineering Department at Utah State University and a Research Assistant at the Utah Water Research Laboratory. Michael was part of the field campaign and performed the CFD modeling of the West Crack Breach at the Great Salt Lake Causeway.

Eric Larsen

Team Member –Undergraduate Student / Research Assistant

Eric is an undergraduate student in the Mechanical and Aerospace Engineering Department at Utah State University and a Research Assistant at SPECTR lab at USU. Eric was part of the field campaign and performed the ANN modeling of the West Crack Breach at the Great Salt Lake Causeway.

Appendix A

Specific Conductance Data

INSTRUMENT MODEL NO. AQUATROLL 600

Specific Conductance and Temperature Profiles (October 2020)

DATA COLLECTED BY UWRL

Site Name	Latitude	Longitude	Depth (ft)	Depth (m)	Sample elev. (ft)	Temp (℃)	Sp. Cond. (µS/cm)
A	41.2206	-112.7661	1	0.319	-1	19.97	165700
			2	0.866	-2	19.75	165810
			4	1.158	-4	19.66	165730
			5.5	1.89	-5.5	19.28	>200000
			6	1.982	-6	19.4	>200000
			7	2.16	-7	18.9	
			8.00		-8	18.84	
B	41.2204	-112.766	2	0.85	-2	19.54	165800
			6	1.96	-6	19.3	195000 +- 1000
			13	4.1	-13	18.9	>200000
C	41.2205	-112.7661	1	0.3	-1	20	165760
			2	0.68	-2	19.95	165800
			4	1.16	-4	19.73	165720
			5.7	1.96	-5.7	19.7	180000
D1	41.2204	-112.7661	1	0.31	-1	20.05	165770
			2	0.86	-2	19.8	165739
			4	1.33	-4	19.7	165740
			5.6	1.9	-5.6	19.67	170100
			5.75	1.97	-5.75	19.57	180000
			6	2	-6	19.5	>200000
D2	41.2201	-112.766	1	0.29	-1	20.2	165800
			2	0.69	-2	20	165900
			4	1.503	-4	19.85	165800
			6	1.82	-6	19.8	165790
			8	2.75	-8	19.8	165805

			9.2	3.1	-9.2	19.6	180700
			10	3.2	-10	19.6	190000
			10.1	3.27	-10.1	19.6	193000
			10.2	3.3	-10.2	19.6	>200000
			12			19.4	>200000
E	41.22	-112.77	2	0.856	-2	19.75	164830
			3	1.31	-3	19.77	165450
F	41.22	-112.76	2	0.877	-2	19.26	165750
			6	2	-6	19.11	>200000
			5.5	1.8	-5.5	19.6	165900
H	41.2203	-112.7658	2	0.79	-2	20.25	165800
			4	1.23	-4	20.17	165780
			6	2.1	-6	20.1	165836
			7	2.16	-7	19.6	165950
I	41.22014	-112.7657	2	0.89	-2	20.23	165785
			4	1.3	-4	20.22	165805
			6	2.03	-6	20.18	165800
			7	2.35	-7	19.8	166000
			8	2.7	-8	19.45	166000
			9	3.05	-9	19.4	175000
			9.5	3.15	-9.5	19.5	190000
			10	3.19	-10	19.5	196000
			10.1	3.2	-10.1	19.5	>200000
			11	3.35	-11	19.5	>200000
J	41.22049	-112.76545	1	0.49	-1	19.5	165730
			3	1.18	-3	19.51	165795

Specific Conductance and Temperature Profiles (North Arm, November 2020)

DATA COLLECTED BY UWRL

Point	Latitude	Longitude	Depth (ft)	Sample Elev. (ft)	Temp (℃)	Sp. Cond. (µS/cm)	Note
A	41.22238	-112.76897	2	4190	17.08	223900	Bottom to top varied from 219-223000
B	41.22603	-112.76859	2	4190		220000	
C	41.22649	-112.76633	2	4190	11.8	223500	
			14	4178	11.06	223500	bottom
			0.21	4191.8	12.3	190000	top 2-3 inches
D	41.22424	-112.76337	2	4190	12.29	223400	
			13	4179	11.2	218000	bottom

Specific Conductance and Temperature Profiles (South Arm, November 2020)

DATA COLLECTED BY UWRL

Point	Latitude	Longitude	Depth (ft)	Sample Elev. (ft)	Temp (℃)	Sp. Cond. (µS/cm)
A	41.22029	-112.76608	2	4190.45	11.57	168660
			10	4182.45	11.12	205500
B	41.21999	-112.76604	2	4190.45	11.46	175553
			12	4180.45	11.07	197000
			13	4179.45	11.25	216600
			14	4178.45	11.4	223800
			15	4177.45	11.46	225500
			16	4176.45	11.48	225300
			12	4180.45	11.13	179000

			13	4179.45	11.26	201500
			14	4178.45	11.29	216000
			15	4177.45	11.5	225200
			0.5	4191.95	12.6	174500
C	41.22038	-112.76604	2	4190.45	11.85	172100
			6.5	4185.95	11.51	178200
			7	4185.45	11.52	222000
			8	4184.45	11.51	223079
			10	4182.45	11.48	223000
D	41.21976	-112.7661	2	4190.45	11.85	174800
			12	4180.45	11.08	192300
			11.5	4180.95	10.96	178000
			13	4179.45	11.24	212900
			14	4178.45	11.38	224100
			15	4177.45	11.47	224400
E	41.21929	-112.76527	2	4190.45	11.66	173500
			12	4180.45	10.97	182000
			12.5	4179.95	11.29	215500
			13	4179.45	11.39	219800
			14	4178.45	11.93	221500
			15	4177.45	11.44	221500
F	41.2194	-112.76542	10	4182.45		176500
			12	4180.45	10.96	177900
			12.5	4179.95	11.19	205000
			13	4179.45	11.38	218100
			14	4178.45	11.46	222700
			15	4177.45	11.5	225000
G	41.21999	-112.76506	2	4190.45	12.04	175800
			10	4182.45	11.22	176500

			11	4181.45	11.03	177000
			12.5	4179.95	11	177400
H	41.22012	-112.76645	2	4190.45	11.89	175800
			7	4185.45	11.36	176600
			12.5	4179.95	11.14	193700
			13	4179.45	11.25	205500
			13.5	4178.95	11.33	213300
			14	4178.45	11.43	218200
			14.5	4177.95	11.46	218700
I	41.21924	-112.76606	2	4190.45	11.86	165800
			8	4184.45	11.29	169100
			10	4182.45	11.13	170300
			11.5	4180.95	11	170900
			12	4180.45	10.96	171200

Appendix B

Total Dissolved Solids Data

ANALYSIS AT UTAH WATER RESEARCH LABORATORY

Date	Sample ID	Depth (ft)	Temp (℃)	σ (μS/cm)	TDS (g/L)
11/5/2020	1	12	11.13	186250	189
	2	13	11.26	202983	236
	3	14	11.29	211667	250
	4	15	11.5	216067	293
	5	0.5	12.6	168300	160
	South Shore	0	-	170583	160
	North Shore	0	-	215983	265
5/13/2021	North Shore	0	-		294
	South Shore	0	-		151
7/20/2021	North Shore	0	-		313
	South Shore	0	-		169

Appendix C

Select Field Campaign Photos

October 1, 2020

November 5, 2020

January 6, 2021

February 2, 2021

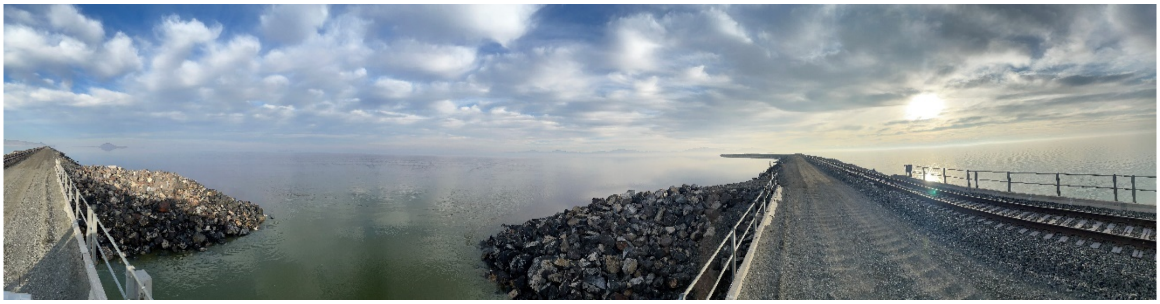

March 2, 2021

April 29, 2021

May 20, 2021


ASCE

Appendix D

Great Salt Lake Bathymetry (Baskin and Turner, 2006)

AUGMENTED HDR BATHYMETRY PROVIDED TO USU/UWRL

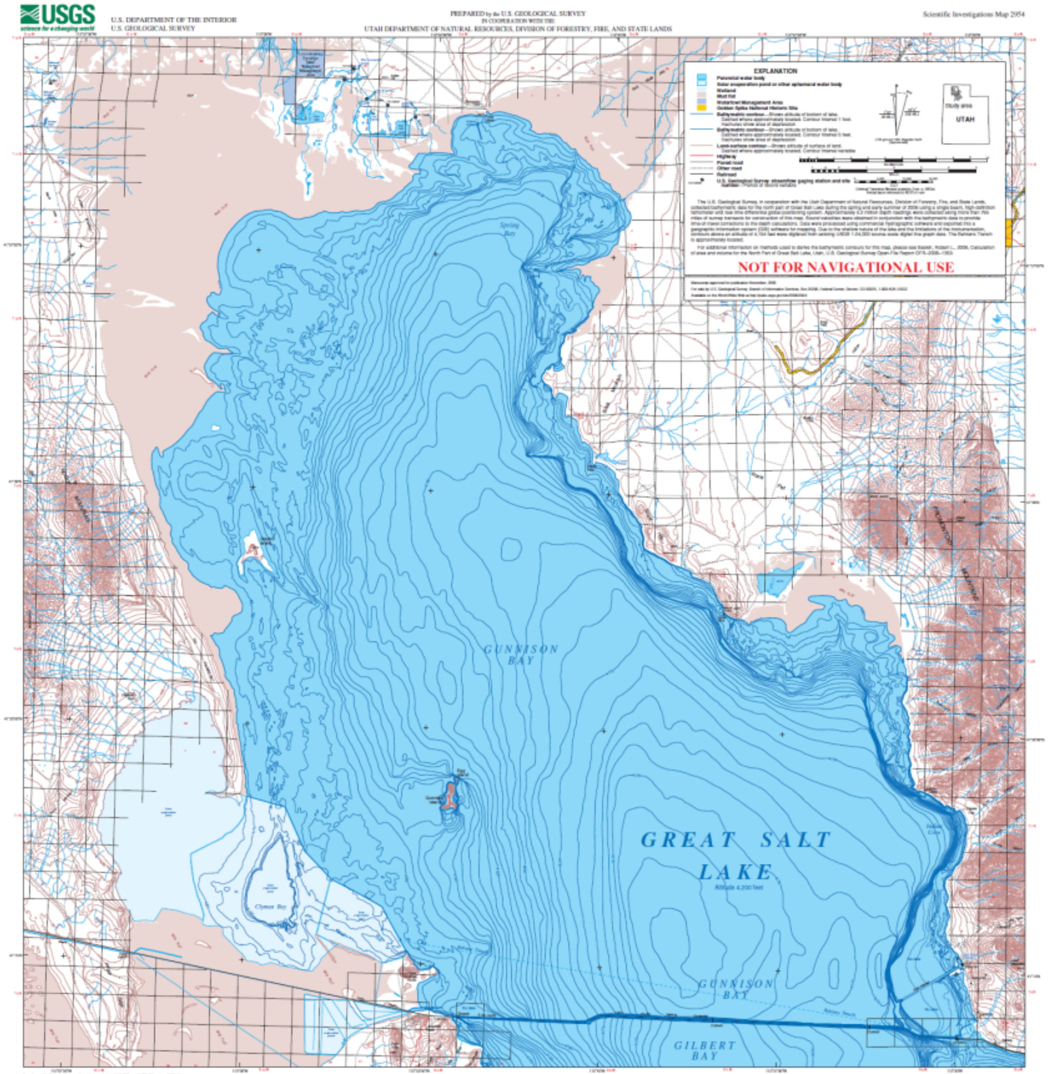

Bathymetric Map of the North Part of Great Salt Lake, Utah, 2006
By
Robert L. Baskin and Jane Turner
2006

Appendix E

Table of CFD Simulations Conducted

Sim #	Sim time interval (s)	ρ_S (slug/ft3)	ρ_N (slug/ft3)	$\Delta\rho$ (slug/ft3)	EL_S (ft)	EL_N (ft)	ΔEL (ft)	Cell size (ft)	Cell count
1	0-3500	2.05	2.25	0.200	4192.5	4192.3	0.2	1	49,400
2	0-3500	2.05	2.25	0.200	4192.5	4192.3	0.2	0.75	83,208
3	0-3500	2.05	2.25	0.200	4192.5	4192.3	0.2	0.6	134,323
4	0-3500	2.05	2.25	0.200	4192.5	4192.3	0.2	0.5	192,400
5	0-3500	2.05	2.25	0.200	4192.5	4192.3	0.2	0.4	286,000
6	2000-3500	2.05	2.25	0.200	4192.5	4192.3	0.2	0.3	528,687
7	2000-3500	2.05	2.25	0.200	4192.5	4192.3	0.2	0.25	696,800
8	3000-3500	2.05	2.25	0.200	4192.5	4192.3	0.2	0.1	4,368,000
9	0-3500	2.05	2.25	0.200	4192.6	4192.1	0.5	0.5	192,400
10	0-3500	2.05	2.25	0.200	4192.6	4192.1	0.5	0.5	192,400
11	0-3500	2.05	2.25	0.200	4192.6	4192.1	0.5	0.5	192,400
12	0-3000	2.05	2.25	0.200	4192.6	4192.1	0.5	0.5	192,400
13	0-3500	2.05	2.25	0.200	4192.5	4192.3	0.2	0.5	192,400
14	0-475	2.05	2.25	0.200	4192.5	4192.3	0.2	0.5	192,400
15	0-2500	2.129	2.353	0.224	4192.4	4191.9	0.5	1	13,185,000
16	0-2500	2.129	2.353	0.224	4192.4	4191.9	0.5	1	13,518,396
17	500-2500	2.129	2.353	0.224	4192.4	4191.9	0.5	0.5	15,852,168
18	0-1400	2.129	2.353	0.224	4192.4	4191.9	0.5	0.25	34,522,344
19	500-2500	2.129	2.353	0.224	4192.4	4191.9	0.5	0.5	15,852,168
20	0-1100	2.129	2.353	0.224	4192.12	4191.98	0.14	1	16,200,000
21	0-1000	2.134	2.32	0.186	4192.12	4191.98	0.14	1	16,200,000
22	0-2000	2.13	2.27	0.140	4192.12	4191.98	0.14	1	16,200,000
23	0-1500	2.13	2.27	0.140	4192.12	4191.98	0.14	1	16,200,000
24	0-1500	2.13	2.27	0.140	4192.32	4192.12	0.2	0.5	18,867,168
25	0-1300	2.13	2.27	0.140	4192.32	4192.12	0.2	0.5	18,867,168
26	0-1100	2.13	2.27	0.140	4192.32	4192.12	0.2	0.25	23,359,968
27	0-160	2.13	2.27	0.140	4192.32	4192.12	0.2	0.25	23,359,968
28	0-2000	2.13	2.27	0.140	4192.32	4192.12	0.2	1	16,200,000
29	0-2000	2.13	2.27	0.140	4192.32	4192.12	0.2	1	16,200,000
30	0-751	2.13	2.27	0.140	4192.32	4192.12	0.2	0.25	25,108,704
31	0-944	2.13	2.27	0.140	4192.32	4192.12	0.2	0.25	25,108,704
32	0-1300	2.147	2.27	0.123	4191.94	4192.08	-0.14	0.25	25,108,704
33	0-1700	2.14	2.27	0.130	4192.86	4192.35	0.51	0.25	25,108,704
34	0-1100	2.119	2.27	0.151	4192.32	4192.12	0.2	0.25	23,359,968
35	0-1000	2.104	2.27	0.166	4192.32	4192.12	0.2	0.25	23,359,968
36	0-1500	2.13	2.27	0.140	4192.32	4192.12	0.2	0.5	18,219,168
37	0-1500	2.13	2.29	0.160	4192.32	4192.12	0.2	0.5	18,219,168
38	0-1500	2.134	2.32	0.186	4192.32	4192.12	0.2	0.5	18,219,168
39	0-1500	2.13	2.33	0.200	4192.32	4192.12	0.2	0.5	18,219,168

40	0-1500	2.129	2.353	0.224	4192.32	4192.12	0.2	0.5	18,219,168
41	0-1500	2.14	2.27	0.130	4193.18	4192.56	0.62	0.5	18,219,168
42	0-1300	2.15	2.25	0.100	4193.3	4192.56	0.74	0.5	18,219,168
43	0-1415	2.13	2.29	0.160	4192.35	4192.12	0.23	0.5	18,219,168
44	0-1208	2.13	2.29	0.160	4191.78	4191.99	-0.21	0.5	18,219,168
45	0-733	2.13	2.29	0.160	4193.2	4192.4	0.80	0.5	18,219,168
46	0-785	2.13	2.29	0.160	4193.35	4193.12	0.23	0.5	18,219,168
47	0-798	2.13	2.29	0.160	4191.35	4191.12	0.23	0.5	18,219,168
48	0-795	2.13	2.29	0.160	4195.35	4195.12	0.23	0.5	18,219,168
49	0-1406	2.13	2.29	0.160	4189.35	4189.12	0.23	0.5	18,219,168